POLYTECHNIQUE MONTRÉAL

affiliée à l'Université de Montréal

Multi-mode bandpass filters with controllability, tunability and scalability

WENTAO LIN

Département de génie électrique

Thèse présentée en vue de l'obtention du diplôme de *Philosophiæ Doctor*

Génie électrique

Octobre 2022

POLYTECHNIQUE MONTRÉAL

affiliée à l'Université de Montréal

Cette thèse intitulée :

Multi-mode bandpass filters with controllability, tunability and scalability

présentée par **Wentao LIN**

en vue de l'obtention du diplôme de *Philosophiæ Doctor*

a été dûment acceptée par le jury d'examen constitué de :

Gunes KARABULUT KURT, présidente
Ke WU, membre et directeur de recherche
Tarek DJERAFI, membre
Jens BORNEMANN, membre externe

DEDICATION

To my beloved wife and parents

ACKNOWLEDGEMENTS

I would like to express my sincere gratitude to my supervisor Prof. Ke Wu for providing the opportunity to pursue my PhD degree at Poly-Grames Research Center, for giving his guidance, patience, encouragement, and confidence in my PhD study, and for supporting worldwide top-level research. Prof. Wu opens a new window to my life and leads me into a whole new world, thus changing my worldview. The study and research experience during my PhD will benefit me for a lifetime.

I would like to acknowledge the technical and administrative team at Poly-Grames Research Center. Especially, Traian Antonescu and Steve Dube for their circuit fabrication, Jules Gauthier, Louis-Philippe Carignan, Maxime Thibault and David Dousset for their support of the measurement, Rachel Lortie and Jean-Sebastien Decarie for their financial and IT help.

I would like to take this opportunity to thank all my colleagues for their valuable academic discussions and suggestions. Especially, Tae-Hak Lee, Kang Zhou, Ping Zhao and Kai Wang for professional suggestions, discussion and help in the field of filter design, Desong Wang, Xiaoqiang Gu, Yifan Yin, Lvzhou Chen and Yangping Zhao for adapting to life abroad, Jiapin Guo, Kuangda Wang, Ben You, Tongfeng Guo, Dongze Zheng, Yue-Long Lye, Amirhossein Askarian, Mohammad Reza Rahimi, Pascal Burasa, Chunmei Liu, Chao Li, Muhib Ur Tahma, Srinaga Nikhil Nallandhigal, Fang Zhu, Long Zhang, Gaoming Xu, Yunlong Lu, Lei Guo, Wenwen Yang, Peng Chu, Jun Xu, Yihong Su, Yunjie Geng, Bengeng Cai, Amir Afshani, Qingtao Chen, Xiaoyi Wang, Lianfeng Zou, Hao Chen, Xiaoxiong Song, Yuanwei Tong, Jiming, Li, Wencui Zhu, Omar Masood Kham, Nhu Huan Nguyen, Qingtao Chen, Guillaume Ndjamba, Lamine Asmarane Bamogho and Marko Zivanovic for building precious memories of life together.

I am extremely grateful to my parents, my wife and my parents-in-law for their continuously supporting, understanding and endless love. It is worth mentioning that I met my wife during my PhD. Thanks for her companionship, encouragement, and support all the time.

RÉSUMÉ

Avec le développement des systèmes de communication RF et sans fil, les ressources du spectre électromagnétique sont occupées par de nombreuses applications, telles que la diffusion, le Wi-Fi, la communication sans fil, la détection radar et l'imagerie, etc. Il n'y a pas assez de spectre non attribué pour prendre en charge plus de nouvelles applications émergentes. D'autre part, pour répondre à des besoins multistandards et multifonctions, la conception de dispositifs et de systèmes accordables et reconfigurables est une tendance dans le développement des technologies de communications modernes, ce qui représente un moyen efficace d'améliorer l'efficacité des ressources en bande passante, d'utiliser des porteuses distinctes et de s'adapter à une mise à niveau du système, parmi de nombreux autres scénarios. Dans les systèmes micro-ondes, les filtres jouent un rôle important dans de nombreuses applications RF et micro-ondes. De plus, la conception de filtres accordables et reconfigurables constitue un nouveau défi pour s'adapter aux systèmes sans fil modernes plus complexes tels que les applications de communication.

Le réglage seul des fréquences centrales des filtres ne permet pas de répondre aux différents scénarios d'application. Pour répondre à des objectifs multistandards et multifonctions, les filtres accordables et reconfigurables doivent présenter une variété de caractéristiques. Par exemple, le filtre présente ses propres caractéristiques de filtrage pendant le réglage de la fréquence centrale, couvre une plus large plage de réglage dynamique avec une largeur de bande constante et passe même d'une bande unique à une double ou multi-bandes.

Cette recherche doctorale porte sur un filtre passe-bande accordable avec des zéros de transmission (TZ) symétriques reconfigurables. Une méthode de synthèse de matrice de couplage adaptée à une classe de filtres passe-bande accordables (BPF) avec des caractéristiques de filtrage reconfigurables est présentée. Le filtre possède des zéros de transmission symétriques (TZs) qui peuvent être reconfigurés sur l'axe réel ou imaginaire du plan complexe. Différentes caractéristiques de filtrage peuvent être obtenues en accordant simplement les fréquences de résonance de certains résonateurs. L'accord de fréquence et les états reconfigurables du filtre peuvent être réalisés simultanément.

À l'exception des TZ symétriques, des filtres passe-bande accordables avec des zéros de transmission asymétriques commutables sont présentés dans cette recherche. Les filtres ont des zéros de transmission asymétriques qui peuvent être reconfigurés sur l'axe imaginaire du plan

complexe entre positif et négatif. Deux approches différentes, nommées la technique de couplage en fonction de la fréquence (FDC *: frequency-dependent coupling*) et la topologie en forme de boîte, sont implémentées pour la réalisation physique. La topologie avec FDC simplifie le chemin de circulation du signal, montrant une faible influence sur les autres coefficients de couplage lors de la reconfiguration des positions des TZ, ce qui est également plus facile pour la réalisation physique. Par ailleurs, dans la topologie en forme de boîte, le réglage de la fréquence et la commutation des TZ peuvent être réalisés simultanément en accordant simplement les fréquences de résonance des résonateurs.

De plus, une approche du développement des filtres passe-bande (*BPFs : bandpass filters*) accordables à guide d'ondes avec une large plage de réglage de fréquence (*FTR* : *frequency-tuning range*) tout en préservant une largeur de bande absolue (ABW *: absolute bandwidth*) constante est présentée. La clé pour réaliser ce type de BPF est que le mode fondamental et le mode commun dans une cavité rectangulaire peuvent être commutés en contrôlant les éléments de réglage. Les bandes de fréquences inférieures et supérieures peuvent être combinées par un rapport longueur/largeur approprié de la cavité rectangulaire pour réaliser une large FTR.

En outre, une approche du développement de filtres *BPFs* accordables à passe-bande reconfigurables en bande utilisant un concept de commutation de mode est étudiée et développée. La clé pour réaliser ce type de BPF est que le premier mode d'ordre supérieur de TE_{210} peut être commuté sur les modes diagonaux en utilisant des éléments d'accord dans une cavité de guide d'ondes carrée. Par conséquent, le BPF accordable correspondant peut être reconfiguré entre les états à bande unique et à double bande. En plus, un nombre flexible de pôles de transmission peut être également implémenté dans un état à double bande.

Enfin, un intérêt particulier pour le développement des techniques de filtrage de la bande THz est présenté à travers l'étude d'un nouveau mode résonnant. Ce mode peut rendre le volume de la cavité résonante plus grand que celui du mode fondamental tout en maintenant une valeur de qualité non chargée similaire à celle du mode fondamental. Cette nouvelle idée offre non seulement plus de possibilités pour la conception de filtres mais aussi des options techniques pour le développement technologique THz.

ABSTRACT

With the development of RF/wireless communication systems, the electromagnetic spectrum resource is occupied by extensive applications, such as broadcast, Wi-Fi, wireless communication, radar sensing, and imaging *etc*. There is not enough unallocated spectrum to support more novel and emerging applications. On the other hand, to satisfy the multi-standard and multi-function purposes, tunable and reconfigurable devices and systems design is a tendency in the development of modern communication technologies, which presents an efficient way to improve the efficiency of bandwidth resources, to utilize separate carriers, and to adapt to a system upgrade among many other scenarios. In microwave systems, filters play an important role in many RF/microwave applications. Moreover, tunable and reconfigurable filters design are new challenges to adapt to more complicated modern wireless systems such as communication applications.

Only tuning the center frequencies of filters cannot satisfy different application scenarios. To meet multi-standard and multi-function purposes, tunable and reconfigurable filters should exhibit a variety of features. For example, the filter manifests its own different filtering characteristics when tuning the center frequency, covers a much wider dynamic tuning range with constant bandwidth, and even switches between single band and dual-/multi-bands.

This doctoral research begins with a tunable bandpass filter with reconfigurable symmetric transmission zeros (TZs). A coupling matrix synthesis method tailored for a class of tunable bandpass filters (BPFs) with reconfigurable filtering characteristics is presented. The filter has symmetric transmission zeros (TZs) which can be reconfigured on the real or imaginary axis of the complex plane. Different filtering characteristics can be obtained by merely tuning resonant frequencies of certain resonators. The frequency tuning and reconfigurable states of the filter can be achieved simultaneously.

Except for symmetric TZs, tunable bandpass filters with switchable asymmetric transmission zeros are presented in this research. The filters have asymmetric transmission zeros that can be reconfigured on the imaginary axis of complex plane between positive and negative. Two different approaches, namely frequency-dependent coupling (FDC) technique and box-like topology, are implemented for physical realization. The topology with FDC simplifies the signal flow path, showing a little influence on the other coupling coefficients when reconfiguring the locations of

TZs, which is also easier for physical realization. Meanwhile, in the box-like topology, frequency tuning and TZ switching can be simultaneously achieved by merely tuning the resonant frequencies of resonators.

In addition, an approach to the development of tunable waveguide bandpass filters (BPFs) with a wide frequency-tuning range (FTR) while preserving a constant absolute bandwidth (ABW) is presented. The key to realize this type of BPF is that the fundamental mode and the common mode in a rectangular cavity can be switched by controlling tuning elements. The lower and higher bands can be combined by a suitable length-to-width ratio of the rectangular cavity to realize a wide FTR.

Furthermore, an approach to the development of band-reconfigurable tunable bandpass filters (BPFs) using a mode-switching concept is studied and developed. The key to realize this type of BPF is that the first higher-order mode of TE_{210} can be switched to the diagonal modes using tuning elements in a square waveguide cavity. Accordingly, the corresponding tunable BPF can be reconfigured between single- and dual-band states. Moreover, a flexible number of transmission poles can also be implemented in the dual-band state.

At last, a special interest in the development of THz band filtering techniques is presented through the investigation of a new resonant mode. This mode can make the volume of the resonant cavity larger than that of the fundamental mode while maintaining an unloaded quality value similar to that of the fundamental mode. This new idea provides not only more possibilities for designing filters but also technical options for THz technological development.

TABLE OF CONTENTS

LIST OF TABLES

LIST OF FIGURES

LIST OF SYMBOLS AND ABBREVIATIONS

ABW	Absolute bandwidth
AR	Augmented reality
BPFs	Bandpass filters
BRF	Band-reconfigurable filter
BST	Barium-strontium-titanate
CFs	Center frequencies
CQ	Cascaded quadruplet
DBC	Dual-band configuration
DR	Dielectric resonator
FBW	Fractional bandwidth
FDC	Frequency-dependent coupling
FTR	Frequency-tuning range
FPFA	Field-programmable filter array
FPMS	Field programmable microwave substrate
GSM	Global system for mobile communication
HBC	High band configuration
HFSS	High-frequency structure simulator
IL	Insertion loss
LBC	Low band configuration
LC	Liquid crystal
LTE	Long term evolution
LBC	Low band configuration

MEMS	Micro-electromechanical systems
ML	Microstrip line
NBC	No-band configuration
NRD	Non-radiative dielectric
PCB	Printed circuit board
RF	Radio frequency
RL	Return loss
SDR	Software define radio
SIW	Substrate integrated waveguide
TZs	Transmission zeros
UMTS	Universal mobile telecommunication system
VR	Virtual Reality
YIG	Yttrium iron garnet

LIST OF APPENDICES

CHAPTER 1 INTRODUCTION

1.1 Research background

The electromagnetic spectrum itself is a limited and scarce resource for RF and wireless applications. With the development of wireless communication systems, the spectrum resource is being exhausted by extensive wireless applications, such as broadcast, Wi-Fi, radar sensing, xG communication, *etc*. There is not enough unallocated spectrum to support more and more novel and emerging applications. Hence, how to improve the efficiency of spectrum allocations and how to accommodate more applications through the use of a limited spectrum resource are some of the key issues for current and future communication system design.

To improve signal and system capacity and efficiency in connection with bandwidth allocations, the modulation technique should become more elaborated in adapting to the development of emerging communication systems. With reference to the four-generation (4G), a technique to allocate bandwidth (channels) named carrier aggregation, allows combining several separate signal carriers to increase the efficiency of bandwidth allocations. However, these separate signal carriers require separate microwave components such as bandpass filters, which make the transceiver bulky and expensive.

On the other hand, with the increased demands of users in connection with signal transmissions from text and voice to video and Augmented reality/Virtual Reality (AR/VR), communication systems and standards are also evolving from Global System for Mobile Communication (GSM), Universal Mobile Telecommunication System (UMTS), Long Term Evolution (LTE), LTE-Advanced, to the five generation (5G). For communication operators, all different standards and systems mentioned above should be running simultaneously to sustain services. However, deploying individual base station for each generation communication is unpractical amid high operating costs. In other words, combining and sharing base stations is an economical way to go for current and future developments.

Based on the aforementioned spectrum issues, tunable and reconfigurable systems design is a tendency to develop communication technologies, which presents an efficient way to improve the efficiency of bandwidth allocations, to utilize separate carriers and to adapt to system upgrading. Frequency-agile RF and microwave devices have attracted much attention for growing demands in

dynamic spectrum management. For instance, Software Defined Radio (SDR), a communication system is a much-discussed platform to advance the efficiency of spectrum by employing tunable and reconfigurable components. In this case, RF/microwave components that are traditionally implemented in analog hardware are instead implemented by means of software on personal computers or embedded systems. Compared to separate or individual systems design, combining or joint operation development with tunable components allows systems to operate with multi-standard and multi-function. At the same time, the system real-estate is decreased with reduced weight and cost is reduced while the performance is improved.

As critical components, filters have been playing an important role in countless microwave applications. Depending on the requirements and specifications, they can be designed in the form of lumped elements or/and distributed elements and realized in various transmission line structures, such as rectangular waveguides [1-3], planar transmission lines [4-6], and substrate integrated waveguides (SIW) [7-9]. Based on the growing demands of frequency-agile RF/microwave devices and systems, tunable and reconfigurable filters are widely studied and used for that purpose. Essentially, those filters are set for tuning of either center frequency or bandwidth or both in response to specific application requirements.

1.2 Research objects

This thesis research is concerned with the theoretical foundation and experimental demonstration of various tunable and reconfigurable bandpass filters. The theoretical model will be investigated based on a coupling matrix platform, and an electromagnetic model will be developed using multiple modes, such as fundamental mode and higher-order modes. Specifically, this research work is focused on the following aspects:

1) To investigate a coupling matrix for tunable and reconfigurable bandpass filters. The existing coupling matrix theory is mainly implemented for fixed filters design. To theoretically guide how to design a tunable and reconfigurable bandpass filter, coupling coefficients in the coupling matrix should be tuned. Varying a few coupling coefficients would lead to reconfigurability of the filter but the performance should be considered for a possible physical realization.

2) To investigate the reconfigurable performance of a filter. This task is mainly focused on the locations of transmission zeros (TZs) and two points are highlighted in the work. First, a pair of symmetric TZs on the complex plane can be reconfigured between the real axis and the imaginary axis. Second, asymmetric TZs on the imaginary axis of the complex plane can be reconfigured between the positive imaginary axis and the negative imaginary axis of the complex plane.

3) To investigate the physical realization of a reconfigurable filter. The values of some internal coupling coefficients are needed to change from positive to negative in theoretically realizing the reconfigured performance of the filter. For physical realization, the coupling structure, the operating modes, and how to control/assign the tuning elements should be analyzed and decided.

4) To investigate the frequency-tuning performance of a filter with constant bandwidth, especially, at a higher operating frequency (>6 GHz). Regardless of physical internal or external coupling coefficients, each of coefficients has a limited dynamic range. Theoretical conditions are explored to keep a constant bandwidth and the possibility for a physical realization while maximizing the frequency-tuning range of the filter. Meanwhile, two or more operating modes are considered.

5) To investigate the band-reconfigurable performance of a filter. The mechanism on how to reconfigure the band will be examined and formulated. A possible number of poles in the passband in each band-reconfigurable state and frequency-tuning performance of the filter are discussed.

6) To investigate resonant modes for THz applications. This methodology should somehow make the resonant cavity larger compared to the initial resonant cavity (i.e., operating with the fundamental mode) at THz frequencies.

The tunable and reconfigurable bandpass filter design mainly contains two parts. First, searching for theoretical guidance based on the coupling matrix for a filter design will be described. Second, exploring for the physical realization of a reconfigurable filter will be conducted, especially, using higher-order modes.

1.3 Thesis outline

This Ph.D. thesis proposes and presents original research dedicated to the tunable and reconfigurable bandpass filter design and developments. The frequency-tuning and reconfigurable performances can be realized simultaneously using the same set of tuning elements. The reconfigurable performance of filter can be related to changing center frequency, location of transmission zeros on the complex plane, and number of passbands. In each design, experimental prototypes, theoretical foundation, and physical realization will be investigated and detailed. This thesis is organized as follows:

Chapter 1: The background and objectives of this research work on the tunable and reconfigurable bandpass filters are introduced.

Chapter 2: A review of reported research results on various tunable and reconfigurable bandpass filters is provided. The physical realization of operating modes and physical internal/external coupling coefficients will be emphasized.

Chapter 3: A coupling matrix synthesis method tailored for a class of tunable bandpass filters (BPFs) with reconfigurable filtering characteristics is presented. The filter has symmetric transmission zeros (TZs), which can be reconfigured on the real or imaginary axis of the complex plane. Different filtering characteristics can be obtained by merely tuning resonant frequencies of certain resonators. The frequency tuning and reconfigurable states of filter can be achieved simultaneously.

Chapter 4: Tunable bandpass filters with switchable asymmetric transmission zeros are presented. The filters have asymmetric transmission zeros that can be reconfigured on the imaginary axis of the complex plane between positive and negative. Two different ways, including frequency-dependent coupling (FDC) technique and box-like topology, are implemented for physical realization. The topology with FDC simplifies the signal flow path, showing a little influence on the other coupling coefficients when reconfiguring the locations of TZs, which is also easier for physical realization. Meanwhile, in the box-like topology, frequency tuning and TZ switching can be simultaneously achieved by merely tuning the resonant frequencies of resonators.

Chapter 5: An approach to the development of tunable waveguide bandpass filters (BPFs) with a wide frequency-tuning range (FTR) while preserving a constant absolute bandwidth (ABW) is presented. The key to realize this feature is that the fundamental mode and the common mode in a rectangular cavity can be switched by controlling tuning elements. The lower and higher bands can be combined by a suitable length-to-width ratio of the rectangular cavity to realize a wide FTR.

Chapter 6: An approach to the development of band-reconfigurable tunable bandpass filters (BPFs) using a mode-switching concept. The key to realize this type of bandpass filter is that the first higher-order mode of TE_{210} can be switched to the diagonal modes using tuning elements in a square waveguide cavity. Accordingly, the corresponding tunable BPF can be reconfigured between single- and dual-band states. Moreover, a flexible number of transmission poles can also be implemented in the dual-band state.

Chapter 7: A space controllable resonator for THz applications is presented. The resonator has a larger resonant cavity than that of the fundamental mode while it maintains an unloaded quality factor similar to that of the fundamental mode. The final volume of resonator is controllable at the same resonant frequency by changing the diameter of a metal post in the middle of the cavity.

Chapter 8: A comprehensive conclusion will be drawn first for the reported original research work and contributions we have made in this thesis to the tunable and reconfigurable bandpass filters. It is followed by an outlook into future works related to the research of this thesis, providing some interesting topics and directions on tunable and reconfigurable microwave components.

CHAPTER 2 LITERATURE REVIEW

2.1 Brief history of filter theory evolution

Methodologies and techniques of microwave filter design have undergone through a quite long evolution. Since 1922, numerous researchers have investigated and looked into filter design theory [10]. Around 1957, L. Weinberg presented explicit formulas for the modeling strategies of classical filter types for design considerations, named Tschebyscheff and Butterworth ladder networks [11], and later, R. Levy tabulated the element values for distributed low-pass prototype filters in 1965 [12]. This is a classic theory with low-pass topology for filter design.

In 1974, A. E. Atia and A. E. Williams, *etc*. presented for the first time a coupling matrix synthesis of filter networks [13]. R. J. Cameron presented the synthesis of a general class of the Chebyshev filter function in 1999 [14] and imported source and load coupling to advance coupling matrix synthesis techniques for microwave filters in 2003 [15]. All those mentioned above may epitomize a brief history of theoretical analysis of filter design based on major milestones. Nowadays, researchers and engineers are also interested in tunable filter design for more advanced circuits and systems.

2.2 Physical realization of tuning modes in the cavity-based structure

Since this thesis work is mainly focused on cavity-based structures, only waveguide and substrate integrated waveguide (SIW) structures will be considered and studied.

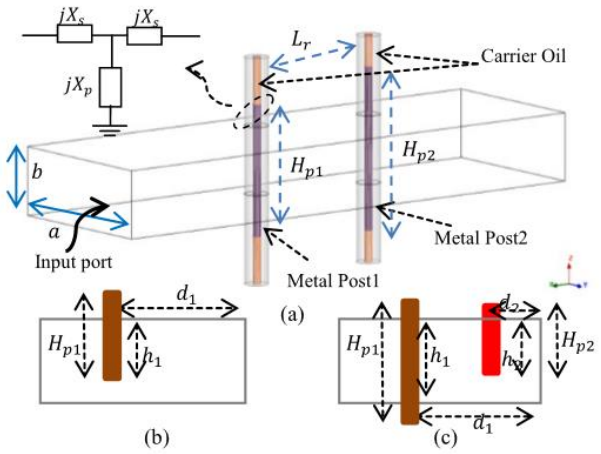

Figure 2.1 (a) The perspective view of a proposed structure. (b) The cross-section of a tunable band-reject element. (c) The cross-section of a reconfigurable waveguide filter [16]

2.2.1 Metal cavity-based tuning modes

The most commonly implemented operating mode is the fundamental mode which resonates in an empty cavity [17-20]. Deploying a tuning screw in the centre of the cavity, the mode is electrically perturbed. The deeper the height of the tuning screw goes, the lower the resonant frequency becomes [21, 22]. In [22], a tunable bandpass filter (tBPF) with one switchable transmission zero over X band was designed, fabricated, and measured. The measured frequency tuning range from 9.5 GHz to 10.8 GHz was achieved by tuning screws. Except for the tuning screws, liquid metal posts can tune resonant frequency. In [16], a WR42 reconfigurable band-reject/band-pass filter was realized by the integration of microfluidically controlled liquid metal posts. As shown in Fig. 2.1, a circular liquid metal post is partially inserted in the waveguide cavity for the dominant TE_{10} mode to achieve a tuning range from 18.20 GHz to 21.10 GHz. Also, a partial height post was used in conjunction with another microfluidic metal post to design a reconfigurable bandpass filter with one pole and one transmission zero. Moreover, dielectric perturbators are a good choice for waveguide structures [23, 24]. In [23], a tunable cavity resonator was composed of a resonating cavity and a dielectric perturbator. By varying the angle of rotation of the perturbator, a tuning range of 22.2% around 11.5 GHz while maintaining an unloaded Q factor between 1500 and 2300 was obtained.

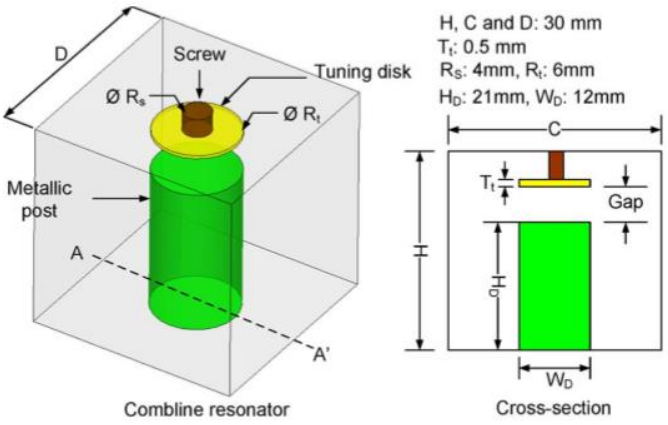

Figure 2.2 Combline tunable resonator with tuning disk [25]

The second type of structure is based on dielectric/ferrite-loaded resonators [25-28]. A new class of evanescent tunable combline bandpass filters based on one electronic tuning using RF micro-electromechanical systems (MEMS) or mechanical tuning using piezo motors was presented in [25]. The filter structure consists of combline resonators with tuning disks, as shown in Fig. 2.2. Also, it can be implemented using alternative technologies such as barium-strontium-titanate (BST) varactors to change the gap between the post and the tuning disk. In [29], the tuning disk technique is replaced by an angular tuning technique to maintain a constant Q value over a relatively wide tuning range. The physical filter structure was integrated with miniature piezoelectric motors and demonstrated a constant insertion loss over the tuning range centered at 3.6 GHz (11.9% tuning range). In [30], the post was replaced by a dielectric resonator in the cavity. The tunability was achieved by unique MEMS tuning elements to perturb magnetic and electrical fields surrounding the dielectric resonators and an approximately 400 MHz tuning range was obtained at Ku band. In [31], a high-Q tunable dielectric resonator (DR) filter consists of disk-shaped DRs with holes created in the center of each resonator and MEMS tuning circuits assembled inside the circular hole, as shown in Fig. 2.3. The physical structure can be extended to varactor-tuned structure by soldering GaAs varactor.

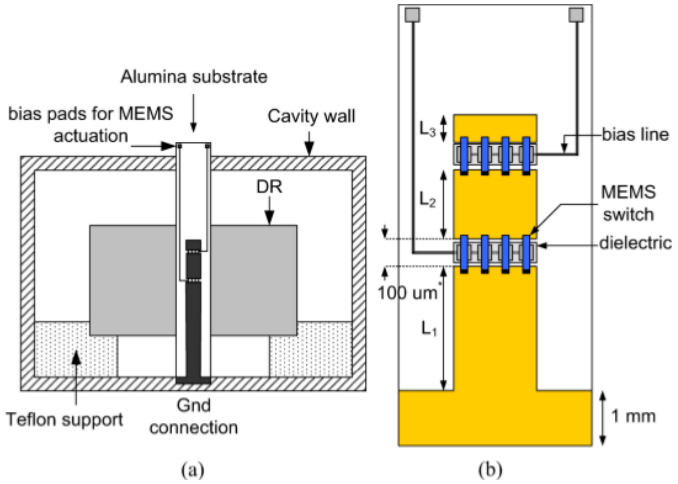

Figure 2.3 (a) Cross-sectional view of a dielectric resonator (DR) with tuning element inside. (b) Schematic view of an alumina substrate with tuning circuit (dimensions not to scale) [31]

Except for metal posts and dielectric materials loaded in the cavity, other materials are considered to make the tunable methodology more flexible [32-34]. For example, in [33], a high-power low-loss continuously tunable bandpass filter with transversely biased ferrite-loaded coaxial resonators was exhibiting a tuning span of 41%, where an externally applied transverse DC magnetic bias controls the center frequency between 740 MHz to 1040 MHz. Moreover, a continuously tunable non-radiative dielectric (NRD) waveguide bandpass filter based on liquid crystal (LC) technology at 60 GHz was presented. As shown in Fig. 2.4, LC is regarded as a tunable material to tune the center frequency and a tunability of 2.5% was measured with electrical biasing [34].

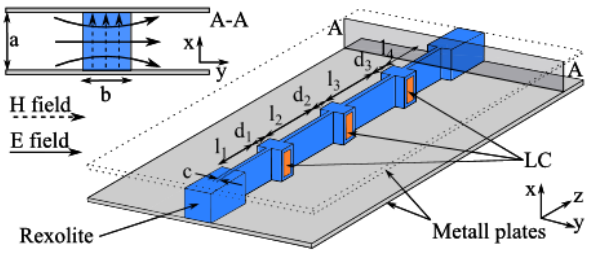

Figure 2.4 On the left-hand side, the field lines of operating LSM_{01} mode are shown in the *xy* plane. On the other side, a three-pole filter structure with stepped widths [34]

At last but not least, higher-order modes are chosen as the operating mode at high frequencies because a larger size of the cavity is easier to control resonant frequencies. In [35], only one tuning screw was deployed in the middle to tune the TE_{301} mode, as shown in Fig. 2.5. The advantage is that the tuning screw would not be that sensitive to tune the center frequency. However, how to suppress other higher-order modes must be figured out. The measured results exhibit a frequency tuning range from 17.0 GHz to 17.6 GHz with a bandwidth of 36 MHz.

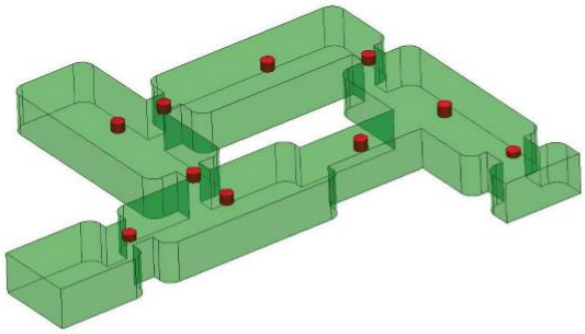

Figure 2.5 Folded tunable rectangular waveguide filter with rounded corners and real tuning screws [35]

2.2.2 SIW-based tuning modes

The physical realization for SIW-based tuning modes has more choices because circuits can be mounted on SIW surfaces. Therefore, switch, PIN diode [36], varactor diode [37], and MEMS [38-40] can be implemented for mode tuning. In [41], solid-state varactor diodes are surface-mounted to electrically perturb the resonator, as shown in Fig. 2.6. A center metallic via-hole shorts the top and bottom layer of the cavity, and two ring gaps are needed to create a bias point for varactors. The measured frequency tuning range is from 0.58 GHz to 1.22 GHz by controlling bias voltages. Replacing the varactor diodes, a mechanical tuning of SIW filters was presented in [42]. The via-hole is partially enclosed by a circular slot connected to the top layer, which is set to perturb the electromagnetic field distribution for the SIW resonator and change the resonant frequency. Also, a kind of mechanical tuning for a tunable circular resonator was realized by creating different distances between the moving copper column and the center of the circular cavity [43]. Finally, a tuning range of 12.6 GHz to 15.0 GHz was achieved by perturbing the dominant cavity resonance frequency.

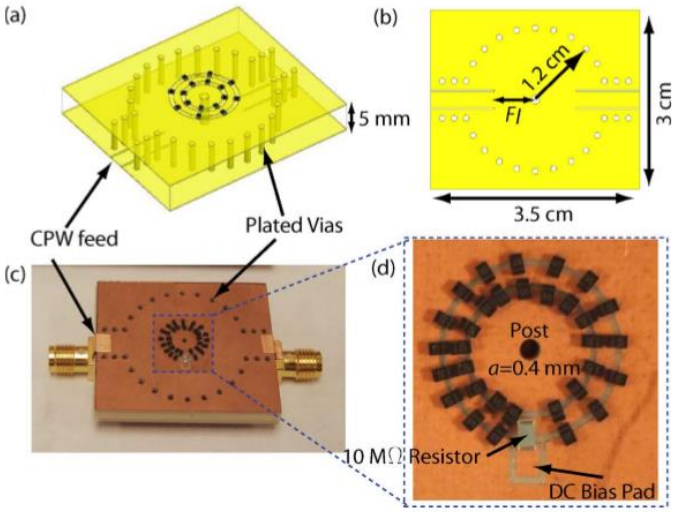

Figure 2.6 (a) Designed resonator's top view. (b) Bottom view showing CPW feedlines. (c) Rogers TMM3 substrate with vias and Skyworks SMV1405 varactors. (d) Close-up view of two surface ring gaps showing the varactors (not soldered on yet) and the dc bias point [41]

In addition, the surface-mounted varactor diodes can be replaced by contactless tuners [44, 45], especially operating at high frequency. A K-band tunable filter with contactless printed circuit board (PCB) tuners was presented, as shown in Fig. 2.7. There are two main advantages to make them attractive. First, they are based on low-cost PCB technology. Second, contactless tuners exhibit no hard contact with evanescent-mode cavities. The fabricated resonators can be tuned from 20 GHz to 26.5 GHz, which minimizes the insertion loss by utilizing extended cavity sidewalls.

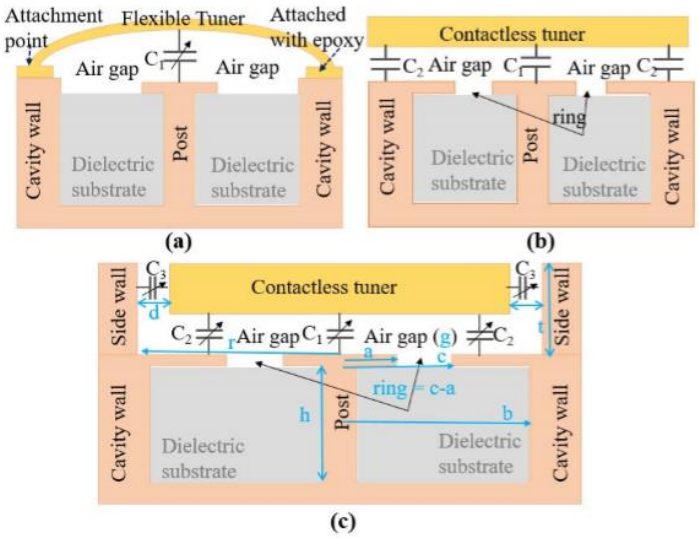

Figure 2.7 Tunable EVA-cavity resonator tuning concept. (a) Conventional. (b) Contactless. (c) Contactless with sidewall [44]

The second way is the use of material-loaded SIW cavity resonators, such as ferrite and liquid metal [46-50]. In [46], a magnetically tunable ferrite-loaded SIW cavity resonator is operated in the dominant mode and the ferrite slabs are loaded on both side walls of the cavity, where the value of magnetic field is the highest. Eventually, a frequency tuning range of more than 10% at X-band was obtained. Moreover, a concept of simultaneous electric and magnetic 2-D tuned SIW cavity was introduced as a building block in [50], as shown in Fig. 2.8. The significant interest is that the 2-D tuning not only allows changing resonant frequencies but also optimizes other key specifications, such as return loss and unloaded quality factor. A total tuning range of as much as 20% was experimentally achieved around 12 GHz using ferrite slabs and surface-mounted capacitors. In [48], a SIW band-reconfigurable filter was realized by liquid metal, which is chosen to enable switching between different configurations by filling or emptying certain via-holes and channels. Four different states are obtained, including dual-band, low band, high band and no-band, as shown in Fig. 2.9.

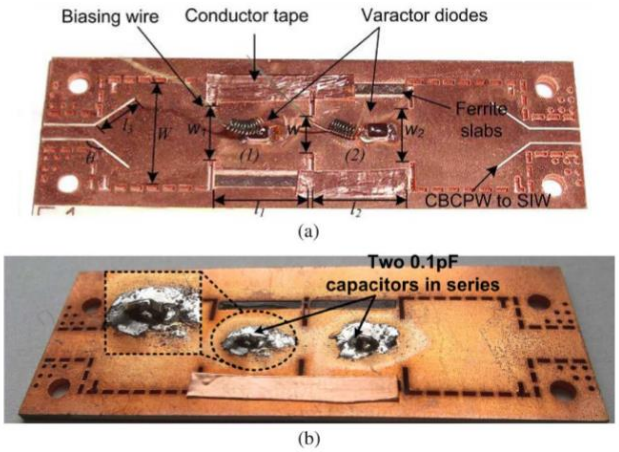

Figure 2.8 Fabricated SIW second-order Chebyshev bandpass filter. (a) Top view. (b) Bottom view[50]

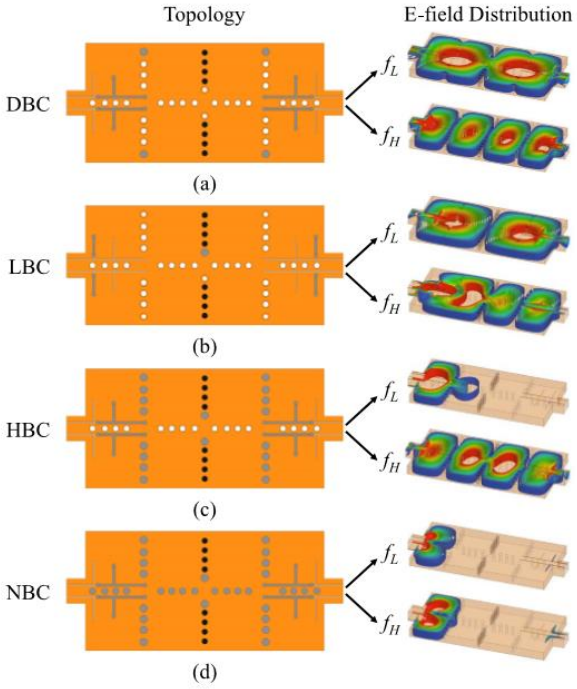

Figure 2.9 Band-reconfigurable filter (BRF) topologies and corresponding E-field distributions at the center frequency of each band. A liquid metal configuration in the channels and via holes are shown in gray, whereas white represents air and black represents copper. (a) Dual-band configuration (DBC). (b) Low band configuration (LBC). (c) High band configuration (HBC). (d) No-band configuration (NBC)[48]

The third approach is using piezo actuators, which are mainly deployed in the group of Prof. Juseop Lee [51-55]. The physical structures are shown in Fig. 2.10. In [51], a wide frequency tuning range from 0.98 GHz to 3.48 GHz was achieved and the physical structure is given in Fig.2.10(a). A capacitive post is embedded in the cavity and a piezo actuator is used to change the gap between the post and the copper foil so as to change the final resonant frequency. In [52], a tunable bandstop filter is physically designed by a conductive loading element deployed in the middle of the cavity, as shown in Fig. 2.10(b). A wide spurious-free upper passband covering 0.85 GHz to 6.6 GHz was obtained by changing the small air gap using piezoelectric actuators. Afterwards, multi-functional solutions and various designs have been proposed based on this type of resonator technique [53-58]. For example, in [53], a field-programmable filter array (FPFA) was presented by controlling the positive and negative inter-coupling. In [54], a frequency-tunable tri-function filter was presented by adding switches on a microstrip line. Three different states, including bandpass, all-pass and bandstop, can be switched.

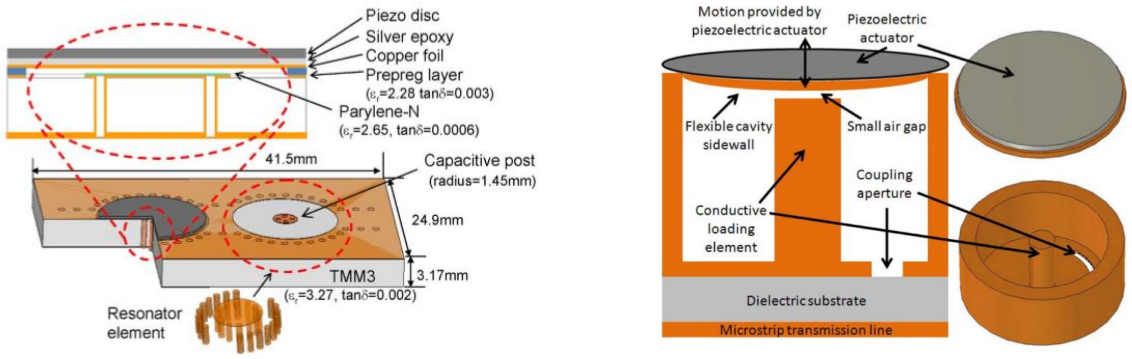

(a) (b)

Figure 2.10 (a) 3-D view of a tunable evanescent-cavity mode filter[51]. (b) Illustration of an evanescent-mode cavity resonator coupled to a microstrip line through an aperture in the microstrip line's ground plane and a 3-D model of the evanescent-mode cavity resonator[52]

The fourth method is based on higher-order mode, half-mode, or quarter mode, *etc*. Similar to metal cavity-based tuning modes, the use of SIW-based tuning modes is also possible based on dual modes [59-61]. In [59], a dual-mode SIW resonator can change frequencies of both even and odd

modes simultaneously through a contactless tuner and achieve a whole tuning range eventually. In addition, it also works for half-mode resonators [62-67]. In [62], a ferrite-loaded half-mode SIW bandpass filter was presented. A planar Yttrium Iron Garnet (YIG) slab is loaded along the metalized wall of the cavity to achieve magnetic tuning. By controlling the applied magnetic bias and the value of loaded lumped capacitors, the bandwidth tunable bandpass filter was demonstrated. Moreover, in [68], a miniaturized eighth-mode SIW filter was presented. The filter uses a stub-capacitor-loaded structure to achieve miniaturization and to tune the center frequency as well as variable bandwidth.

2.3 Physical coupling realization

Different physical coupling realization techniques for cavity-based structures will be introduced in this section. First, coupling structures for a fixed coupling value, regardless of positive or negative cases, will be discussed. Then, a revised structure for realizing flexible coupling values will be investigated.

2.3.1 Metal cavity-based coupling iris

2.3.1.1 Fixed coupling physical structure in the metal cavity

For metal cavity-based physical coupling, the most common structures are inductive coupling irises. According to the operating modes and the locations of coupling irises, they are possible to realize positive or negative couplings. In [69, 70], coupling irises are deployed in the middle of two fundamental modes. The positive coupling will be stronger with a larger width of the iris. In [71, 72], TE_{201} and TE_{10} modes are resonating in the same cavity. As shown in Fig. 2.11, positive or negative couplings can be selected based on different locations of irises. It will be in-phase if coupling irises are on the same side and it will be out-of-phase if coupling irises are on the opposite side. Moreover, multi-layer topology can flexibly adjust the positions of coupling irises to obtain positive or negative couplings. For example, in [73], the irises can be deployed in the middle of the cavity where the electric field is strongest or around the wall where the magnetic field is strongest, so positive or negative values of coupling are achieved. Even if two or more irises can be deployed to suppress higher-order modes, the performance of out-of-band rejection will be improved.

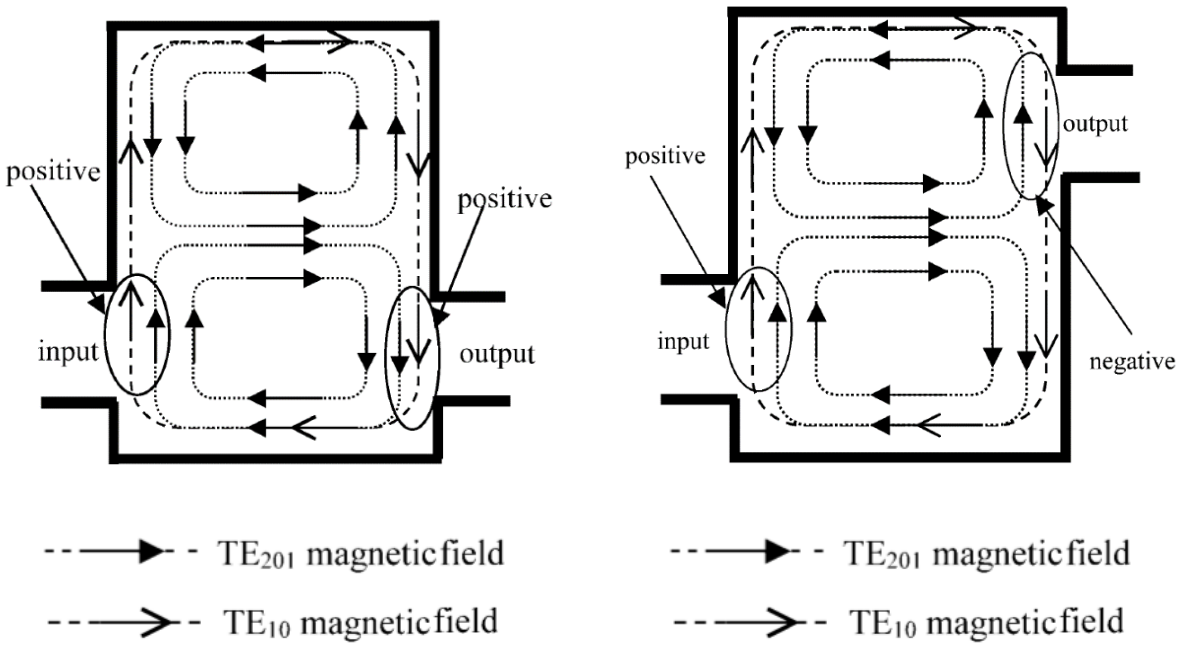

(a) (b)

Figure 2.11 Magnetic field of mode TE_{201} and TE_{10}. (a) Positive coupling. (b) Negative coupling

Except for the coupling irises, capacitive probe is usually coupled between two non-adjacent resonators to realize negative coupling. In [74], a capacitive probe was cascaded with a 180-degree transmission line. It can be regarded as a lumped inductor and generate a positive coupling.

Finally, some mixed-coupling structures are investigated. In [75], electric and magnetic coupling can be separately controlled in an inline coaxial filter. The coaxial coupling structure consists of two modified rods, a coupling strip, and a coupling pin, which results in a mixed-coupling. In [76], several fundamental building blocks with frequency-dependent couplings (FDCs) have been introduced. The FDC is usually realized as a partial height post, which controls the location of transmission zero.

2.3.1.2 Flexible coupling physical structure in the metal cavity

Flexible coupling physical structures are evolved and upgraded from the fixed physical structures. Deploying a tuning screw in the middle of a coupling iris can decrease electric coupling and hence increase total coupling. In [74], a decoupling wall on the bottom side is set in the middle of two adjacent resonators and a tuning screw is deployed on the top side. The final coupling strength is decided by the depth of the tuning screw.

The other approach is using a partial height of post between resonators. At the same time, one transmission zero will be generated. In [75], two resonators are frequency-dependent, coupled by a partial height post. Moving along the wall side direction and changing the depth of the post can alter the coupling.

2.3.2 SIW-based coupling iris

2.3.2.1 Fixed coupling physical structure in the SIW cavity

For SIW cavity-based physical coupling, the most common structures are inductive coupling irises [20, 77]. They are similar to the metal cavity-based physical coupling structures. To realize positive or negative coupling values, different resonating modes can be selected and locations of coupling irises can be deployed [78-80]. In [81], SIW resonators in multilayer substrates can be vertically coupled with both electric and magnetic couplings through an aperture over the middle metal layer. The advantage of this structure is that the first higher-order modes TE_{102} can be suppressed. In [9], a negative magnetic coupling structure was studied. A special planar negative coupling scheme, which involves a magnetic coupling post-wall iris and a balanced microstrip line with a pair of metallic via-holes, was investigated in detail. Two fourth-order cross-coupled bandpass filters were implemented on a single substrate. In [82], a mixed coupling which consists of two inter-resonator coupling structures with opposite coupling signs was studied and realized. The positive coupling by an inductive iris can be cancelled out by a continuously tunable microstrip line-based negative coupling structure. In other words, the signal route selectivity, no matter the positive or negative value, can be managed. Moreover, in [83], the coaxial-cavity resonators were mixed electric and magnetic inter-resonator coupling as shown in Fig. 2.12. Eventually, positive or negative coupled values can be obtained.

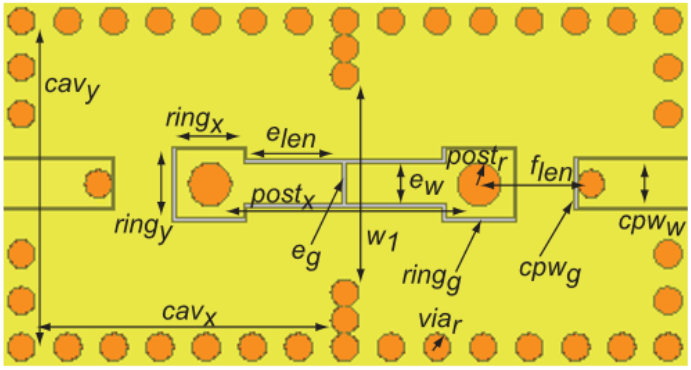

Figure 2.12 Two resonators with mixed electric and magnetic inter-resonator coupling[83]

2.3.2.2 Flexible coupling physical structure in the SIW cavity

By implementing tuning elements within fixed physical structures, flexible coupling physical structures can be realized. The tuning elements can be varactor diodes, PIN diodes, switches, MEMS, etc., which are the same as those designed for tuning resonators. Based on the coupling schemes, there are mainly two methods. The first is that the structure is set to only change the strength but does not alter the sign. For example, in [84], two resonators were electrically coupled by an etched microstrip line. Two varactor diodes mounted on the top layer can equivalently change the length of a coupled line so as to alter the coupling strength.

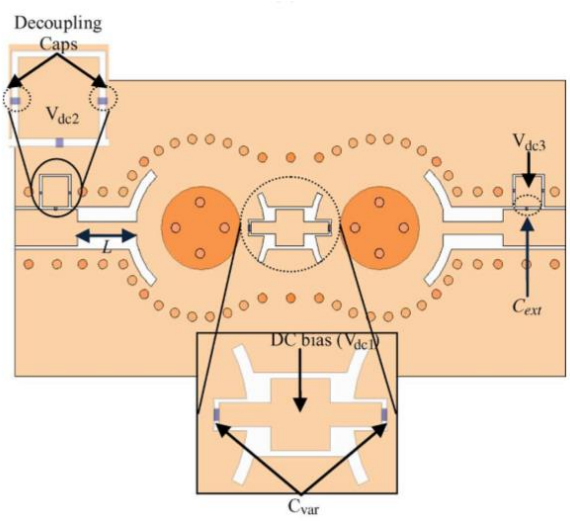

Figure 2.13 Varactor diodes mounted on top layer for varying internal coupling strength

The second is that structure can be designed to change the strength and sign together. Generally, it has two coupling paths and either one of the strengths associated with the paths can be changed so the total strength is varied. In [53], a tunable inter-resonator coupling structure capable of varying the coupling coefficient between resonators from positive to negative values was demonstrated and shown in Fig. 2.14. The resonators are coupled to each other through a varactor-loaded uniform transmission line and coupling slot. Controlling the bias voltages for varactor diodes, the total internal-coupling value becomes tunable.

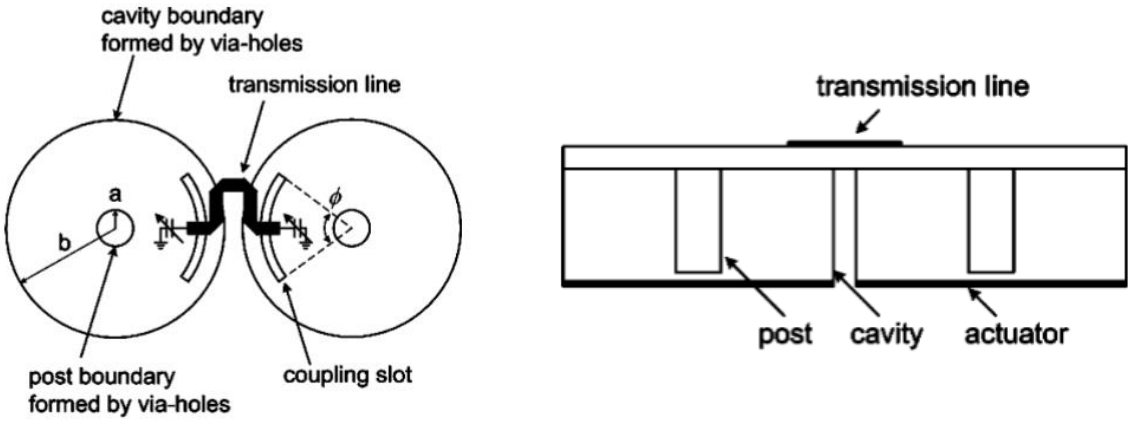

(a) (b)

Figure 2.14 Tunable cavity resonators and tunable inter-resonator coupling structure [53]

2.4 Other physical structures

Many novel physical configurations for tunable filters have been proposed so far. For example, the resonating modes and the internal/external couplings can be controlled together using fewer tuning elements [85-88]. In [85], the methodology of tunable filter design was developed to cover the inter-resonator coupling, input-output coupling, and tuning elements. The proposed tunable WG filter is shown in Fig. 2.15. The features of frequency tuning performance and constant absolute bandwidth were obtained by only one tuning element.

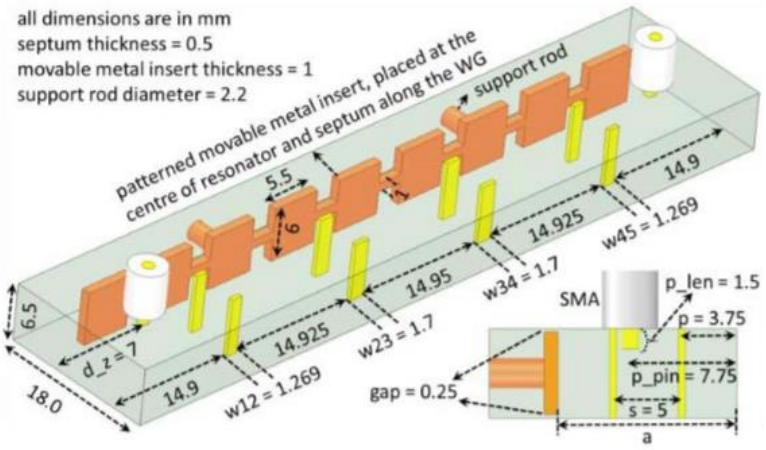

Figure 2.15 3-D schematic of a proposed tunable WG filter [85]

Moreover, in [89], the concept of field programmable microwave substrate (FPMS) was introduced for reconfigurable microwave filters. It allows the implementation of a filter with controllable filter order, operating bandwidth, and tunable center frequencies. The proposed filter is given in Fig. 2.16. The resonant frequency of the FPMS cavity is tuned by changing the bias voltage of the cavity unit cell lattice.

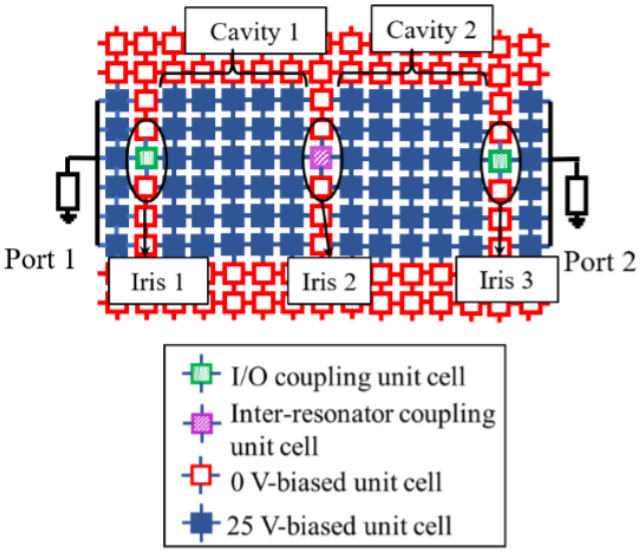

Figure 2.16 The proposed field programmable microwave waveguide filter [89]

CHAPTER 3 TUNABLE BANDPASS FILTER WITH RECONFIGURABLE SYMMETRIC TRANSMISSION ZEROS

This chapter is basically copied from one paper, *tunable bandpass filters with reconfigurable symmetric transmission zeros on real or imaginary axis*, and introduces a coupling matrix synthesis method tailored for a class of tunable bandpass filters (BPFs) with reconfigurable filtering characteristics. The type of filter has symmetric transmission zeros (TZs) which can be reconfigured on the real or imaginary axis of the complex plane. Different filtering characteristics can be obtained by merely tuning resonant frequencies of certain resonators. The frequency tuning and reconfigurable states of the filter can be achieved simultaneously.

The synthesis procedure mainly includes three steps. First, a transversal coupling matrix is synthesized according to the design specifications of one of the reconfigurable states. Second, the matrix is transformed to an intermediate configuration, in which some of the coupling coefficients on the mainline couplings are designated as key coefficients. Tuning these key coefficients alone can change the locations of TZs to realize reconfigurable filtering characteristics. In this intermediate configuration, the coupling matrix is optimized based on the values of synthesis to make all reconfigurable filter states meet their design requirements. Finally, the key coefficients are rotated to the diagonal entries of the coupling matrix so that reconfigurable TZs are realized by merely tuning the resonant frequencies of certain resonators.

The reconfigurable mechanism and the maximum number of TZs for different filter orders are investigated in detail for a variety of coupling diagrams. Two synthesis examples are presented to show the novel reconfigurable filter optimization procedure. For experimental verification, a fourth-order tunable BPF with a pair of reconfigurable symmetric TZs was fabricated and measured. The filter states with TZs on the real or imaginary axis of the complex plane can be switched solely by tuning resonant frequencies, which validates the proposed synthesis approach of tunable filters.

3.1 Introduction

Tunable filters are important alternatives to traditional filter banks thanks to their wide frequency coverage, flexible reconfigurable capability, and compact size. They play an ever-increasing critical role in emerging terrestrial and space wireless communication systems in response to the

trendy development of multi-network convergences and multi-function applications such as space-air-ground integrated network, cognitive radio, and software-defined radio (SDR). Different methods for designing tunable filters with transmission zeros (TZs) on the complex plane have been proposed in recent decades [41, 50, 53, 71, 74, 84, 85, 90-96]. Symmetric TZs on the appropriate positions of the real axis of the complex plane can improve the in-band group delay response, which are usually created by an in-phase cross-coupling in a cascaded quadruplet (CQ) topology [97-102]. On the other hand, symmetric TZs on the imaginary axis of the complex plane can improve near-skirt selectivity, which can also be generated by the CQ coupling diagram but with a negative cross-coupling [9]. For the physical realization of cross-coupled filters, positive couplings are usually realized as inductive coupling irises, whereas negative couplings are created through different realizations, which have been widely investigated [74], [9, 103-106]. For example, a capacitive coupling probe in waveguide structures [74] or balanced microstrip lines with a pair of metallic via-holes in a substrate integrated waveguide (SIW) structure [9] can introduce a negative coupling. Multilayered topologies [103] and [104], and higher-order modes with properly designed coupling irises [105] and [106] can also produce negative couplings.

It is well-known that the phases of different paths in cross-coupled topologies determine the type of TZs. Therefore, reconfigurable filtering characteristics can be realized by reversing the signs of cross-couplings. In this way, a versatile internal coupling circuit design that can tune coupling coefficients from positive to negative was presented [53, 82, 83, 107]. In [53] and [83], an appropriate combination of magnetic and electric couplings was realized by soldered varactor diodes. Two inter-resonator coupling structures, namely the negative microstrip line and the positive inductive iris, are integrated in [82]. Dual-mode resonators with perturbation technology were reported to introduce a coupling phase reversal equivalently [107]. However, there are three drawbacks to the previous designs of tunable bandpass filters. First, all these approaches require relatively complicated circuit structures, which demand time-consuming simulation and high-precision fabrication. Second, the tuning range of internal coupling coefficients is limited by the tuning elements designed to control the coupling strength. It may not be able to completely cover the required tuning range of the filter in question. Third, the internal coupling coefficients and the resonant frequencies are controlled independently, which would increase the number of tuning elements. Although numerous efforts and attempts related to tunable bandpass filters involving the

relocation of TZs have been presented, theoretical guidance on reconfiguring symmetric TZs on the complex plane has not been reported or discussed so far.

In this chapter, an approach to synthesis for tunable bandpass filters with reconfigurable symmetric TZs is proposed. The complex internal coupling structure design can be replaced by simple inductive coupling irises, which are theoretically interpreted through coupling matrix rotations. At the same time, the symmetric TZs reconfigurability on the real or imaginary axis of the complex plane can be managed together with a center frequency control by merely tuning the resonant frequencies to decrease the number of tuning elements. Besides, the reconfigurable mechanism and the maximum number of controllable TZs under various coupling diagrams are investigated in detail for different filter orders.

The subsequent sections are organized as follows. The proposed synthesis procedure of tunable bandpass filters is introduced and explained in Section 3.2. The optimization steps are provided in Section 3.3. Two synthesis examples are presented in Section 3.4 to show how to implement the optimization steps. In Section 3.5, a fourth-order tunable bandpass filter prototype is fabricated and measured to experimentally validate the proposed method. Finally, the conclusion is drawn in Section 3.6.

3.2 Synthesis procedure of tunable filters

In this section, the synthesis procedure of tunable filters is detailed and discussed. Realizing reconfigurable symmetric TZs on the complex plane is the primary concern in this work. The synthesis procedure can be divided into five steps:

(1) Synthesize a normalized coupling matrix. A transversal coupling matrix can be synthesized according to the design specifications for realizing the generalized Chebyshev filtering characteristics [14].

(2) Transform the coupling matrix. The transversal coupling matrix is first transformed to a folded canonical form. Then the folded coupling matrix is further rotated to an intermediate cascaded topology, where some mainline couplings are chosen as the key coefficients. Tuning these key coefficients alone can realize reconfigurable filtering characteristics. How to choose key

coefficients depends on the cascaded blocks in the intermediate topology, which will be explained in the following sections.

(3) Make the cross and mainline couplings positive. If a cross-coupling is negative, multiplying the whole row and column by -1 would reverse its sign. Subsequently, this process is repeated and applied to the mainline couplings except for those key coefficients.

(4) Optimize the coupling matrix. The initial coupling matrix is synthesized based on one possible set of TZs. It may not produce acceptable performances for other reconfigurable filter states, which are obtained by sweeping the key coefficients. All the other coupling matrix entries need to be optimized to make different reconfigurable filter states meet the requirements. Details about the optimization are given in Section 3.3.

(5) Rotate the key coefficients to the diagonal entries of the coupling matrix. As a result, the effect of tuning the key coupling coefficients is equivalently achieved by shifting the resonant frequencies of certain resonators. Originally, all the resonators must be tuned to shift the center frequency of the filter. Therefore, after the key coefficients are transformed to diagonal positions of the coupling matrix, reconfigurable filter states can be realized without increasing the number of tuning elements.

(a) (b)

Figure 3.1 Sub-topology in the intermediate topology. (a) Quad sub-topology. (b) Hexa sub-topology

After introducing the synthesis procedure, the reconfigurable mechanism and the maximum number of controllable TZs for different filter orders will be investigated in detail. Two sub-topologies are introduced to explain how to reconfigure the state of a filter, as shown in Fig. 3.1 (Black circles: resonators. Black solid lines: constant couplings. Red solid lines: constant couplings chosen for these key coefficients). The quad and hexa sub-topology can control one and two pairs of TZs, respectively, according to the positions of key coefficients which are marked with red solid lines. However, there seems to be no regular pattern of coupling matrix rotations to transfer a folded configuration to a sub-topology-based configuration. Therefore, each order needs to be considered individually. The different coupling diagrams can be classified into three categories, namely quad-section, hexa-section, and mixed-section.

(a) (b)

Figure 3.2 Coupling topology of a fourth-order filter. (a) Folded configuration after coupling matrix synthesis. (b) Quad-section configuration after eliminating M_{23}

3.2.1 Multipath coupling diagram of quad-section

The quad sub-topology is shown in Fig. 3.1(a). Every four resonators can be employed to control a pair of symmetric TZs in the quad sub-topology. The minimum order to realize the quad-section topology is four. The coupling diagram is shown in Fig. 3.2(a) (Black circles: resonators. Hollow circles: terminals. Solid line segments: positive coupling. Dash line segments: negative coupling. Red arrows: resonant frequencies shifting) and the corresponding coupling matrix takes the following form

$$M = \begin{bmatrix} 0 & M_{S1} & 0 & 0 & 0 & 0 \\ M_{S1} & 0 & M_{12} & 0 & M_{14} & 0 \\ 0 & M_{12} & 0 & M_{23} & 0 & 0 \\ 0 & 0 & M_{23} & 0 & M_{34} & 0 \\ 0 & M_{14} & 0 & M_{34} & 0 & M_{4L} \\ 0 & 0 & 0 & 0 & M_{4L} & 0 \end{bmatrix} \tag{3.1}$$

The fourth-order configuration is a special case since the folded configuration is the same as the quadruplet configuration. If the sign of M_{14} is negative, the second row and column are then multiplied by -1 to make it positive. Similar procedures can be applied to make mainline couplings M_{S1} and M_{12} positive. Eventually, the only possible negative value in the coupling matrix is M_{23}.

The locations of TZs should satisfy the condition whereby the equation of S_{21} is equal to 0 [108].

$$S_{21} = \frac{P(s)}{\varepsilon E(s)} = 2\sqrt{R_S R_L}\,[y]_{N1} = 0 \tag{3.2}$$

where $P(s)$ and $E(s)$ are two polynomials with respect to the complex frequency variable s. ε is a real factor to normalize the highest-order coefficients in the two polynomials. R_S and R_L are the reference impedance of source and load, respectively. [y'] is the nodal admittance matrix. From (3.2), we can find that the positions of TZs should satisfy the following condition,

$$s^2 + M_{23}\left(M_{23} - \frac{M_{12}M_{34}}{M_{14}}\right) = 0 \tag{3.3}$$

Table 3.1 Relationship between value of M_{23} and location of TZs in the fourth-order filter

Value of M_{23}	Solution of s	Location of TZs
$M_{23} > 0$	Pure real	On the real axis
$M_{23} < 0$	Pure imaginary	On the imaginary axis

s has a pair of pure real or imaginary roots depending on whether M_{23} is positive or negative. In the generalized Chebyshev filters, $M_{12}^2/M_{14} \gg M_{23}$, which means that the TZs can be switched between pure real and pure imaginary, as summarized in Table 3.1. The key coefficient M_{23} changes its sign to reconfigure filtering characteristics, but the other reconfigured states may not meet the design requirements because the coupling matrix is initially synthesized based on one

possible set of TZs. Hence, optimization is necessary, which will be explained in detail in Section 3.3.

At last, the coupling matrix rotations [97-99] can be applied to rotate the key coefficient M_{23} in (3.4).

$$M^{(n+1)} = R \cdot M^{(n)} \cdot R^{T} \qquad (n = 1, 2, 3, ..) \tag{3.4}$$

where the new matrix $M^{(n+1)}$ has the same eigenvalues and eigenvectors as $M^{(n)}$. The rotation matrix R is defined by the pivot $[i, j]$, and the rotation angle θ_r. R^{T} is the transpose of R. In R, all the diagonal entries are 1 and off-diagonal entries are 0, except for $R_{ii} = R_{jj} = cos\theta_r$ and $R_{ji} = -R_{ij} = sin\theta_r$ ($i, j \neq 1$ or N+2, and $i \neq j$).

The rotation angle θ_{r1} can be calculated through

$$\theta_{r1} = \frac{1}{2}\tan^{-1}\left(\frac{2M_{i,j}}{M_{j,j} - M_{i,i}}\right) \tag{3.5}$$

Substituting $M_{22} = M_{33} = 0$ into (5) yields $\theta_{r1} = \pm\pi/4$. After applying (3.4) to the coupling matrix in (3.1), the coupling matrix becomes

$$M = \begin{bmatrix} 0 & M_{S1} & 0 & 0 & 0 & 0 \\ M_{S1} & 0 & \frac{M_{12}}{\sqrt{2}} & -\frac{M_{12}}{\sqrt{2}} & M_{14} & 0 \\ 0 & \frac{M_{12}}{\sqrt{2}} & M_{23} & 0 & \frac{M_{34}}{\sqrt{2}} & 0 \\ 0 & -\frac{M_{12}}{\sqrt{2}} & 0 & -M_{23} & \frac{M_{34}}{\sqrt{2}} & 0 \\ 0 & M_{14} & \frac{M_{34}}{\sqrt{2}} & \frac{M_{34}}{\sqrt{2}} & 0 & M_{S1} \\ 0 & 0 & 0 & 0 & M_{S1} & 0 \end{bmatrix} \tag{3.6}$$

This step aims to eliminate the coupling between resonators 2 and 3. At the same time, it creates non-zero elements on the diagonal of the coupling matrix, which can control the location of TZs. In this process, the reconfiguration mechanism of the filter is transformed from internal coupling coefficient tuning to resonant frequency tuning. The quad-section topology corresponding to the coupling matrix in (3.6) is depicted in Fig. 3.2(b). Tuning the resonant frequencies of resonator 2 and resonator 3 can reconfigure the state of the filter. This is the important step to realize center

frequencies tuning and reconfigurable responses at the same time by merely tuning resonant frequencies.

To independently control two pairs of TZs, cascaded quad-section topologies can be used with a minimum filter order of eight. Similar to the fourth-order topology, the eighth-order filter can be

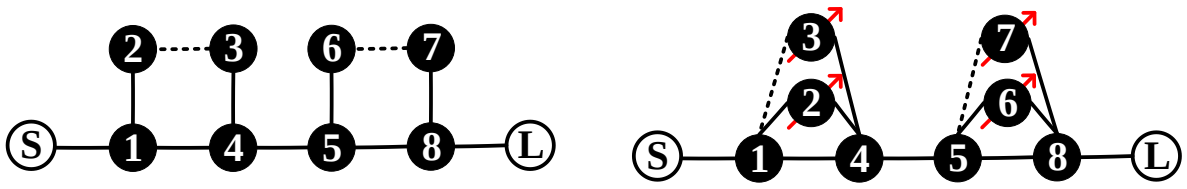

(a) (b)

Figure 3.3 Coupling topologies of eighth-order filter. (a) Cascaded quadruplet (CQ) configuration after coupling matrix rotations. (b) Final configuration after eliminating M_{23} and M_{67}

synthesized in a folded configuration with cross-couplings M_{36} and M_{27}, then the topology can be transformed into a CQ configuration by coupling matrix rotations. The detailed procedures of rotations are given in [97]. The CQ topology is drawn in Fig. 3.3(a) with the corresponding coupling matrix, shown as

$$M = \begin{bmatrix} 0 & M_{S1} & 0 & 0 & 0 & 0 & 0 & 0 & 0 & 0 \\ M_{S1} & 0 & M_{12} & 0 & M_{14} & 0 & 0 & 0 & 0 & 0 \\ 0 & M_{12} & 0 & M_{23} & 0 & 0 & 0 & 0 & 0 & 0 \\ 0 & 0 & M_{23} & 0 & M_{34} & 0 & 0 & 0 & 0 & 0 \\ 0 & M_{14} & 0 & M_{34} & 0 & M_{45} & 0 & 0 & 0 & 0 \\ 0 & 0 & 0 & 0 & M_{45} & 0 & M_{56} & 0 & M_{58} & 0 \\ 0 & 0 & 0 & 0 & 0 & M_{56} & 0 & M_{67} & 0 & 0 \\ 0 & 0 & 0 & 0 & 0 & 0 & M_{67} & 0 & M_{78} & 0 \\ 0 & 0 & 0 & 0 & 0 & M_{58} & 0 & M_{78} & 0 & M_{8L} \\ 0 & 0 & 0 & 0 & 0 & 0 & 0 & 0 & M_{8L} & 0 \end{bmatrix} \tag{3.7}$$

In (3.7), all the coefficients can be made positive by the aforementioned procedures, except for the possible negative values of M_{23} and M_{67}. The TZs satisfy the following condition based on (3.2).

$$\left[M_{14}s^2 + M_{23}\left(M_{14}M_{23} - M_{12}M_{34}\right)\right] * \left[M_{58}s^2 + M_{67}\left(M_{67}M_{58} - M_{56}M_{78}\right)\right] = 0 \tag{3.8}$$

The values of M_{23}, M_{12}, M_{14}, M_{34} and M_{67}, M_{56}, M_{58}, M_{78}, shown in blue and red in (3.7), respectively, can individually control a pair of TZs. M_{23} and M_{67} are chosen as the key coefficients to control the locations of TZs. For instance, if M_{23} or M_{67} is positive, the solutions of s are pure real because the mainline couplings are larger than those cross-couplings in the generalized Chebyshev filters (*i.e.*, $M_{14}M_{23}$-$M_{12}M_{34} < 0$, $M_{67}M_{58}$-$M_{56}M_{78} < 0$).

The final step is to annihilate the coupling coefficients M_{23} and M_{67} in (3.4) and (3.5). The two key coefficients are rotated to the diagonal entries of the coupling matrix with the same absolute values but opposite signs, shown as

$$M = \begin{bmatrix}
0 & M_{S1} & 0 & 0 & 0 & 0 & 0 & 0 & 0 & 0 \\
M_{S1} & 0 & \frac{M_{12}}{\sqrt{2}} & -\frac{M_{12}}{\sqrt{2}} & M_{14} & 0 & 0 & 0 & 0 & 0 \\
0 & \frac{M_{12}}{\sqrt{2}} & M_{23} & 0 & \frac{M_{34}}{\sqrt{2}} & 0 & 0 & 0 & 0 & 0 \\
0 & -\frac{M_{12}}{\sqrt{2}} & 0 & -M_{23} & \frac{M_{34}}{\sqrt{2}} & 0 & 0 & 0 & 0 & 0 \\
0 & M_{14} & \frac{M_{34}}{\sqrt{2}} & \frac{M_{34}}{\sqrt{2}} & 0 & M_{45} & 0 & 0 & 0 & 0 \\
0 & 0 & 0 & 0 & M_{45} & 0 & \frac{M_{56}}{\sqrt{2}} & -\frac{M_{56}}{\sqrt{2}} & M_{58} & 0 \\
0 & 0 & 0 & 0 & 0 & \frac{M_{56}}{\sqrt{2}} & M_{67} & 0 & \frac{M_{78}}{\sqrt{2}} & 0 \\
0 & 0 & 0 & 0 & 0 & -\frac{M_{56}}{\sqrt{2}} & 0 & -M_{67} & \frac{M_{78}}{\sqrt{2}} & 0 \\
0 & 0 & 0 & 0 & 0 & M_{58} & \frac{M_{78}}{\sqrt{2}} & \frac{M_{78}}{\sqrt{2}} & 0 & M_{8L} \\
0 & 0 & 0 & 0 & 0 & 0 & 0 & 0 & M_{8L} & 0
\end{bmatrix} \tag{3.9}$$

The coefficients corresponding to the resonant frequencies, *i.e.* resonators 2 and 3, resonators 6 and 7, can independently control a pair of symmetric TZs. Hence, four (2^2) different states in total can be achieved in the 8th-order filter. (3.6) and (3.9) show that the topology in Fig. 3.3(b) consists of two cascaded quad-section configurations, and their matrix coefficients are asymmetric about the principal diagonal.

In a 12th-order filter, the same synthesis technique can be applied. However, the coupling matrix rotations become much more complicated because three cascaded quad-sections need to be

reconfigured. The procedures of the coupling matrix rotations for a 12th-order filter using a quad-section topology are given step-by-step from the folded configuration. Fig. 3.4 shows the nonzero entries in the coupling matrix after rotations [97]. The following notations are adopted, such as $c_1 = cos\theta_1$, $t_1 = tan\theta_1$, *etc*. After each coupling matrix rotation, the notation M'_{ij} represents the matrix coefficient after the first rotation, *etc*. The details are shown below:

After the first rotation:

Pivot: M_{48}

$$M'_{34} = c_1 M_{34}$$

$$M'_{45} = c_1 M_{45} - s_1 M_{58}$$

$$M'_{78} = c_1 M_{78}$$

$$M'_{89} = s_1 M_{49} + c_1 M_{89}$$

$$M'_{47} = -s_1 M_{78}$$

$$M'_{49} = c_1 M_{49} - s_1 M_{89}$$

$$M'_{38} = s_1 M_{34}$$

$$M'_{58} = s_1 M_{45} + c_1 M_{58} \tag{3.10}$$

After the second rotation:

Pivot: M_{57}

$$M''_{45} = c_2 M'_{45} - s_2 M'_{47}$$

$$M''_{56} = c_2 M'_{56} - s_2 M'_{67}$$

$$M''_{67} = s_2 M'_{56} + c_2 M'_{67}$$

$$M''_{78} = s_2 M'_{58} + c_2 M'_{78}$$

$$M''_{47} = s_2 M'_{45} + c_2 M'_{47}$$

$$M''_{58} = c_2 M'_{58} - s_2 M'_{78} \tag{3.11}$$

After the third rotation:

Pivot: M_{68}

$$M'''_{56} = c_3 M''_{56} - s_3 M''_{58}$$

$$M'''_{67} = c_3 M''_{67} - s_3 M''_{78}$$

$$M'''_{78} = s_3 M''_{67} + c_3 M''_{78}$$

$$M'''_{89} = c_3 M''_{89}$$

$$M'''_{58} = s_3 M''_{56} + c_3 M''_{58} = 0$$

$$M'''_{38} = c_3 M''_{38}$$

$$M'''_{36} = -s_3 M''_{38}$$

$$M'''_{69} = -s_3 M''_{89} \tag{3.12}$$

After the fourth rotation:

Pivot: M_{79}

$$M^{IV}_{67} = c_4 M'''_{67} - s_4 M'''_{69}$$

$$M^{IV}_{78} = c_4 M'''_{78} - s_4 M'''_{89}$$

$$M^{IV}_{89} = s_4 M'''_{78} + c_4 M'''_{89}$$

$$M^{IV}_{910} = c_4 M'''_{910}$$

$$M^{IV}_{49} = s_4 M'''_{47} + c_4 M'''_{49} = 0$$

$$M^{IV}_{69} = s_4 M'''_{67} + c_4 M'''_{69} = 0$$

$$M^{IV}_{47} = c_4 M'''_{47} - s_4 M'''_{49}$$

$$M_{710}^{IV} = -s_4 M_{910}''' \tag{3.13}$$

After the fifth rotation:

Pivot: M_{810}

$$M_{310}^{V} = s_5 M_{38}^{IV} + c_5 M_{310}^{IV} = 0$$

$$M_{710}^{V} = s_5 M_{78}^{IV} + c_5 M_{710}^{IV} = 0 \tag{3.14}$$

c_1, s_1, c_2 and s_2 can be calculated using the above five rotations, and they should satisfy the following conditions,

$$\begin{aligned}
&c_2\left(M'_{38}M'_{910}M'_{49}M'_{56} - M'_{310}b\right) \\
&+s_2\left(-M'_{38}M'_{910}M'_{49}M'_{67} - M'_{310}a\right) = 0 \\
&c_2 s_2\left[\begin{array}{l} M'_{49}\left(M'^{2}_{56} - M'^{2}_{67} + M'^{2}_{58} - M'^{2}_{78}\right) - \\ M'_{89}\left(M'_{45}M'_{58} - M'_{47}M'_{78}\right) \end{array}\right] + \\
&s_2^2\left[M'_{49}\left(-M'_{56}M'_{67} - M'_{58}M'_{78}\right) + M'_{89}M'_{45}M'_{78}\right] + \\
&c_2^2\left[M'_{49}\left(M'_{56}M'_{67} + M'_{58}M'_{78}\right) - M'_{89}M'_{47}M'_{58}\right] = 0
\end{aligned} \tag{3.15}$$

where

$$a = M'_{45}M'_{56}M'_{78} - M'_{45}M'_{67}M'_{58} - M'_{89}M'_{49}M'_{67}$$

$$b = M'_{47}M'_{56}M'_{78} - M'_{47}M'_{67}M'_{58} + M'_{89}M'_{49}M'_{56} \tag{3.16}$$

Until now, the first two rotation angles can be calculated using scientific computational tools, such as MATLAB, *etc*. Eliminating M_{811} in the sixth rotation is easy, and the nonzero M_{912} will be created. The remaining steps are similar to the case of an 8th-order filter.

Table 3.2 Pivots and rotation angles for 12th filter order with quad-section topology

Degree N	Rotation No. R	Pivot [i, j]	$\theta r=\tan^{-1}(k\, M_{u1,u2}/M_{v1,v2})$					Annihilated elements
			u1	u2	v1	v2	k	
12	1	[4,8]					+1	
	2	[5,7]					+1	
	3	[6,8]	5	8	5	6	-1	M_{58}
	4	[7,9]	6	9	6	7	-1	M_{49}, M_{69}
	5	[8,10]	7	10	7	8	-1	M_{310}, M_{710}
	6	[9,11]	8	11	8	9	-1	M_{811}
	7	[4,6]					+1	
	8	[5,7]	4	7	4	5	-1	M_{47}
	9	[3,5]	3	6	5	6	+1	M_{36}, M_{38}
	10	[2,4]	2	5	4	5	+1	M_{25}
	11							M_{23}, M_{67}, M_{1011}

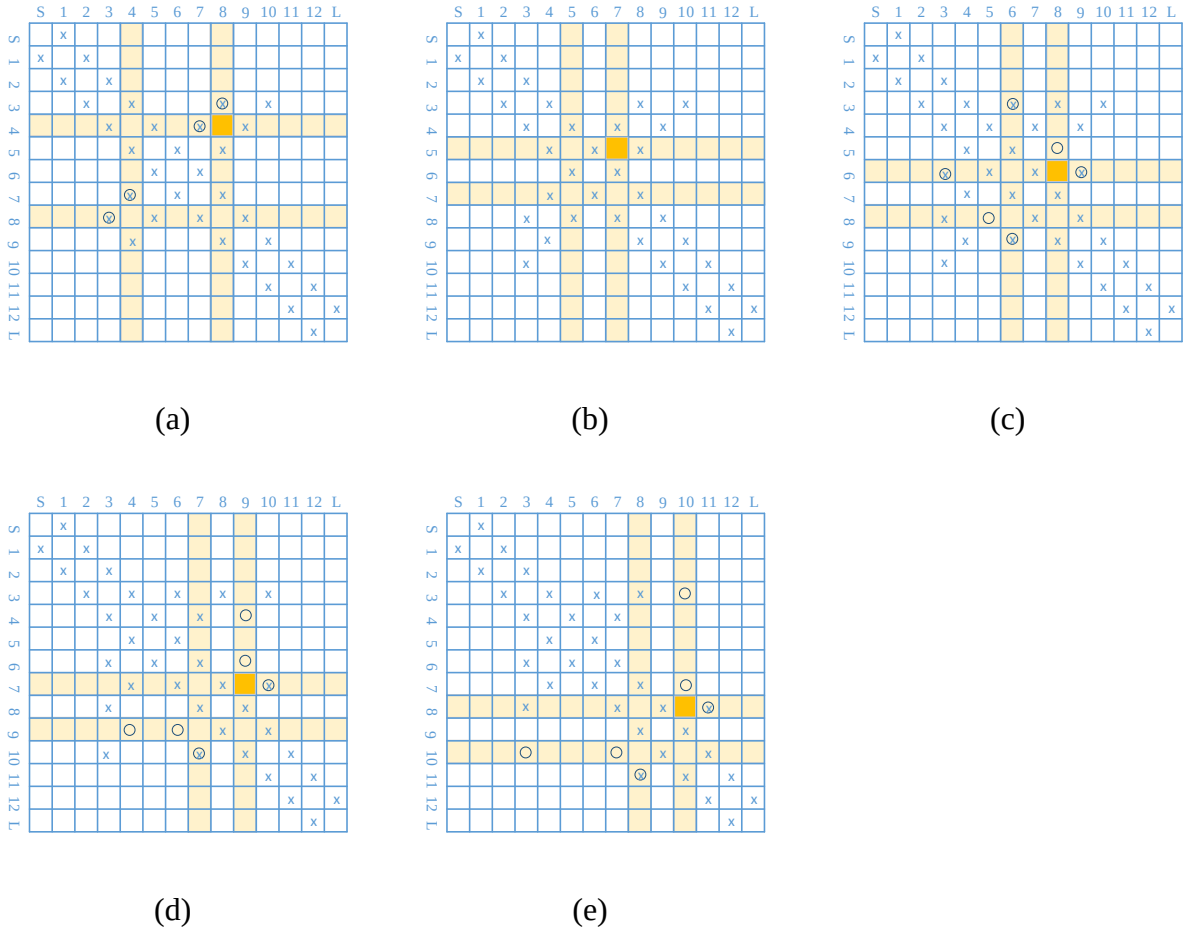

(a) (b) (c)

(d) (e)

Figure 3.4 Coupling matrix rotations for 12th-order filters. (a) Pivot: M_{48}. (b) Pivot: M_{57}. (c) Pivot: M_{68}. (d) Pivot: M_{79}. (e) Pivot: $M_{8,10}$

A detailed procedure is described in (3.10)-(3.16), and three pairs of TZs can be independently controlled by tuning resonant frequencies. There are eight (2^3) different states in terms of the reconfigured locations of TZs. The pivots and rotation angles for the 12th-order filter of cascaded quad-section topology are listed in Table 3.2. It is worth pointing out that a pair of symmetric TZs can be controlled by every four resonators in filters of other orders ($\geqslant$4). For example, 7th-order and 9th-order topology can have one and two pairs of independently controlled TZs, respectively. Their target topologies can be chosen with reference to the synthesis procedures of 4th-order and 8th-order topologies.

3.2.2 Multipath coupling diagram of hexa-section

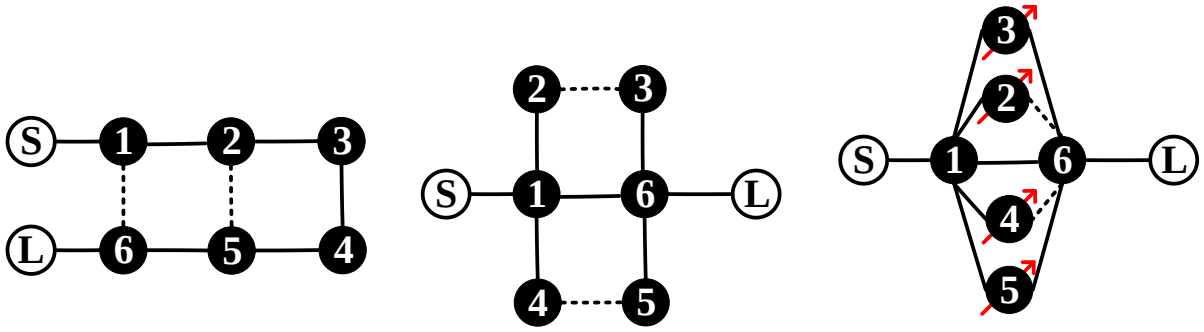

(a) (b) (c)

Figure 3.5 Coupling topologies of sixth-order filter. (a) Folded configuration after coupling matrix synthesis. (b) Six-section configuration after coupling matrix rotations. (c) Final configuration after eliminating M_{23} and M_{45}

The hexa sub-topology is shown in Fig. 3.1(b). Compared with a quad sub-topology, a hexa sub-topology can control more TZs, but its tuning mechanism is more complicated. In a hexa-section, the six resonators can dependently control two pairs of symmetric TZs. The synthesis procedure of a hexa-section also starts from a folded topology, as shown in Fig. 3.5(a). The transformation of the folded coupling matrix to a hexa-section form [97, 109] is illustrated in Fig. 3.6. Here, all the

nonzero entries are indicated with ‘X’; the newly created entries are represented by ‘⊗’; and the eliminated entries are marked as ‘○’. The first rotation angle θ_1 has an unknown value with the pivot [2, 4]. This operation aims to eliminate M_{25} and M_{34} simultaneously in the next step. The second rotation uses an angle θ_2 with the pivot [3, 5]. θ_2 can be calculated by (3.17).

$$\theta_2 = -\tan^{-1}\left(\frac{M_{j,k}}{M_{i,k}}\right) \tag{3.17}$$

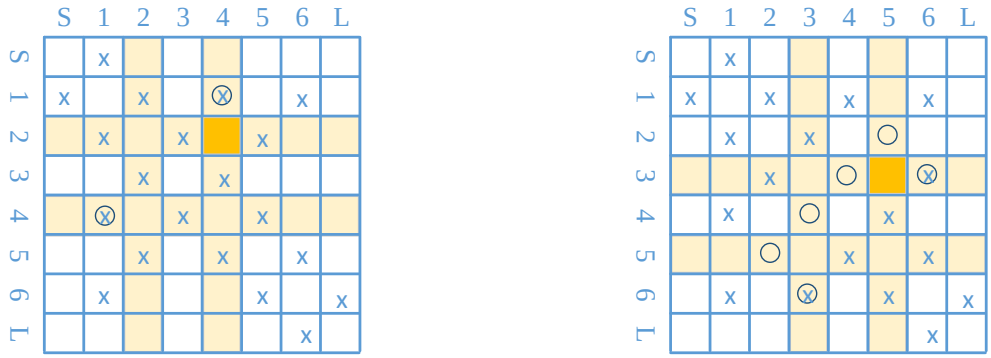

(a) (b)

Figure 3.6 Coupling matrix rotations from a folded topology to a hexa-section topology. (a) Rotation with unknown angle θ_1. (b) Rotation to eliminate M_{25}, M_{34} simultaneously

where $i = 3$, $j = 5$, $k = 2$. This step eliminates M_{25} and M_{34} simultaneously. To determine θ_1, coupling coefficients in rows i and j and columns i and j are calculated since only they will be changed by the rotation. In the following derivations, the simplified notations are adopted: $c_1 = cos\theta_1$, $t_1 = tan\theta_1$, and $s_1 = sin\theta_1$. After the coupling matrix rotations, M'_{ij} represents the matrix coefficient after the first rotation, *etc*. The details are shown below:

After the first rotation:

$$M'_{12} = c_1 M_{12}$$

$$M'_{23} = c_1 M_{23} - s_1 M_{34}$$

$$M'_{34} = s_1 M_{23} + c_1 M_{34}$$

$$M'_{45} = s_1 M_{25} + c_1 M_{45}$$

$$M'_{25} = c_1 M_{25} - s_1 M_{45}$$

$$M'_{14} = s_1 M_{12}\,. \tag{3.18}$$

After the second rotation:

$$M''_{25} = s_2 M'_{23} + c_2 M'_{25}$$

$$M''_{34} = c_2 M'_{34} - s_2 M'_{45}\,. \tag{3.19}$$

To enforce $M''_{25}$and M''_{34} in (3.19) to be zero simultaneously, t_2 is set to be $\frac{-M'_{25}}{M'_{23}}$ or $\frac{M'_{34}}{M'_{45}}$. Then, substituting into (3.18), t_1 can be expressed as follows:

$$\begin{aligned} &t_1^2\left(-M_{23}M_{34} - M_{25}M_{45}\right) + \\ &t_1\left(M_{23}^2 - M_{34}^2 + M_{25}^2 - M_{45}^2\right) + \\ &\left(M_{23}M_{34} + M_{25}M_{45}\right) = 0 \end{aligned} \tag{3.20}$$

As all the coefficients in (3.20) are known at the beginning, t_1 can be solved. The topology after the rotations is shown in Fig. 3.5(b). The locations of TZs can be calculated with (3.3) and the simplified equation is

$$\begin{aligned} &M_{16}\left(s^2 + M_{45}^2\right)\left(s^2 + M_{23}^2\right) - M_{12}M_{36}M_{23}\left(s^2 + M_{45}^2\right) \\ &-M_{14}M_{56}M_{45}\left(s^2 + M_{23}^2\right) = 0 \end{aligned} \tag{3.21}$$

It is difficult to directly obtain the relationship between the coupling coefficients and the locations of TZs from (3.21). However, two points are clear. First, the solutions of *s* can be pure real, pure imaginary, and conjugate complex values. Only the solutions of pure real and pure imaginary values (on the axes) will be discussed in this chapter. Second, the solutions of *s* can be controlled by the key coefficients M_{45} and M_{23} to change the locations of TZs. Theoretically, there are up to four different states, but the total number of states is limited by the coupling values in (3.21).

Finally, through (3.4) and (3.5), coupling coefficients M_{45} and M_{23} are rotated to the diagonal entries of the coupling matrix with coefficients M_{22}, M_{33}, M_{44}, and M_{55}. In other words, the reconfigurable filtering characteristics will be realized by tuning the resonant frequencies of resonators 2, 3, 4, and 5. The final hexa-section topology is shown in Fig. 3.5(c).

The 12th-order filter can have two cascaded hexa-sections. Each hexa-section can control two pairs of TZs independently. Hence, the 12th-order filter has up to sixteen (2^4) different states. The coupling matrix transformation from the folded topology to the cascaded hexa-section topology is

Table 3.3 Pivots and rotation angles for hexa-section topology for different filter orders

Degree N	Rotation No. R	Pivot [i,j]	$\theta r=\tan^{-1}(k\, M_{u1,u2}/M_{v1,v2})$					Annihilated elements
			u1	u2	v1	v2	k	
6	1	[2,4]						
	2	[3,5]	2	5	2	3	-1	M_{25}, M_{34}
	3							M_{23}, M_{45}
12	1	[3,9]					+1	
	2	[4,8]					+1	
	3	[5,7]					+1	
	4	[6,8]	5	8	5	6	-1	M_{58}
	5	[7,9]	6	9	6	7	-1	M_{49}, M_{69}
	6	[8,10]	7	10	7	8	-1	M_{310}, M_{710}
	7	[9,11]	8	11	8	9	-1	M_{211}, M_{811}
	8	[3,7]					+1	
	9	[4,6]					+1	
	10	[5,7]	4	7	4	5	-1	M_{47}
	11	[6,8]	5	8	5	6	-1	M_{58}, M_{38}
	12	[7,9]	6	9	6	7	-1	M_{29}, M_{69}
	13	[8,10]	7	10	7	8	-1	M_{710}
	14	[9,11]					+1	M_{912}
	15	[3,5]					+1	
	16	[2,6]	2	7	6	7	+1	M_{27}, M_{36}
	17	[2,4]					+1	
	18	[3,5]	2	5	2	3	-1	M_{25}, M_{34}
	19	[8,10]					+1	
	20	[9,11]	8	11	8	9	-1	M_{811}, M_{910}
	21							M_{23}, M_{45}, M_{89}, M_{1011}

very complicated. 21 rotations are needed to reconfigure the coupling matrix. The pivots and the rotation angles of the hexa-section topology are listed in Table 3.3 for different filter orders. Like the quad-section topology, each pair of symmetric TZs can be controlled using similar coupling matrix rotations. For instance, the 7^{th}-order topology can control two pairs of TZs referring to the 6^{th}-order topology's rotation.

3.2.3 Multipath coupling diagram of mixed-section

As discussed above, the quad-section and hexa-section can be used as building blocks to control one and two pairs of symmetric TZs, respectively. They can be connected in different ways to extend the diversity of responses and realizations. In Fig. 3.7, some coupling topologies consisting of different sub-sections are illustrated to realize different characteristics. In Fig. 3.7(a), two quad-sections in parallel have the same responses as the cascaded quartet topology, though their coupling diagrams are different, leading to better flexibility in the physical design. Additionally, the quad-section topology is cascaded with the hexa-section topology to control three pairs of TZs in total, as shown in Fig. 3.7(b), which is a hybrid form between the pure quad- and hexa-section topologies. The mixed-section topology provides a tradeoff between these two topologies to realize the same number of symmetric TZs with a lower order of the filter.

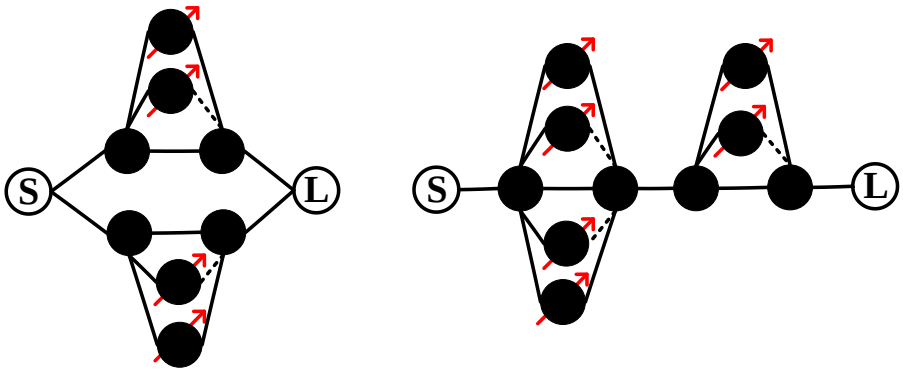

(a) (b)

Figure 3.7 Possible coupling topologies of mixed-section. (a) Two quad-section topologies in parallel. (b) Cascading of a quad-section topology and a hexa-section topology

3.3 Optimization

Since the initial coupling matrix is synthesized based on one possible set of TZs, the performance of other reconfigurable states, especially, the return loss level, may deteriorate when the key coefficients change their signs or values. Hence, the initial coupling matrix needs to be optimized to make a tradeoff among all states with respect to the design specifications. The optimization procedure mainly contains four steps:

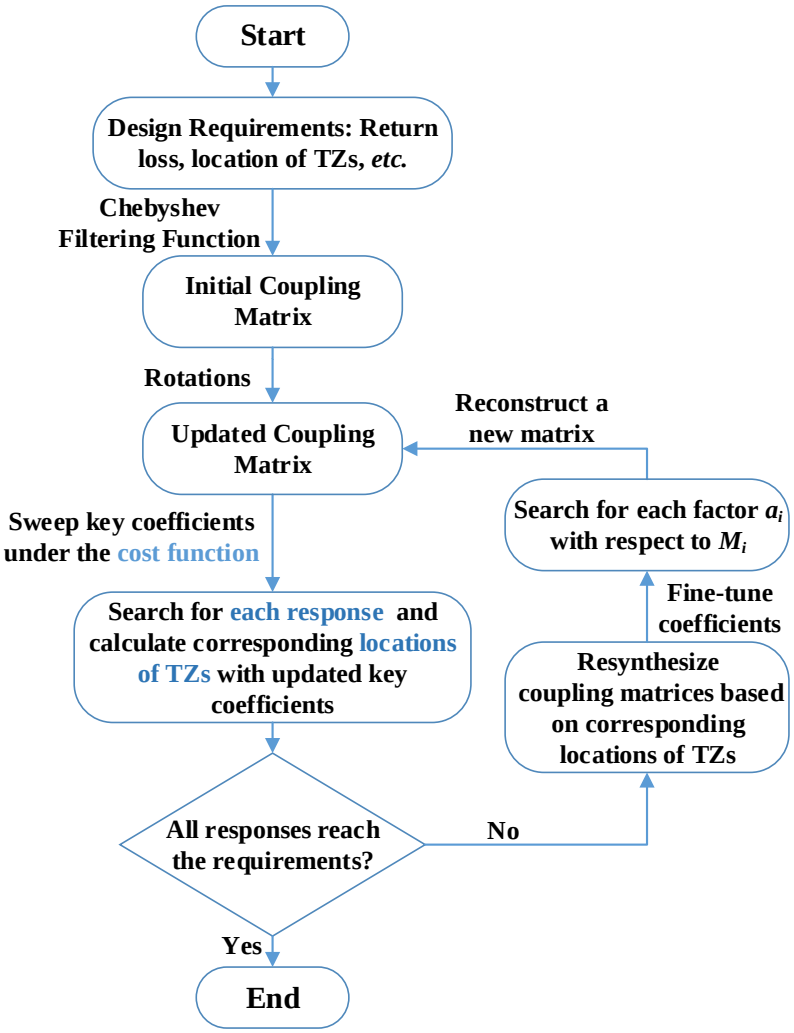

Figure 3.8 Flow chart for coupling matrix optimization

Step 1: Change the value of the key coefficient to reconfigure filter characteristics.

Following the procedure described in Section 3.2, a coupling matrix with an intermediate topology has been synthesized. The positions of key coefficients are given in Fig. 3.1 to reconfigure the locations of TZs. The final values of the key coefficients are determined to optimally satisfy the system requirements on the reconfigurable filter, such as return loss level, group delay flatness, and out-of-band rejection, *etc*. For example, the following cost function can be used to evaluate the filter performance in terms of the in-band return loss and the stopband rejection as:

$$\begin{aligned} C = & \max\left\{ dB\left(S_{11}\right) \text{in} \quad \text{passband}, -r_{in} \right\} \\ & + w \cdot \max\left\{ dB\left(S_{21}\right) \text{in} \quad \text{stopband}, -r_{out} \right\} \end{aligned} \tag{3.22}$$

where r_{in} and r_{out} are the prescribed in-band return loss level and stopband rejection level, respectively. w is a predefined weight factor. The reconfigurable states are determined with a set of key coefficient values that can minimize C. Note that the initial coupling matrix should be synthesized for the reconfigurable states with the most challenging specifications.

Step 2: Check whether the performances of all reconfigurable states meet design requirements. If not, synthesize a coupling matrix for each reconfigurable state.

Usually, it is the return loss levels of reconfigurable states that do not meet design specifications. If the performances of some reconfigurable states are not satisfactory, then for each state, resynthesize a coupling matrix based on the calculated locations of TZs of that state. So if there are N reconfigurable states, there will be N synthesized coupling matrices. Note that all the N coupling matrices should be reconfigured to the same intermediate coupling topology as the initial matrix obtained in step 1.

Step 3: Fine-tune the coefficients to obtain the final coupling matrix.

N coupling matrices are synthesized in step 2. However, we can use only one final coupling matrix to guide and enable the physical realization of the filter. The final coupling matrix should make a compromise among all the reconfigurable states. Therefore, each of its coefficients is fine-tuned within the range whose the lower and upper bounds are determined by the minimum and maximum values in the corresponding positions of the N coupling matrices obtained in step 2. Direct optimization of all the coefficients to construct a new coupling matrix that can give satisfactory

performance for all reconfigurable states is time-consuming due to too many optimization variables. Therefore, we introduce a simple approach to derive the final coupling matrix. The final coupling matrix M_F is determined by the weighted sum of all the matrices obtained in step 2 as follows,

$$M_F = a_1 * M_1 + a_2 * M_2 \ldots + a_i * M_i \ldots + a_N * M_N, \tag{3.23}$$

where a_i is the weight factor for the coupling matrix M_i, and M_i is the synthesized coupling matrix for the i^{th} reconfigurable state. The values of a_i satisfy $a_1 + a_2 + \cdots + a_i + \cdots + a_N = 1$, and $a_i \geq 0$.

With (3.23), the optimization variables are converted from the non-zero coefficients in the coupling matrix to the weight factors a_1 to a_N. In this way, the number of optimization variables can be reduced because the number of states N is often smaller than the total number of non-zero coefficients in the coupling matrix. The optimal solution stemmed from the optimization procedure can be found because it is a brute-force method by sweeping all the variables in the corresponding dynamic range. An appropriate set of weight factors can be determined by an exhaustive parameter sweep to make all the reconfigurable states of M_F have close return loss levels. Then, M_F gives the best performance of all states. According to our experience, it is not necessary to optimize all the a_i's values. Usually, the lower and upper bounds of all the coupling coefficients are determined by only two matrices, whose TZs are all on the real axis and the imaginary axis of the complex plane, respectively. Satisfactory results can be obtained if we set all the a_i's zero, except the two for the above two matrices. Then the number of non-zero weight factors is decreased to two to reduce the amount of calculation.

Step 4: Repeat steps 1 to 3 until all the states meet the design requirements.

If sweeping a_i in (3.23) fails to make all reconfigurable states meet the design requirements, we can resynthesize the coupling matrices with a higher return loss level at the beginning. Then repeat steps 1 to 3, until all the states meet the design specifications. The flow chart of coupling matrix optimization is shown in Fig. 3.8. The whole procedure can be programmed using scientific computational tools, such as MATLAB, to optimize the final matrix.

In the following sections, two syntheses and one design example are illustrated to show how to implement the optimization steps.

3.4 Synthesis examples

3.4.1 A fourth-order filter with two reconfigurable states

A fourth-order reconfigurable filter with one pair of TZs is taken as the first example. The return loss levels of both reconfigurable states should be better than 22 dB. One of the states gives group delay equalization over 70% of the passband.

$$\begin{bmatrix} 0 & 1.0989 & 0 & 0 & 0 & 0 \\ 1.0989 & 0 & 0.9894 & 0 & 0.1927 & 0 \\ 0 & 0.9894 & 0 & 0.6526 & 0 & 0 \\ 0 & 0 & 0.6526 & 0 & 0.9894 & 0 \\ 0 & 0.1927 & 0 & 0.9894 & 0 & 1.0989 \\ 0 & 0 & 0 & 0 & 1.0989 & 0 \end{bmatrix}$$

(a)

$$\begin{bmatrix} 0 & 1.0937 & 0 & 0 & 0 & 0 \\ 1.0937 & 0 & 0.9476 & 0 & 0.1590 & 0 \\ 0 & 0.9476 & 0 & -0.7980 & 0 & 0 \\ 0 & 0 & -0.7980 & 0 & 0.9476 & 0 \\ 0 & 0.1590 & 0 & 0.9476 & 0 & 1.0937 \\ 0 & 0 & 0 & 0 & 1.0937 & 0 \end{bmatrix}$$

(b)

$$\begin{bmatrix} 0 & 1.0953 & 0 & 0 & 0 & 0 \\ 1.0953 & 0 & 0.9601 & 0 & 0.1691 & 0 \\ 0 & 0.9601 & 0 & -0.3628 & 0 & 0 \\ 0 & 0 & -0.3628 & 0 & 0.9601 & 0 \\ 0 & 0.1691 & 0 & 0.9601 & 0 & 1.0953 \\ 0 & 0 & 0 & 0 & 1.0953 & 0 \end{bmatrix}$$

(c)

$$\begin{bmatrix} 0 & 1.0953 & 0 & 0 & 0 & 0 \\ 1.0953 & 0 & 0.6789 & -0.6789 & 0.1691 & 0 \\ 0 & 0.6789 & -0.8181 & 0 & 0.6789 & 0 \\ 0 & -0.6789 & 0 & 0.8181 & 0.6789 & 0 \\ 0 & 0.1691 & 0.6789 & 0.6789 & 0 & 1.0953 \\ 0 & 0 & 0 & 0 & 1.0953 & 0 \end{bmatrix}$$

(d)

Figure 3.9 Coupling matrix of a fourth-order filter obtained by an analytical synthesized procedure. (a) Simplified coupling matrix with folded topology synthesized from the Chebyshev filtering function. (b) The second matrix synthesized from the Chebyshev filter function with the return loss of 23 dB and the TZs of ±2.2681j rad/s. (c) The optimized matrix with weight factor of 0.3 and 0.7 according to the matrices in (a) and (b), respectively. (d) The final matrix after rotating coefficient M_{23}, where M_{23} = -0.8181 in the matrix before rotation

Step 1: The initial matrix is synthesized from the Chebyshev filtering function with the prescribed TZs at ±1.7 rad/s and a return loss of 22 dB. The initial coupling matrix is shown in Fig. 3.9(a).

As analyzed in Section 3.2, the pair of TZs can be controlled by tuning the key coefficient M_{23} in the quad sub-topology. As seen in (3.3) and Table 3.1, there are two reconfigurable states corresponding to a positive and a negative value of M_{23}. The coupling matrix with a positive M_{23} (i.e., 0.6526) is initially synthesized from the Chebyshev filtering function, as shown in Fig. 3.9(a). The location of TZs is placed on the real axis of the complex plane in this state. The other state can be found by sweeping the negative values of M_{23} to minimize the cost function (3.23). The S-parameters under different values of M_{23} are plotted in Fig. 3.10(a). It is seen that the in-band return loss level is affected

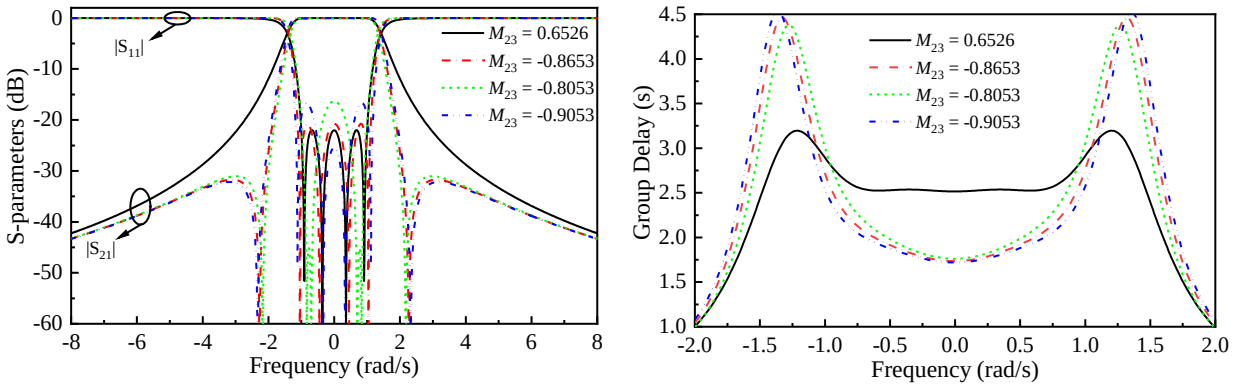

(a) (b)

Figure 3.10 The responses by sweeping the key coefficients M_{23}. (a) S-parameters. (b) Group delay

by the value of the key coefficient M_{23}. The best return loss level of the second reconfigurable state is 20.7453 dB, which is obtained by a negative M_{23} (i.e., -0.8653). The positions of TZs on the imaginary axis of the complex plane are also changed with different negative values of M_{23}, which can be calculated by (3.3). Substituting M_{23} = -0.8653 into (3.3), the values of TZs are ±2.2681j rad/s.

At the same time, the group delay flatness is also affected by tuning M_{23}, as shown in Fig. 3.10(b). When the location of TZs is switched from the real axis to the imaginary axis of the complex plane, the near-skirt selectivity of the filter becomes better, but the in-band group delay flatness becomes worse.

Step 2: It is seen that the state with TZs on the imaginary axis of the complex plane has deteriorated return loss performance. Hence, the coupling matrix needs to be resynthesized for the second reconfigurable state. In general, the return loss levels of reconfigured filter states will be slightly lower than that of the initially synthesized state. Therefore, the return loss level used in the analytical synthesis procedure can be chosen slightly higher than the required level. In this example, the coupling matrix is resynthesized based on the TZs of ±2.2681j rad/s and the return loss of 23 dB, in order to meet the return loss requirement of 22 dB. The synthesized coupling matrix is given in Fig. 3.9(b). The next step is adjusting all the coefficients in the coupling matrix.

Table 3.4 Performance of two states after fine-tuning the key coefficient and locations of TZs

No. of states	M_{23}	Return loss (dB)	Locations of TZs
1	0.6411	22.3975	±1.7561
2	-0.8181	22.2752	±2.2647j

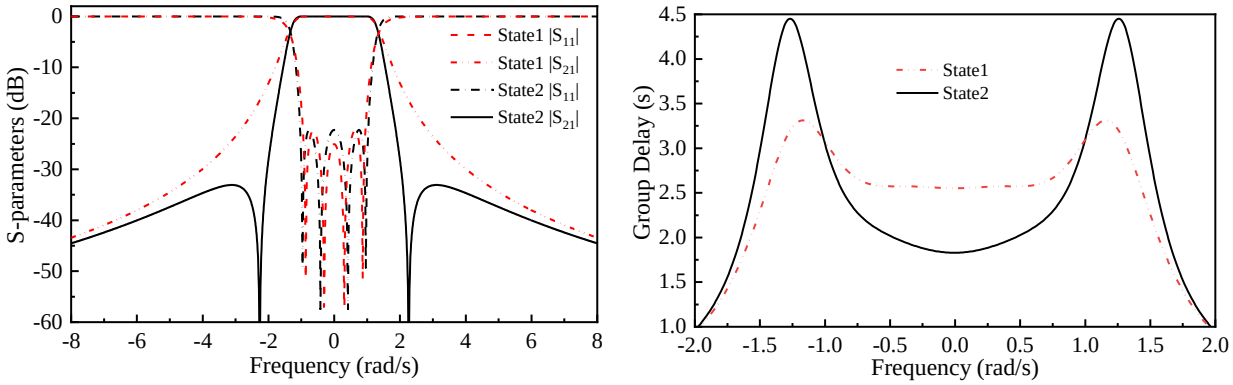

(a) (b)

Figure 3.11 The responses of two states for the fourth-order filter after optimization. (a) Magnitude of S-parameters. (b) Group delay

Step 3: Implementing the simplified adjustment-based method, the final matrix is given in Fig. 3.9(c). It is obtained with the weight factor of a_1 = 0.3 and a_2 = 0.7 according to the matrices in Fig. 3.9(a) and Fig. 3.9(b), respectively. Repeating steps 1 to 2 with the matrix in Fig. 3.9(c), the

return loss level and the locations of TZs are updated in Table 3.4. Finally, the return loss levels of both states are better than 22 dB. The magnitude and group delay responses of both states are shown in Fig. 3.11(a) and Fig. 3.11(b), respectively (State1: TZs on the real axis of the complex plane. State2: TZs on the imaginary axis of the complex plane). The group delay equalization of the first state with TZs on the real axis of the complex plane is over 70% of the passband.

With the coupling matrix in the intermediate topology, the states can be reconfigured by merely tuning the key coefficient M_{23}. The last step is to rotate the intermediate coupling matrix using (3.4) and (3.5). The resultant matrix is given in Fig. 3.9(d), which is eventually transformed to the quad-section based topology. Now different reconfigurable filter states can be realized by tuning the resonant frequencies of resonators 2 and 3 without modifying any other coefficient. The center frequency tuning and the reconfigurable state control can be realized by tuning all resonant frequencies simultaneously.

3.4.2 An eighth-order filter with four reconfigurable states

An eighth-order reconfigurable filter with two pairs of TZs is taken as the second example. In this example, the return loss of all states should be better than 23 dB, and one of the states gives out-of-band rejection better than 85 dB when the normalized frequency > 2 rad/s.

Table 3.5 Coefficients of S-parameter polynomials

s^i, i=	$E(s)$	$F(s)$	$P(s)$
0	0.1343	0.0095	36
1	0.7437	0	0
2	2.1265	0.2794	13
3	3.9646	0	0
4	5.5134	1.3268	1
5	5.4780	0	
6	4.4576	2.0506	
7	2.1941	0	
8	1	1	
ε = 268.6451, ε_R = 1			

Step 1: The initial values of TZs are ±2j and ±3j rad/s, and the return loss level is 23 dB. The transfer and reflection characteristics can be synthesized from the generalized Chebyshev filtering function. The coefficients of the polynomials are given in Table 3.5. The simplified coupling matrix in the folded topology is obtained and shown in Fig. 12(a). Rotating the folded topology to the cascaded CQ topology has been introduced in [97]. The first rotating angle is calculated that $tan\theta$ = -0.0926 or -0.0354. After completing the matrix rotations, the matrix in the CQ topology is shown in Fig. 3.12(b). As can be seen, all the coefficients are positive except for M_{23} and M_{67}.

As analyzed in Section 3.2, these two pairs of TZs can be independently controlled by sweeping the key coefficients M_{23} and M_{67} in the quad sub-topology. There are four reconfigurable states based on the locations of TZs. In this case, it can be seen from (3.8) that these four states are

$$\begin{bmatrix}
0 & 1.0474 & 0 & 0 & 0 & 0 & 0 & 0 & 0 & 0 \\
1.0474 & 0 & 0.8703 & 0 & 0 & 0 & 0 & 0 & 0 & 0 \\
0 & 0.8703 & 0 & 0.6057 & 0 & 0 & 0 & 0.0022 & 0 & 0 \\
0 & 0 & 0.6057 & 0 & 0.5557 & 0 & -0.0732 & 0 & 0 & 0 \\
0 & 0 & 0 & 0.5557 & 0 & 0.6187 & 0 & 0 & 0 & 0 \\
0 & 0 & 0 & 0 & 0.6187 & 0 & 0.5557 & 0 & 0 & 0 \\
0 & 0 & 0 & -0.0732 & 0 & 0.5557 & 0 & 0.6057 & 0 & 0 \\
0 & 0 & 0.0022 & 0 & 0 & 0 & 0.6057 & 0 & 0.8703 & 0 \\
0 & 0 & 0 & 0 & 0 & 0 & 0 & 0.8703 & 0 & 1.0474 \\
0 & 0 & 0 & 0 & 0 & 0 & 0 & 0 & 1.0474 & 0
\end{bmatrix}$$

(a)

$$\begin{bmatrix}
0 & 1.0474 & 0 & 0 & 0 & 0 & 0 & 0 & 0 & 0 \\
1.0474 & 0 & 0.8658 & 0 & 0.0886 & 0 & 0 & 0 & 0 & 0 \\
0 & 0.8658 & 0 & -0.6622 & 0 & 0 & 0 & 0 & 0 & 0 \\
0 & 0 & -0.6622 & 0 & 0.5462 & 0 & 0 & 0 & 0 & 0 \\
0 & 0.0886 & 0 & 0.5462 & 0 & 0.5478 & 0 & 0 & 0 & 0 \\
0 & 0 & 0 & 0 & 0.5478 & 0 & 0.5555 & 0 & 0.0342 & 0 \\
0 & 0 & 0 & 0 & 0 & 0.5555 & 0 & -0.6276 & 0 & 0 \\
0 & 0 & 0 & 0 & 0 & 0 & -0.6276 & 0 & 0.8696 & 0 \\
0 & 0 & 0 & 0 & 0 & 0.0342 & 0 & 0.8696 & 0 & 1.0474 \\
0 & 0 & 0 & 0 & 0 & 0 & 0 & 0 & 1.0474 & 0
\end{bmatrix}$$

(b)

$$\begin{bmatrix}
0 & 1.0489 & 0 & 0 & 0 & 0 & 0 & 0 & 0 & 0 \\
1.0489 & 0 & 0.8682 & 0 & 0.0917 & 0 & 0 & 0 & 0 & 0 \\
0 & 0.8682 & 0 & -0.6670 & 0 & 0 & 0 & 0 & 0 & 0 \\
0 & 0 & -0.6670 & 0 & 0.5567 & 0 & 0 & 0 & 0 & 0 \\
0 & 0.0917 & 0 & 0.5567 & 0 & 0.5532 & 0 & 0 & 0 & 0 \\
0 & 0 & 0 & 0 & 0.5532 & 0 & 0.5615 & 0 & 0.0345 & 0 \\
0 & 0 & 0 & 0 & 0 & 0.5615 & 0 & -0.6380 & 0 & 0 \\
0 & 0 & 0 & 0 & 0 & 0 & -0.6380 & 0 & 0.8723 & 0 \\
0 & 0 & 0 & 0 & 0 & 0.0345 & 0 & 0.8723 & 0 & 1.0489 \\
0 & 0 & 0 & 0 & 0 & 0 & 0 & 0 & 1.0489 & 0
\end{bmatrix}$$

(c)

$$\begin{bmatrix}
0 & 1.0489 & 0 & 0 & 0 & 0 & 0 & 0 & 0 & 0 \\
1.0489 & 0 & 0.6139 & -0.6139 & 0.0917 & 0 & 0 & 0 & 0 & 0 \\
0 & 0.6139 & -0.6670 & 0 & 0.3936 & 0 & 0 & 0 & 0 & 0 \\
0 & -0.6139 & 0 & 0.6670 & 0.3936 & 0 & 0 & 0 & 0 & 0 \\
0 & 0.0917 & 0.3936 & 0.3936 & 0 & 0.5532 & 0 & 0 & 0 & 0 \\
0 & 0 & 0 & 0 & 0.5532 & 0 & 0.3970 & -0.3970 & 0.0345 & 0 \\
0 & 0 & 0 & 0 & 0 & 0.3970 & -0.6380 & 0 & 0.6168 & 0 \\
0 & 0 & 0 & 0 & 0 & -0.3970 & 0 & 0.6380 & 0.6168 & 0 \\
0 & 0 & 0 & 0 & 0 & 0.0345 & 0.6168 & 0.6168 & 0 & 1.0489 \\
0 & 0 & 0 & 0 & 0 & 0 & 0 & 0 & 1.0489 & 0
\end{bmatrix}$$

(d)

Figure 3.12 Coupling matrix obtained during synthesized procedures. (a) Simplified coupling matrix with folded topology synthesized from the Chebyshev filtering function. (b) Topology transformed after coupling matrix rotations. (c) Optimized coupling matrix with coefficients fine-tuning. (d) Final coupling matrix after rotating coefficients M_{23} and M_{67}

obtained by positive and negative values of the key coefficients M_{23} and M_{67} (positive M_{23}, positive M_{67}; positive M_{23}, negative M_{67}; negative M_{23}, positive M_{67}; negative M_{23}, negative M_{67}). The coupling matrix with negative M_{23} and negative M_{67} is given in Fig. 3.12(b). The coupling matrices corresponding to the other three states can be found by sweeping the key coefficients M_{23} and M_{67} to minimize the cost function (3.23). The four reconfigurable states are summarized in Table 3.6. As can be seen, the return loss level of states 2 to 4 is slightly worse and does not meet the design requirements.

Table 3.6 Comparison of filter performance before and after optimization with related coefficients and locations of TZs

No. of States	M_{23}	M_{67}	Return Loss (dB)	Location of TZs
Before fine-tuning coupling matrix coefficients (Before step 3)				
1	-0.6622	-0.6276	23.0000	±2.0000j, ±3.0000j
2	0.5360	-0.6200	20.5050	±1.6042, ±3.0235j
3	-0.6661	0.5760	22.2331	±1.9912j, ±2.7936
4	0.5240	0.5700	20.2532	±1.5882, ±2.7796
After fine-tuning coupling matrix coefficients (After step 3)				
1	-0.6670	-0.6380	21.3203	±1.9901j, ±3.0765j
2	0.5430	-0.6280	21.4306	±1.6022, ±3.0512j
3	-0.6630	0.5920	21.9157	±1.9834j, ±2.8380
4	0.5340	0.5760	21.2592	±1.5904, ±2.8010

Step 2: Three coupling matrices for states 2 to 4 are resynthesized based on the values of TZs of states 2 to 4 in Table 3.6 and the return loss of 23 dB.

Step 3: Fine-tune all the coefficients in the coupling matrix using the simplified sweeping-based method. Each coefficient has a dynamic range determined by the corresponding minimum and maximum values in the four matrices. For instance, $M_{12} \in [0.8658, 0.8727]$. It can be observed that the matrices of states 1 and 4 determine the coefficients' dynamic range. All the coefficients in the matrices of states 2 and 3 are within the corresponding range. Therefore, a_2 and a_3 are set to zero, and the constraint on weight factors is simplified to $a_1 + a_4 = 1$. Implementing the sweeping-based method, the final matrix is obtained with weight factors of $a_1 = 0.65$, $a_2 = 0$, $a_3 = 0$, and $a_4 = 0.35$ according to the four matrices corresponding to states 1 to 4, as shown in Fig. 3.12(c). Repeating steps 1 to 2, the return loss levels and the locations of TZs after fine-tuning coefficients in the matrix are updated in Table 3.6. The return loss levels of different states are close to each other and are all better than 21.2 dB. The S-parameters and the group delay responses are plotted in Fig. 3.13(a) and in Fig. 3.13(b), respectively. As can be seen, the locations of the TZs have a great impact on the filtering characteristics. The more TZs distributed on the imaginary axis of the complex plane, the better the out-of-band suppression is. On the contrary, the more TZs deployed on the real axis of the complex plane, the flatter the group delay is.

Step 4: Repeat steps 1 to 3 until all the states meet the design requirements. Even though all the return loss levels are better than 21.2 dB, they are not meet the target. A higher level of return loss can be used to synthesize matrices, such as 25 dB at the beginning. Because the rest of the procedure is very similar, leave it to the readers to complete.

Till now, in the intermediate topology, the responses can be reconfigured by controlling the key coefficients M_{23} and M_{67}. The last step is to rotate the intermediate coupling matrix using (3.4) and (3.5). The resultant matrix is given in Fig. 3.12(d), which is eventually transformed into the quad-section based topology. Now the filter states can be reconfigured by tuning the resonant frequencies of resonators 2, 3, 6, and 7.

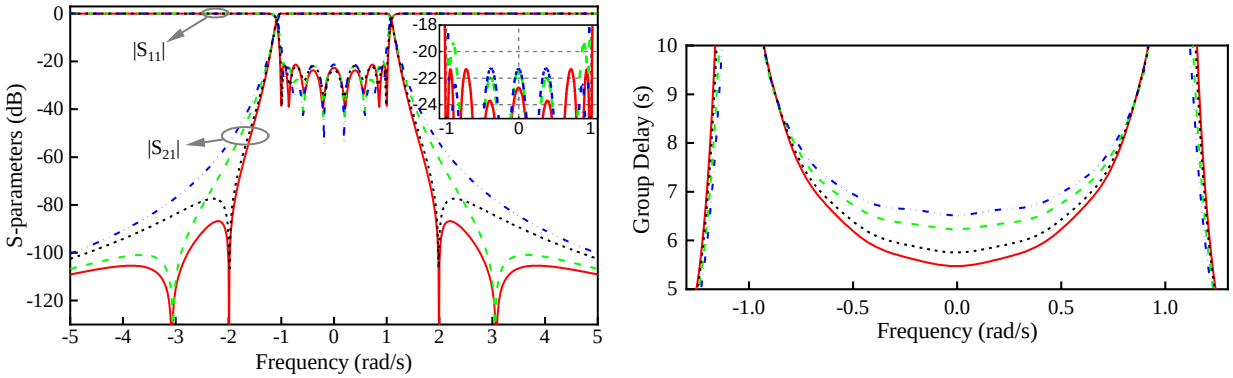

(a) (b)

Figure 3.13 Comparison of states after coupling matrix optimization. (a) S-parameters responses after optimization. (b) Group delay responses after optimization corresponding to the curves in Fig. 3.13(a) using the same color

3.5 Experimental validation

To experimentally validate the proposed theory and techniques, a fourth-order reconfigurable bandpass filter is fabricated and measured. It has two states and both states can be tuned from 9.5 GHz to 10.6 GHz. The filter is initially designed with a center frequency of 10.56 GHz and a bandwidth of 300 MHz. It has two symmetric TZs located at ±4.5j, and the in-band return loss is 28 dB. The choice of a higher level of return loss is mainly done by considering the deterioration of filter performance after the center frequency tuning to a lower frequency.

3.5.1 Coupling matrix synthesis

First, the coupling matrix is synthesized from the generalized Chebyshev filtering function. After simplification, the obtained coupling matrix is shown in Fig. 3.14(a). The only negative coupling is M_{23} = -0.8387, and all the other inter-resonator couplings are positive.

Second, sweep the key coefficient M_{23} to find reconfigurable states by minimizing the cost function in (3.23). There are two states. One state with the negative value of M_{23} (i.e., -0.8387) is initially

synthesized. The other state is found by sweeping the positive values of M_{23}. The value of M_{23} is 0.7840, which gives a return loss of 28.5138 dB.

The corresponding return loss performance and locations of TZs with the suitable values of M_{23} are summarized in Table 3.7. As can be seen, both states meet the design requirements. Therefore, the fine-tuning coefficients in the matrix is not necessary in this example. The final matrix M_F is the same as the initial matrix in Fig. 3.14(a).

Table 3.7 Corresponding return loss performance and location of TZs with suitable value of M_{23}

No. of States	M_{23}	Solution of s	Return Loss (dB)	Location of TZs
1	0.7840	Pure real	28.5138	±4.2014
2	-0.8387	Pure imaginary	28.0000	±4.5000j

$$\begin{bmatrix} 0 & 1.2176 & 0 & 0 & 0 & 0 \\ 1.2176 & 0 & 1.1175 & 0 & 0.0536 & 0 \\ 0 & 1.1175 & 0 & -0.8387 & 0 & 0 \\ 0 & 0 & -0.8387 & 0 & 1.1175 & 0 \\ 0 & 0.0536 & 0 & 1.1175 & 0 & 1.2176 \\ 0 & 0 & 0 & 0 & 1.2176 & 0 \end{bmatrix} \qquad \begin{bmatrix} 0 & 1.2176 & 0 & 0 & 0 & 0 \\ 1.2176 & 0 & 0.7902 & -0.7902 & 0.0536 & 0 \\ 0 & 0.7902 & -0.8387 & 0 & 0.7902 & 0 \\ 0 & -0.7902 & 0 & 0.8387 & 0.7902 & 0 \\ 0 & 0.0536 & 0.7902 & 0.7902 & 0 & 1.2176 \\ 0 & 0 & 0 & 0 & 1.2176 & 0 \end{bmatrix}$$

(a) (b)

Figure 3.14 Normalized coupling matrices corresponding to different topologies. (a) Simplified coupling matrix corresponding to topology in Fig. 3.1(a) after Chebyshev filtering function synthesis. (b) Rotated coupling matrix corresponding to topology in Fig. 3.2(b) with angle -0.7854 rad/s

Third, the mainline coupling M_{23} is rotated by applying (3.4) and (3.5) to the coupling matrix in Fig. 3.14(a). The non-zero coefficients distributed along the diagonal entries of the coupling matrix are shown in Fig. 3.14(b). Afterwards, to reconfigure the filtering characteristics, the previous internal coupling tuning is completely converted to resonant frequencies tuning.

3.5.2 Filter design

In this work, a 3D electromagnetic model of the filter is built in the ANSYS High-Frequency Structure Simulator (HFSS). The geometry is shown in Fig. 3.15 (Dimensions: w_1 = 900, l_1 = 520, w_2 = 1000, l_2 = 1000, w_3 = 100, w_4 = 165, w_5 = 250, w_6 = 150, w_7 = 170, R_1 = 100, w_{int} = 324, w_{ext} = 433, w_c = 350, h_1 = 400. Unit:mil). Resonators 1 and 4 are realized as the fundamental modes in two rectangular waveguide cavities, whereas resonators 2 and 3 are realized as dual modes in a large square waveguide cavity. The electric field distribution of the two diagonal modes is simulated by an eigenmode analysis in ANSYS HFSS and shown in Fig. 3.16. Each diagonal mode is equipped with a pair of tuning screws at the two magnitude peaks. The advantage of this filter is that all the internal and external coupling, no matter positive or negative, are realized through H-plane irises at the center of the wall. Tuning screws are provisioned in the cavity where the electric field is the most intensive to tune the resonant frequencies of the corresponding modes. The depth values of tuning screws for the fundamental mode, diagonal mode 1, and diagonal mode 2 in the cavity are defined as via_1, via_2, and via_3, respectively. The tuning screws in the middle of the irises can precisely control the coupling coefficients after fabrication, which are fixed after adjusting coefficients.

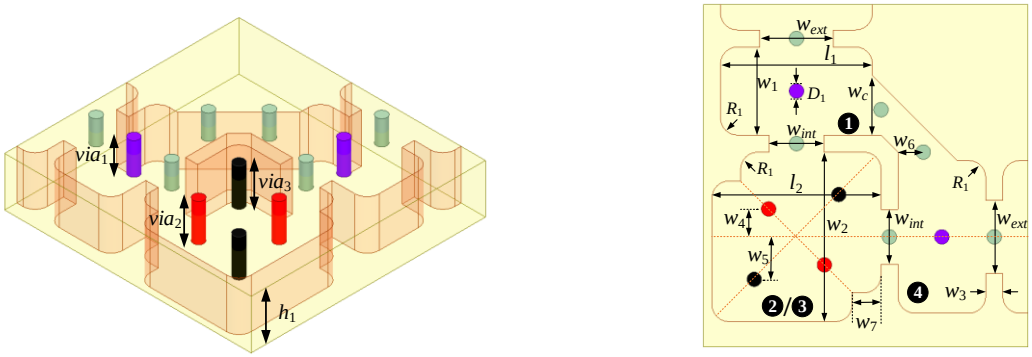

(a) (b)

Figure 3.15 3-D electromagnetic model of demonstrated bandpass filter. (a) Perspective view. (b) Top view

The internal coupling irises w_{int} should be deployed in the middle of the wall to consider the performance of each state. To achieve the same internal coupling coefficient for both diagonal modes, two diagonal corner cuts [109, 110] in the square cavity are introduced. The correspondence

between geometrical parameters and coupling matrix coefficients is summarized in Table 3.8. In the model, the fixed parameters are designed first. Then, the tuning parameters are swept to realize reconfigurable states and frequency-tuning performance.

The filter is tuned with the assistance of the synthesized coupling matrix and the help of the model-based vector fitting method [111-113]. The simulated and the synthesized coupling matrix responses are plotted together in Fig. 3.17. According to the synthesized coupling matrix, M_{22} = -0.8387 and M_{33} = 0.8387 realize a state with TZs on the imaginary axis of the complex plane, and M_{22} = 0.7840 and M_{33} = -0.7840 realize the other state with TZs on the real axis of the complex plane. In switching between the two kinds of filter states, all the other coupling coefficients are kept constant. During the simulation, we keep via_1 = 93.7 mil and only tune values via_2 = 176.4 mil, via_3 = 163.0 mil and via_2 = 170.5 mil, via_3 = 169.1 mil to switch from state1 to state2. It can be seen from Fig. 3.17(a) that the simulated results are consistent with synthesized coupling matrix states (State1: TZs on the real axis of the complex plane. State2: TZs on the imaginary axis of the complex plane). The group delay responses between the two states given in Fig. 3.17(b) have a similar enhancement compared to the simulated and synthesized results. Noted that the physical locations of TZs can be deployed closer to the passband by enhancing the coupling between resonator 1 and resonator 4 [103].

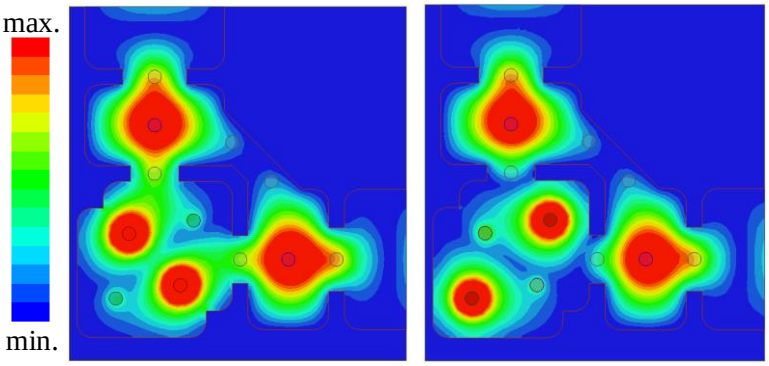

(a) (b)

Figure 3.16 Electric field distribution of two diagonal modes with via_1 = 93.7, via_2 = 170.5, via_3 = 169.1. Unit: mil. (a) Diagonal mode 1. (b) Diagonal mode 2

Table 3.8 Correspondence between geometrical parameters and coupling matrix coefficients

	Geometrical Parameters	Coupling Coefficients
Fixed parameters	l_1	M_{11}, M_{44}
	w_1	M_{11}, M_{44}
	l_2	M_{22}, M_{33}
	w_2	M_{22}, M_{33}
	w_c	M_{14}
	w_{ext}	M_{12}, M_{34}
	w_{int}	M_{12}, M_{13}, M_{24}, M_{34}, M_{14}
	w_7	M_{22}, M_{33}
Tuning parameters	via_1	M_{11}, M_{44}
	via_2	M_{22}
	via_3	M_{33}

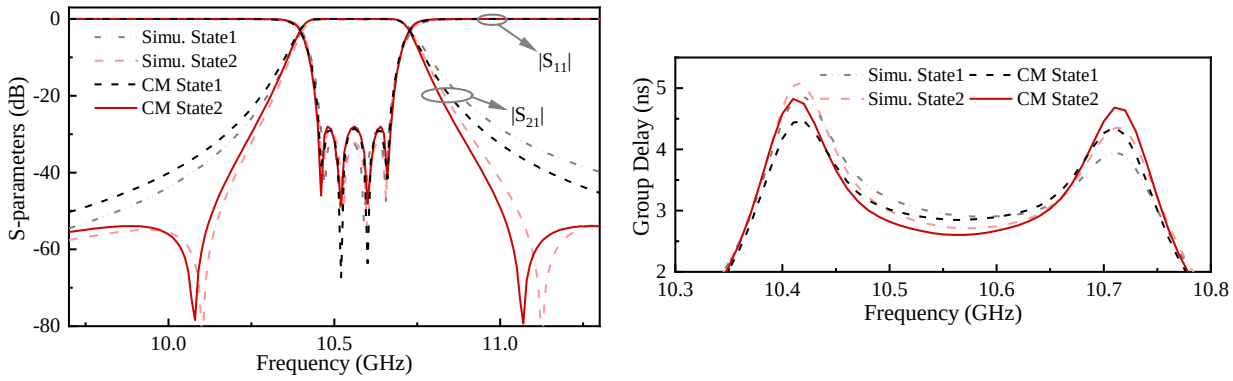

(a) (b)

Figure 3.17 Comparison of states between synthesized coupling matrix and simulated electromagnetic model. (a) S-parameters. (b) Group delay

Tuning screws via_1, via_2, and via_3 can be used to achieve the tunable performance of this filter. The simulated results of the filter are shown in Fig. 3.18 and the corresponding values of via_1, via_2, and via_3 at different center frequencies as well as states are given in Table 3.9. It can be observed that at the same center frequency, the value of via_1 is the same and the states can be switched by

changing the values of via_2 and via_3. The frequency-tuning performance of both states can be realized by adjusting the values of via_1, via_2, and via_3 together. Both states have a tuning frequency range from 9.5 GHz to 10.6 GHz. The performance becomes worsen when the resonant frequencies shift far away from the designed center frequency because all the physical coupling irises are fixed, which are set to introduce a mismatch in this scenario. In Fig. 3.18, there are small peaks on the upper stopband whose magnitude is lower than -28 dB (State1: TZs on the real axis of the complex plane. State2: TZs on the imaginary axis of the complex plane). They result from the spurious resonant modes excited by the tuning screws.

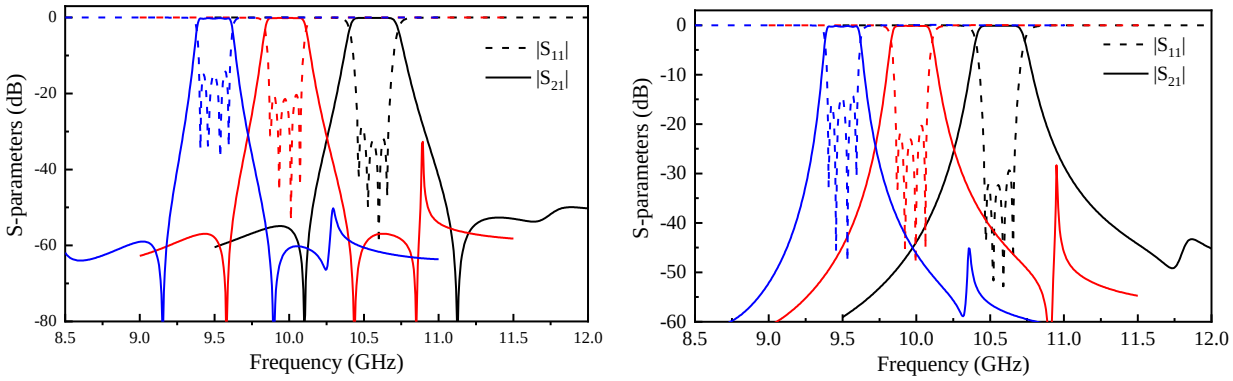

(a) (b)

Figure 3.18 Simulated S-parameters responses of the prototyped tunable bandpass filter. (a) Tunable responses of State2. (b) Tunable responses of State1

Table 3.9 The corresponding values of via_1, via_2, and via_3 at different center frequencies as well as states in figure 3.18

State	f_o (GHz)	via_1 (mil)	via_2 (mil)	via_3 (mil)
state1	10.56	93.7	176.4	163.0
	9.97	138.7	195.1	184.1
	9.50	164.7	210.8	201.1
state2	10.56	93.7	170.5	169.1
	9.97	138.7	190.1	189.2
	9.49	164.7	206.2	205.6

3.5.3 Fabrication and measurement

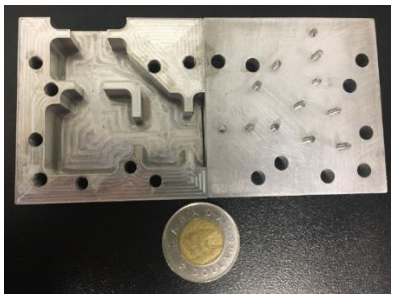

Figure 3.19 Photograph of the fabricated prototype

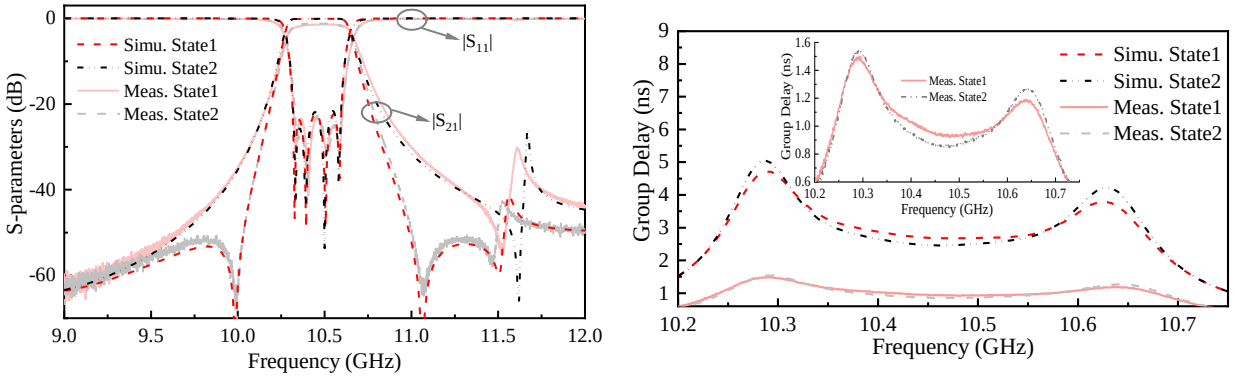

(a) (b)

Figure 3.20 Measured responses of the fabricated filter. (a) S-parameters of both states. (b) Measured group delay responses

The photograph of the fabricated tunable bandpass filter is shown in Fig. 3.19. The filter is made of a piece of aluminium 6061-T5. All the tuning screws are accessible on the top cover. It is measured with a vector network analyzer Keysight N5224A. The measurement results are shown in Fig. 3.20 (State1: TZs on the real axis of the complex plane. State2: TZs on the imaginary axis of the complex plane). The measured bandwidth, insertion loss (IL), and return loss (RL) of the state with TZs on the imaginary axis of the complex plane are 290 MHz, 1.2 dB, and 22.9 dB, respectively, when the filter is tuned to the center frequency of 10.46 GHz. Then, the resonant frequencies of the dual modes can be tuned by changing values of via_2 and via_3. The response is reconfigured to the other state with TZs on the real axis of the complex plane operating at the same band. The IL and RL are 1.5 dB and

23.3 dB, respectively. The peaks beyond the passband in Fig. 3.20(a) results from the interference modes excited by tuning screws in both states. The group delay curves of these two different states are given in Fig. 3.20(b), confirming that the TZs on the real axis of the complex plane are beneficial for achieving a better group delay response.

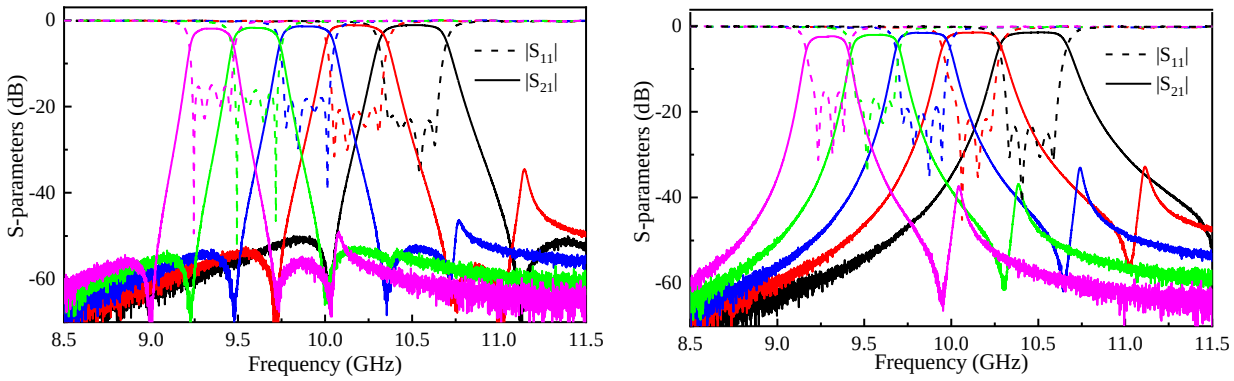

(a) (b)

Figure 3.21 Measured S-parameters responses of the tunable bandpass filter. (a) Tunable responses of State2. (b) Tunable responses of State1

Table 3.10 Comparisons with other related state-of-the-art designs

Ref.	Type	f_0 (GHz)	FBW@ f_0 (%)	F-T Range (GHz)	F-T Pct. (%)	Order	No. of TZ	Switchable TZ
[73]	WG	11.5	0.43	11.29-11.68	3.40	4	2	No
[35]	WG	17.37	0.21	17.15-17.59	2.53	4	2	No
[114]	ML	1.19	9.50	0.94-1.44	42.02	2	2	No
[115]	ML	1.22	9.60	0.95-1.48	43.44	4	2	No
[55]	SIW	2.17	3.69	2.00-2.35	16.13	3	2	No
[53]	SIW	2.50	7.20	-	-	4	2	Yes
Ours	WG	9.95	2.91	9.40-10.50	11.06	4	2	Yes

ML: Microstrip Line; SIW: Substrate Integrated Waveguide; WG: Waveguide; FBW: Fractional Bandwidth; F-T: Frequency Tuning; Pct.: Percentage. Ref.: Reference. No. of TZ: Number of TZ.

The tunable performances of both states are measured and shown in Fig. 3.21(State1: TZs on the real axis of the complex plane. State2: TZs on the imaginary axis of the complex plane). The deeper

the turning screws are in the cavities, the lower the operating frequency is. The measured tuning ranges of both states are from 9.4 GHz to 10.5 GHz with the insertion loss ranging from 1.2 dB to 2.5 dB. Table 3.10 provides the comparisons of our work with some other related designs. It can be seen that the tunable performance and reconfigurable filter states (at the same operating frequency) can be realized simultaneously with the same physical structure.

3.6 Conclusion

In this chapter, the synthesis method for tunable filters with reconfigurable symmetric TZs on the real or imaginary axis of the complex plane has been proposed. The reconfigurable TZs can be realized together with the center frequency control by merely tuning the resonant frequencies of the cavities. The synthesis procedure of these tunable filters for different orders with a variety of coupling diagrams is theoretically interpreted by coupling matrix rotations. The theoretical guidance on reconfiguring symmetric TZs on the complex plane is highlighted because it cannot be directly synthesized through an existing coupling matrix method. Afterwards, the optimization steps for the coupling matrix are given, which make a trade-off among all states' performances of the filter, as demonstrated using a synthesized eighth-order filter. For experimental verification, a fourth-order tunable bandpass filter prototype with a pair of symmetric TZs has been designed, fabricated, and measured. The responses of the fabricated filter can be switched between two states, which has validated the proposed synthesis and design method of the tunable filters. Moreover, this approach can provide a foundation for guiding a flexible design of multi-band and bandstop reconfigurable filters in the future.

CHAPTER 4 TUNABLE BANDPASS FILTER WITH RECONFIGURABLE ASYMMETRIC TRANSMISSION ZEROS

This chapter introduces and discusses two approaches to the development of tunable bandpass filters with reconfigurable asymmetric transmission zeros (TZs), including an inline tunable bandpass filter with TZs realized by frequency-dependent coupling (FDC), and a tunable bandpass filter with one switchable TZ by only tuning resonances.

Inline tunable bandpass filter with TZs realized by FDC: an inline tunable bandpass filter with asymmetric TZs using FDCs is presented. To the best of our knowledge, this is the first time using the FDC technique to realize inline tunable bandpass filters owning asymmetric TZs that can be reconfigured at the lower or upper side of the passband. Compared to cross-coupling based topologies to control asymmetric TZs, the inline topology using FDCs simplifies the signal flow path, which brings less impact on the other coupling coefficients when reconfiguring the locations of TZs and is easier for physical fabrication.

The synthesis procedure can be explained by coupling matrix rotations, and the initially transversal coupling matrix is eventually transferred to the purposed matrix exhibiting an inline topology. Reversing the signs of all diagonal coefficients in the constant matric M and mainline coefficients in the capacitance matrix C together, the positions of TZs can be symmetrically switched to the other side of the passband and the response maintains the same return loss level. Physically tuning the elements for the resonant frequencies and FDCs, the functions of operating frequencies tuning and locations of TZs controlling can be obtained simultaneously.

For experimental verification, a fourth-order inline tunable bandpass filter with two asymmetric TZs has been synthesized, designed, fabricated, and measured. It has two reconfigurable states where both TZs are at the upper or lower side of the passband. For both types of states, the measured results verify that the center frequency of the filter can be tuned from 14.0 GHz to 14.9 GHz with the insertion loss (IL) variation from 1.1 dB to 1.8 dB.

Tunable bandpass filter with one switchable TZ by only tuning resonances: A methodology for tunable bandpass filters (tBPFs) with one switchable transmission zero (TZ) is presented, wherein the frequency tuning and TZ switching can be simultaneously achieved by merely tuning the resonant frequencies of resonators. Theoretically interpreted by coupling matrices with

arbitrary filtering orders (n $\geqslant$ 2), the TZ can be symmetrically switched between the lower and upper sides of the passband while retaining the same return loss level.

As a demonstration, a fourth-order waveguide tBPF is synthesized, designed, fabricated, and measured for experimental verification. Two responses, namely TZ on the lower and upper sides, are showing the tunable frequency range from 9.5 GHz to 10.8 GHz with insertion loss (IL) from 0.34 dB to 1.40 dB and 3-dB bandwidth from 230 MHz to 370 MHz, respectively, which verifies the proposed methodology very well.

4.1 Inline tunable bandpass filter with TZs realized by FDC

4.1.1 Introduction

The content of this section is from our paper named *inline tunable bandpass filter with switchable asymmetric transmission zeros realized by frequency-dependent coupling*. Tunable bandpass filters are crucial in modern communication systems to select the desired band of frequencies for transmission and/or reception. Thereinto, the frequency-tuning characteristic of tunable filters is conveniently used to relocate channels needed for replacing lots of microwave filtering units, thereby saving operating costs. Deploying finite-position TZs near the band is considered to improve the near-skirt selectivity. These TZs are required to reconfigure at the lower or upper sides of the passband because different channels may need diverse responses. Generally, there are three approaches to generate finite TZs, namely, extracted-pole sections [93, 94, 116], cross-coupling scenarios between nonadjacent nodes [74, 77], and frequency-dependent couplings (FDCs) [76, 95, 96, 117, 118].

Extracted-pole sections are well-known to generate TZs by dangling resonators [94, 119]. The topology, consisting of a dangling resonator and a non-resonating node [120], can independently control one TZ on the imaginary axis of the complex plane. It can be synthesized by a circuit-based method [93, 121, 122], and described by a coupling matrix. The filter design has merits containing flexible layout, low loss, and suitably applying for high power handling scenarios. However, there are seldom researched works focused on tunable filter design. The reason is mainly concerned with two parts. First, the filter needs additional tuning elements for non-resonating nodes, which increases tuning units for the tunable filter control. Second, it is a daunting challenge to physically

tune the non-resonating node over a very wide dynamic tuning range to reconfigure the locations of TZs even though the aspect of a matrix shows such a possibility.

Cross-coupling scenarios between non-adjacent nodes are one of the most prevalent ways to generate TZs on the imaginary axis [74, 91]. Multipath signal flow paths are constructed and relative phase shifts of them are set to control the locations of TZs in a tri-section or quadruplet topology [74, 123]. For example, in the tri-section topology, the TZ is realized on the upper side of the passband if the cross-coupling is positive and vice versa [108]. To switch the locations of TZs, the cross-coupling or inter-resonator coupling coefficient should reverse the sign, which needs a more complicated physical structure design for the coefficient control. At the same time, due to the multipath topology, some nodes inevitably have more than two coupling paths, which make networks sensitive to match. There are two more potential problems with tunable filter design. First, since the coefficient controls the position of TZ, no matter mainline coupling or cross-coupling needs altering the sign to reconfigure responses, the previous matching network of nodes having more than two paths must be affected. It is more difficult to match the physical coupling networks after the coupling coefficient reverses the sign. Second, the dynamic range of the coefficient reversing the sign should cover the needed tuning range for tunable filter reconfiguration. The linearity and parasitic resistance of tuning elements should also be considered because of complex internal coupling circuits.

Frequency-dependent coupling technique is attractive for overcoming the potential drawbacks mentioned above for tunable filter design. It is also called resonating coupling [119, 124], or mixed electrical and magnetic coupling [75, 125], or dispersive coupling [126]. In this case, an intrinsic coupling structure brings flexibility to control the location of TZs. The inline topology is used to simplify the required multipath signal flows, which makes it robust to match networks because each node has up to two signal flows. According to its outstanding characteristics, numerous topics based on FDCs for filters [76, 124, 125] and diplexers [127] have extensively been studied in recent years. To the best of our knowledge, however, a tunable filter design using FDCs has hardly been investigated.

In this work, the synthesis of inline tunable bandpass filters with asymmetric TZs using FDCs is proposed. The asymmetric TZs can be reconfigured at the lower or upper side of the passband while the response maintains the same return loss level. The final matrix can be synthesized and transformed from the initial transversal coupling matrix. The features of operating frequency tuning

and locations of TZs controlling are implemented by tuning the elements of resonant frequencies and FDCs together.

The subsequent sections are organized as follows. The synthesis procedure of how to achieve the purposed matrix and the mechanism of how to reconfigure the positions of TZs are investigated in detail in Section 4.1.2. A fourth-order waveguide inline tunable bandpass filter is demonstrated in Section 4.1.3. Thereinto, the FDCs are realized by partial height conducting posts [128]. In Section 4.1.4, the filter is fabricated and measured to verify the synthesis procedure and the performance of the inline tunable bandpass filter. Finally, the concluding remarks are drawn in Section 4.1.5.

4.1.2 Synthesis of an inline tunable bandpass filter

In this section, the synthesis procedure for inline tunable bandpass filters with TZs on the imaginary axis is discussed. The synthesis procedure of how to obtain the purposed matrices is interpreted by coupling matrix rotations. Detailed steps of the procedure to construct the matrix are illustrated starting from controlling one TZ in a tri-section topology. Subsequently, the mechanism of how to reconfigure the positions of TZs is explained from the aspect of the coupling matrix. Each TZ can be independently controlled in the inline topology.

Repeating similar steps of the procedure can be implemented to rotate the matrix that has more TZs. Eventually, the inline topology is realized, which is transformed from the initial cascaded tri-section topology.

4.1.2.1 Topology controlling one TZ

The filter to control one TZ using FDC is analyzed starting from order two. There are two existing methods to synthesize the topology according to design requirements, including directly using a circuit-based method or coupling matrix rotations [97, 98]. For the second approach, note that the initially synthesized matrix of a transversal topology first rotates to an arrow topology [98], and then transfers to a tri-section topology. The final tri-section topology controlling one TZ is shown in Fig. 4.1(a), where numbered black nodes represent resonators and solid lines represent constant couplings. The grey nodes named ‘X’ and ‘Y’ are terminals, source and load because the filter order is two here. Note that each grey node can also represent a resonator to increase the filter order while the number of controlled TZs is still one.

The next step is eliminating the mainline coupling $M_{12}^{(1)}$ using coupling matrix rotations with a rotation angle θ_{r1}.

$$\theta_{r1} = \frac{1}{2}\tan^{-1}\left(\frac{2M_{12}^{(1)}}{M_{22}^{(1)} - M_{11}^{(1)}}\right). \tag{4.1}$$

$$M^{(2)} = R \cdot M^{(1)} \cdot R^{T}. \tag{4.2}$$

where $M_{11}^{(1)}$, $M_{12}^{(1)}$ and $M_{22}^{(1)}$ are coupling coefficients in constant coupling matrix $M^{(1)}$ corresponding to the topology in Fig. 4.1(a). $M^{(2)}$ is the rotated matrix from $M^{(1)}$. R^{T} is the transpose of R. In R, all the diagonal entries are 1 and off-diagonal entries are 0, except for $R_{11} = R_{22} = cos\theta_{r1}$ and $R_{21} = -R_{12} = sin\theta_{r1}$.

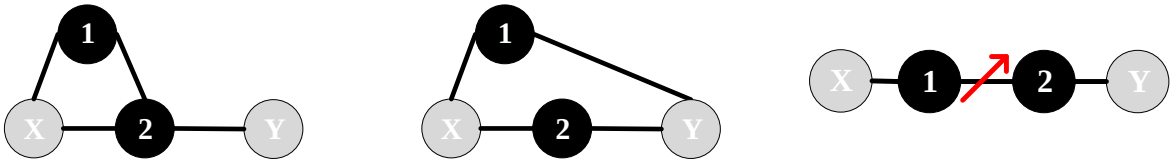

(a) (b) (c)

Figure 4.1 Transforming a tri-section topology to an inline frequency-dependent coupling (FDC) topology. (a) Tri-section topology. (b) Box section topology. (c) Inline frequency-dependent coupling topology

As shown in Fig. 4.1(b), the previous mainline coupling $M_{12}^{(1)}$ is eliminated and a new coupling coefficient $M_{1Y}^{(2)}$ is generated. Note that the diagonal entries of the capacitance matrix $C^{(2)}$ corresponding to $M^{(2)}$ in Fig. 4.1(b) are all scaled to unity, which has the same values as $C^{(1)}$ in Fig. 4.1(a) (Numbered black nodes: resonators. Grey nodes named 'X' and 'Y': resonators or terminals. Black solid lines: constant couplings. The black solid line crossed by a red arrow: FDC).

In the third step, the row and column of the matrices $M^{(2)}$ and $C^{(2)}$ corresponding to node 2 are multiplying with constant α which is calculated as shown below

$$\alpha = \sqrt{-\frac{M_{1Y}^{(2)} M_{1X}^{(2)}}{M_{2Y}^{(2)} M_{2X}^{(2)}}}\,. \tag{4.3}$$

It is prepared to eliminate coefficients $M_{1Y}^{(2)}$ and $M_{2X}^{(2)}$ simultaneously in the fourth step. The coupling matrix is rotated in (4.2) again with a rotation angle θ_{r2} in $M^{(2)}$ and $C^{(2)}$. The expression of θ_{r2} is given below

$$\theta_{r2} = \tan^{-1}\left(\frac{M_{2X}^{(2)}}{M_{1X}^{(2)}}\right). \tag{4.4}$$

Afterward, the constant coupling matrix and the capacitance matrix are updated to $M^{(3)}$ and $C^{(3)}$ corresponding to the topology shown in Fig. 4.1(c). The previous tri-section topology in Fig. 4.1(a) is eventually rotated to the inline topology. Besides, an FDC coefficient is introduced, which is denoted by a black solid line crossed by a red arrow.

The last step is to scale matrix $C^{(3)}$ at node 1 and node 2 to unity [108]. The row and column of both matrices, $M^{(3)}$ and $C^{(3)}$, corresponding to node 1 and node 2 are divided by $\sqrt{C_1^{(3)}}$ and $\sqrt{C_2^{(3)}}$, respectively. The normalized $M^{(3)}$ and $C^{(3)}$ are derived below

$$M^{(3)} = \begin{bmatrix} 0 & M_{S1} & 0 & 0 \\ M_{S1} & M_{11} & M_{12} & 0 \\ 0 & M_{12} & M_{22} & M_{2L} \\ 0 & 0 & M_{2L} & 0 \end{bmatrix}. \tag{4.5}$$

$$C^{(3)} = \begin{bmatrix} 0 & 0 & 0 & 0 \\ 0 & 1 & C_{12} & 0 \\ 0 & C_{12} & 1 & 0 \\ 0 & 0 & 0 & 0 \end{bmatrix}. \tag{4.6}$$

where all the coefficients in the constant coupling matrix $M^{(3)}$ have a one-to-one correspondence with the topology in Fig. 4.1(c). The diagonal entries of capacitance matrix $C^{(3)}$ are scaled to unity and the coefficient C_{12} can be regarded as a partial FDC coefficient which is equal to $M_{12}+sC_{12}/\mathrm{j}$.

The location of TZ in Fig. 4.1(c) should satisfy the condition whereby the equation of S_{21} is equal to 0 [108]. Substituting (4.5) and (4.6) into it, the equation is derived below.

$$S_{21} = sC_{12} + jM_{12} = 0$$
$$s = \frac{-jM_{12}}{C_{12}} \quad . \tag{4.7}$$

It can be seen from (4.7) that the location of TZ is only associated to the FDC coefficient and is not affected by any resonators. The position of TZ can be switched by reversing the sign of M_{12} or C_{12}. Since C_{12} is dependent on operating frequencies, it is chosen to reconfigure the TZ in this work.

4.1.2.2 Topology controlling more TZs

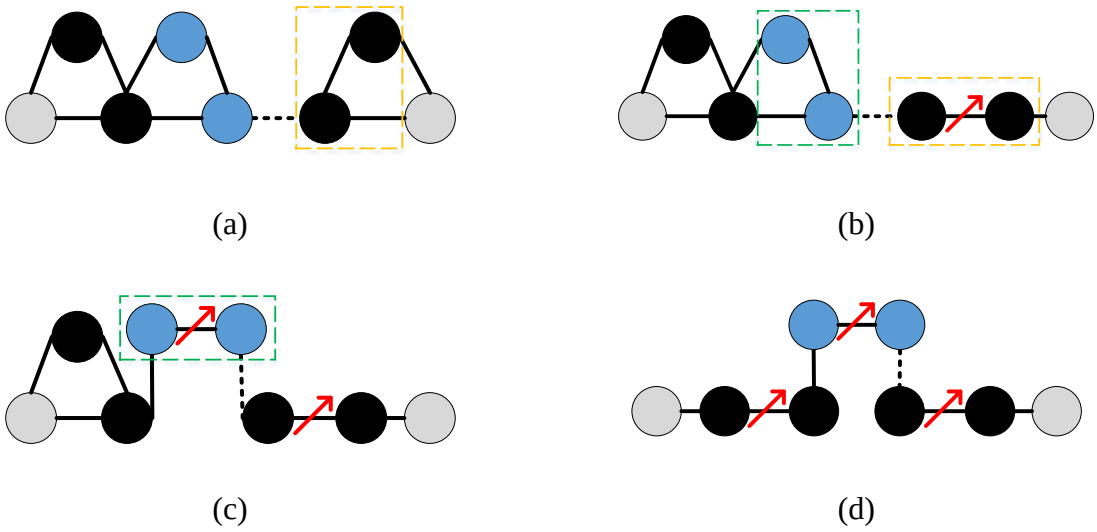

Figure 4.2 Synthesis procedure for inline tunable bandpass filters with TZs. (a) Topology with multiple tri-sections. (b) Transforming the tri-section topology to the FDC topology in the orange frame by the mirror-symmetric topology in Fig. 4.1(a). (c) Transforming the tri-section topology to the FDC topology in the green frame by the same topology in Fig. 4.1(a). (d) Final inline topology with multiple FDCs

The coupling matrix rotations of the topology controlling one TZ can be regarded as a sub-topology to extend the matrix having more TZs. This extension is under the condition that the filter order N should be no less than two times the number of TZs [96]

$$N \geq 2N_{TZ} . \tag{4.8}$$

where N and N_{TZ} are the filter order and the number of TZs, respectively. The topology controlling more TZs is shown in Fig. 4.2(a) with multiple cascaded tri-sections. The black and blue nodes indicate resonators. The black dashed line means many pairs of blue nodes. The transformation starts from the pair of black nodes in the orange frame on the right side. The rotating steps are the same as (4.1) to (4.4) by the mirror-symmetric topology in Fig. 4.1(a). The grey node named 'Y' is a resonator. The grey node named 'X' is a terminal or resonator. The transformed topology is given in Fig. 4.2(b) (Black or blue nodes: resonators. Grey nodes: resonators or terminals. Black solid lines: constant couplings. Black dashed line: many pairs of blue nodes in the green frame. Black solid lines crossed by a red arrow: FDCs). The previous sub-topology is transformed into an inline sub-topology with one FDC.

Repeating the same steps in (4.1) to (4.4) as for the topology in Fig. 4.1(a), the pair of blue nodes in the green frame can be rotated to an inline sub-topology with one FDC as shown in Fig. 4.2(c). Noted that each additional TZ requires an additional pair of blue nodes if the total number of TZs is more than two.

At last, the final inline topology with FDCs is acquired, as shown in Fig. 4.2(d), after transforming the last two back nodes on the left side. The corresponding matrices M and C are normalized by scaling diagonal entries of C to unity corresponding to each node. It is worth pointing out that this procedure is also suitable if more resonators cascade in the topology ($N > 2N_{TZ}$) because this would not affect the rotating procedure. In other words, at least two resonators between two FDCs in the final inline topology under the condition in (4.8). Since each location of TZ is only dependent on the corresponding FDC, the locations of TZs are controlled independently.

In conclusion, if only one TZ is controlled, the synthesized tri-section topology is the same as that shown in Fig. 4.1(a). If two TZs are controlled, the synthesized topology with multiple tri-sections is shown in Fig. 4.2(a) without blue nodes. If more than two TZs are controlled, the topology is the same as shown in Fig. 4.2(a). Afterward, by repeating the rotating steps from (4.1) to (4.4), the final inline topology can be achieved. At last, the corresponding constant coupling matrix M and capacitance matrix C are normalized.

4.1.3 Experimental validation

A fourth-order tunable bandpass filter is designed with the following specifications: an in-band RL of 20 dB, a center frequency of 14.45 GHz with a bandwidth of 300 MHz, and two TZs initially located at -1.7j and -3.3j, which can be switched to +1.7j and +3.3j.

4.1.3.1 Synthesis of matrices M and C

According to the initial locations of TZs and the RL level, the transfer and reflection characteristics can be synthesized from the generalized Chebyshev filtering function [14]. After implementing coupling matrix rotations [76, 129], the final normalized constant coupling matrix M and capacitance matrix C are obtained as follows:

$$M = \begin{bmatrix} 0 & 0.8585 & 0 & 0 & 0 & 0 \\ 0.8585 & \pm 0.8679 & 0.9572 & 0 & 0 & 0 \\ 0 & 0.9572 & \pm 0.4848 & 0.5922 & 0 & 0 \\ 0 & 0 & 0.5922 & \pm 0.1609 & 0.9140 & 0 \\ 0 & 0 & 0 & 0.9140 & \pm 0.4176 & 0.9983 \\ 0 & 0 & 0 & 0 & 0.9983 & 0 \end{bmatrix}, \tag{4.9}$$

$$C = \begin{bmatrix} 0 & 0 & 0 & 0 & 0 & 0 \\ 0 & 1 & \pm 0.5632 & 0 & 0 & 0 \\ 0 & \pm 0.5632 & 1 & 0 & 0 & 0 \\ 0 & 0 & 0 & 1 & \pm 0.2770 & 0 \\ 0 & 0 & 0 & \pm 0.2770 & 1 & 0 \\ 0 & 0 & 0 & 0 & 0 & 0 \end{bmatrix}, \tag{4.10}$$

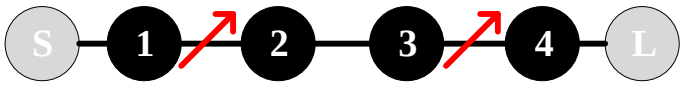

Figure 4.3 Inline frequency-dependent coupling topology for a fourth-order bandpass filter

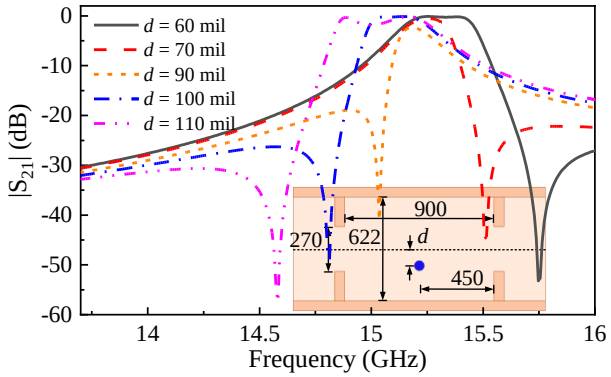

(a)

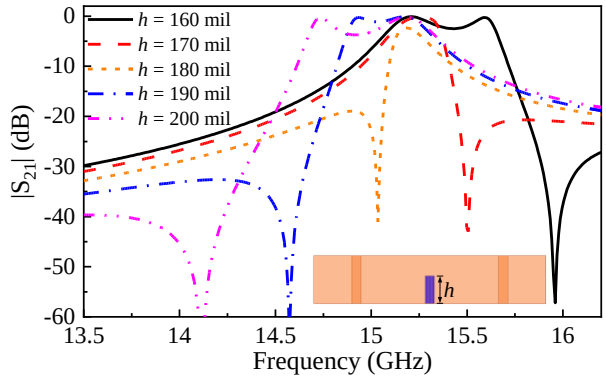

(b)

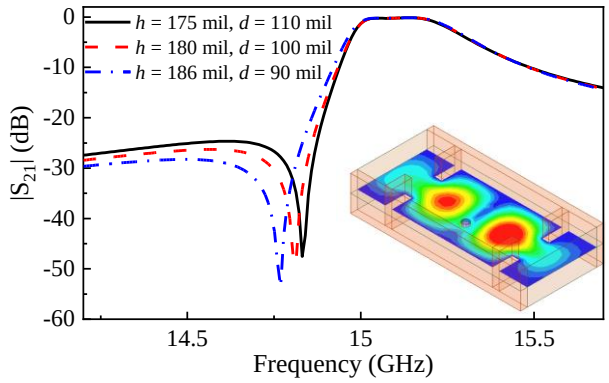

(c)

Figure 4.4 Physical realization of FDC. (a) S-parameters responses by moving the partial height post close to the sidewall. *h* = 180 mil. (b) S-parameters responses by tuning the depth of the partial height post. *d* = 90 mil. (c) S-parameters responses of controlling the locations of TZs by moving and tuning the partial height post simultaneously. Unit: mil

It can be observed that if the diagonal entries of *M* and off-diagonal entries of *C* (in blue color) are positive, the TZs will be located at -1.7j and -3.3j. If the signs of these coefficients get reversed, the two TZs will be switched to +1.7j and +3.3j, respectively. The corresponding inline topology is depicted in Fig. 4.3, where each resonator only has two associated couplings (Numbered black nodes: resonators. Grey nodes named 'S' and 'L': source and load. Black solid lines: constant couplings. The black solid line crossed by a red arrow: FDC). The location of each TZ is independently controlled by adjacent resonators and corresponding FDC.

4.1.3.2 Physical realization of FDC structures

The physical realization of the frequency-dependent coupling structures is primarily concerned because it determines the location of TZ. The electromagnetic model of a second-order bandpass filter with one FDC is simulated in ANSYS HFSS. The perspective view of the filter corresponding to the topology in Fig. 4.1(c) is given as an inset in Fig. 4.4(c). The FDC is realized as a partial height post which is deployed on the vertical centerline of the cavity. Two resonators operating with the fundamental mode TE_{110} are frequency-dependent, coupled by the post. Note that the diameter of the tuning post would affect the strength of FDC as well as the sensitivity during tuning. The latter would be given priority so as to directly choose the post diameter of 60 mil.

The position and the depth of the partial height post are investigated in detail to realize the expected response. The distance from the horizontal centerline of the cavity to the partial height post is defined by *d*, as shown in the inset in Fig. 4.4(a). The height of the post in the cavity is defined by *h*, as shown in the inset in Fig. 4.4(b). Maintaining h = 180 mil, the location of TZ shifts from the upper side to the lower side of the passband if the post moves close to the sidewall (by increasing *d*), as shown in Fig. 4.4(a). At the same time, the internal coupling strength is first decreased and then increased. Afterward, maintaining d = 90 mil, the location of TZ is shifting from the upper side to the lower side of the passband if *h* is increasing, as shown in Fig. 4.4(b). The internal coupling strength changing has a similar trend compared to responses in Fig. 4.4(a).

Both *d* and *h* can be modified to flexibly control the location of TZ and the strength of internal coupling simultaneously with a large dynamic range. Sweeping *d* and *h* together, it can be observed that the location of TZ can be controlled while the internal coupling strength is kept unchanged. As shown in Fig. 4.4(c), when the post is close to the sidewall with a smaller *h*, the location of TZ

is close to the passband and the bandwidth is constant. Since *d* must be fixed in the design and *h* can be tuned, the initial *d* mainly determines the location of TZ with a suitable value of *h*. According to the responses in Fig. 4.4(b), the location of TZ can be switched to the upper side of the passband by tuning the height of the post.

In conclusion, tuning sensitivity is the primary concern in choosing the diameter of the post. The initial position of the post mainly determines the location of TZ. The closer the post is to the sidewall (by increasing *d*), the closer the TZ is to the passband with a suitable value of *h*. At last, tuning the height of the post, *h*, can control the location of TZ and the coupling strength simultaneously.

4.1.3.3 Inline tunable bandpass filter design using FDCs

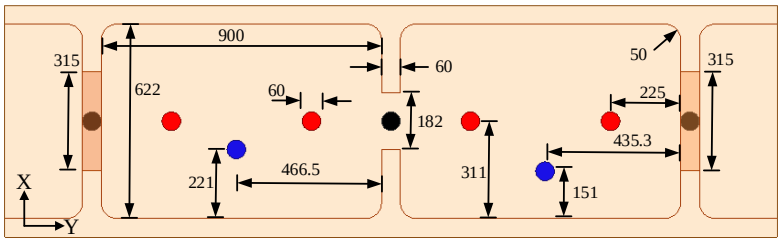

(a)

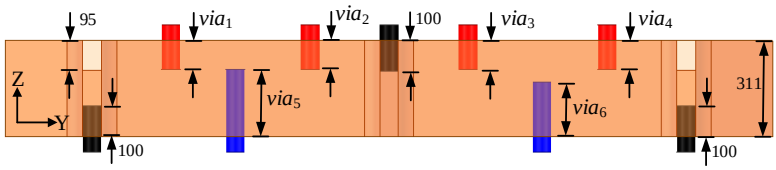

(b)

Figure 4.5 Electromagnetic model of the inline tunable bandpass filter with FDCs. (a) Top view. (b) Side view. Unit: mil

The synthesis of normalized matrices *M* and *C* are given in (4.9) and (4.10), respectively. The details of how to transform the normalized lowpass filter response to the bandpass filter response

with required specifications are introduced in [76]. The electromagnetic model of the fourth-order inline tunable bandpass filter with two FDCs is simulated in ANSYS HFSS, as shown in Fig. 4.5. The physical structure is cascaded by two cavities. Each cavity consists of two resonators and one FDC between them. Four partial height posts in red on the top side of the cavity are deployed to tune the resonant frequencies of fundamental modes TE_{110} and two posts in blue colors on the bottom side of the cavity are FDCs, as shown in Fig. 4.5(a). Based on the initial values of TZs, the positions of blue posts are adjusted along the vertical centerline of the cavity up and down to match the locations of TZs. The left and right blue post is corresponding to the TZs at -3.3j and -1.7j, respectively. After optimization, the final positions of them are moved a little bit on the left or right side to achieve better responses.

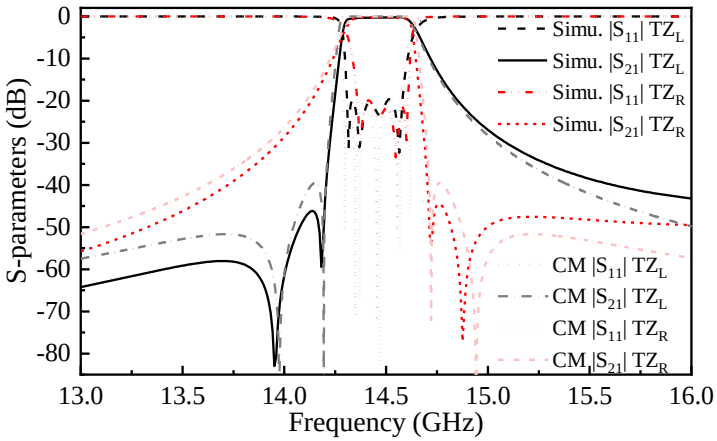

Figure 4.6 Simulated responses compared to coupling matrix responses

As shown in Fig. 4.5(b), a constant internal coupling is realized by an inductive iris. The external couplings are realized by partial height inductive irises after optimization. This is because the height of red posts would affect external coupling strength during resonant frequency tuning. The black posts are set to adjust the coupling coefficient after fabrication. The heights of the four red posts from left to right are defined by via_1, via_2, via_3, and via_4. The heights of left and right blue posts are defined by via_5 and via_6.

The filter is designed according to the synthesized matrices given in (4.9) and (4.10) and with the help of a model-based vector fitting method [111-113]. By the model-based vector fitting method, a coupling matrix corresponding to the same topology can be extracted from the simulation results.

Comparing each coefficient in the extracted matrix to the target matrix, the coefficient having the maximum error can be found. The adjustment is starting from the coefficient mapping to the corresponding physical structure. Subsequently, updated simulated curves can be extracted again. Repeating the same steps until the difference between two matrices is small enough. At last, the physical dimensions are optimized, and the results are marked in Fig. 4.5 except for these six variables. According to the aforementioned analysis in Section 4.1.2, controlling these six variables can realize center frequency tuning and TZ reconfiguration simultaneously.

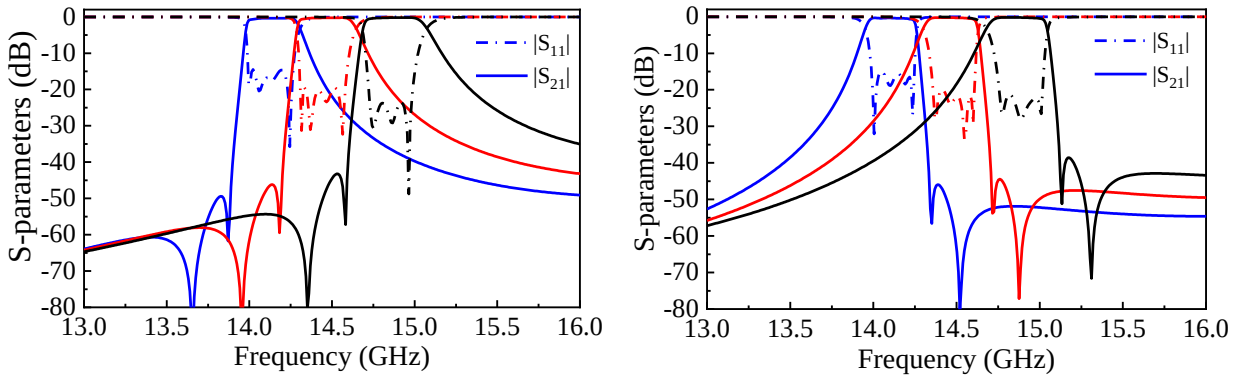

Figure 4.7 Simulated tunable responses of the inline bandpass filter. (a) TZs on the left sideband. (b) TZs on the right sideband

The response with two TZs on the left side of the passband is first simulated. Then, tuning these six variables and fixing all other physical dimensions, the simulated response with two TZs on the right side of the passband can be achieved, as shown in Fig. 4.6 (The response can be reconfigured by tuning the resonant frequencies and FDCs, simultaneously. Simulated results of TZs on the left side: via_1 = 79.5 mil, via_2 = 81.0 mil, via_3 = 81.0 mil, via_4 = 78.5 mil, via_5 = 208.9 mil, via_6 = 171.5 mil. Simulated results of TZs on the right side: via_1 = 85.7 mil, via_2 = 87.8 mil, via_3 = 89.5 mil, via_4 = 80.3 mil, via_5 = 188.5 mil, via_6 = 162.3 mil). Both responses have the same performance, including RL of 20 dB, center frequency of 14.38 GHz, and 3-dB bandwidth of 300 MHz. The simulated responses are well consistent with the coupling matrix-based responses except for an

offsetting of locations of TZs on the right sideband. This is caused by the height of FDC posts. The shorter the height of posts, the locations of TZs closer to the passband, and even the impact is mild.

The frequency tuning performance is described in Fig. 4.7 by tuning these six variables together. The tunable responses with TZs on the left and right sides are depicted in Fig. 4.7(a) and Fig. 4.7(b), respectively. Tuning the operating band to the lower or upper side of the initial passband brings under and over coupled, respectively. Since the constant internal coupling and external couplings are fixed in the design, the tuning manipulation introduces a mismatch between required and achieved coupling strengths so as to deteriorate the response performance. It is a trade-off between the response performance and the needed number of tuning elements because internal/external couplings control can modify the response performance but need more controlled tuning elements. It can be seen that the out-of-band rejection of TZs' sideband becomes better if the TZs are located at lower frequencies. The lower frequencies of TZs located are, the higher height of FDC posts needed are. However, a higher height of the FDC post would mildly take the locations of TZs away from the passband, which is the same reason explained for the responses in Fig. 4.6. In short, the locations of TZs can be switched with the guidance of the synthesis procedure. The tuning performance, no matter the TZs located on the lower or upper side of the passband, is validated by tuning these six screws.

4.1.4 Fabrication and measurement

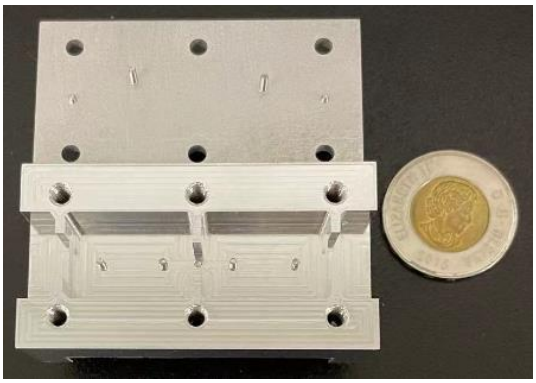

Figure 4.8 Photograph of the fabricated inline tunable bandpass filter

The photograph of the fabricated inline tunable bandpass filter is shown in Fig. 4.8. The filter is made of a piece of aluminum 6061-T5. All the tuning posts are realized by tuning screws. The

diameter of the screws is 60 mil. It is measured with WR-62 connectors and vector network analyzer N5224A. The measured responses are depicted in Fig. 4.9. As can be seen, both types of responses, TZs at the lower and upper sides of the passband, measured 3-dB bandwidth, insertion loss (IL), and RL is 300 MHz, 1.4 dB, and 20.7 dB, respectively, when the filter is tuned to the center frequency at 14.38 GHz. The performance of IL can be modified with silver plating both in cavities and screws.

The tunable performance of responses, TZs on the lower and upper side of the passband, is measured in Fig. 4.10(a) and Fig. 4.10(b), respectively. The responses have the frequency tuning range from 14.0 GHz to 14.9 GHz with insertion losses from 1.1 dB to 1.8 dB. The measured tuning responses are consistent well with the simulated tuning responses as shown in Fig. 4.7, no matter the frequency tuning performance or the locations of TZs. The highest frequency band in Fig. 4.10(a) is a little bit higher than the highest frequency band in Fig. 4.10(b) because of the limitation of the dynamic tuning range of tuning screws. To sum up, the frequency tuning performance and the locations of TZs controlling the inline bandpass filter can be achieved simultaneously by tuning the resonant frequencies and FDCs, which are physically realized by these six tuning screws.

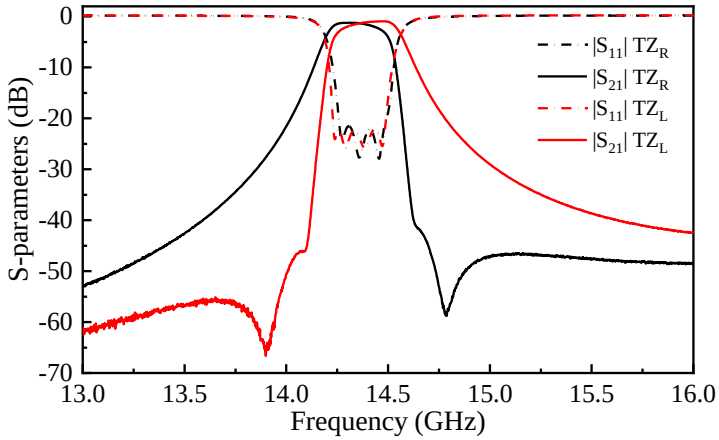

Figure 4.9 Measured S-parameters responses comparing TZs on the left and right sides of passband

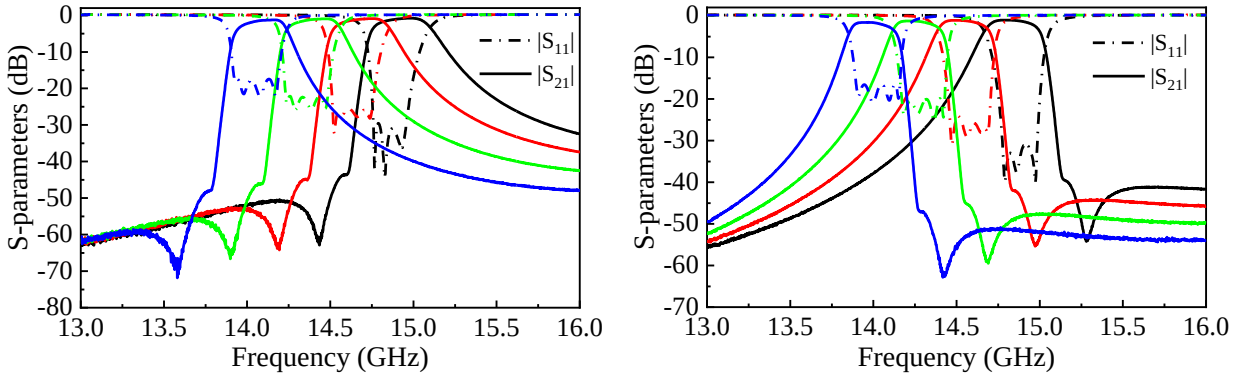

(a) (b)

Figure 4.10 Measured tunable responses of the inline bandpass filter. (a) TZs on the left sideband. (b) TZs on the right sideband

4.1.5 Conclusion

In this section, a synthesis methodology of inline tunable bandpass filters using FDCs has been presented. The locations of TZs can be switched and the operating frequencies can be tuned simultaneously by tuning the resonant frequencies and FDCs. To the best of our knowledge, this is the first time using the FDC technique to realize inline tunable bandpass filters with reconfigurable TZs. The inline topology simplifies the signal flow path, which brings less impact on other coupling coefficients and is easier for physical fabrication. The synthesis procedure of how to obtain the purposed matrices and the mechanism of how to reconfigurable the positions of TZs have been investigated in detail. For experimental validation, a fourth-order inline tunable bandpass filter has been synthesized, designed, fabricated, and measured with the guidance of the synthesis procedure. The reconfigured locations of TZs while maintaining the same return loss level of response, and the frequencies tuning performance are exhibited, which are consistent well with the simulated results.

4.2 Tunable bandpass filter with one switchable TZ by only tuning resonances

4.2.1 Introduction

This section is basically copied from one paper named *tunable bandpass filters with one switchable transmission zero by only tuning resonances*. Tunable bandpass filters (tBPFs) are playing a key role in modern wireless communication systems because of the urgent demand for multi-channel functions and requirements for volume and weight reduction of transceiver front-ends [50, 59, 83, 108, 123, 130-138]. On the other hand, reconfigurable filtering characteristics are attractive since various responses are usually needed for different channels, wherein the controllable transmission zeros (TZs) are concerned, especially those TZs on imaginary axis to improve the out-of-band rejections. For instance, a box-section or box-like topology can be employed to switch one TZ on the lower or upper side of the passband [123, 133, 134].

Besides controlling TZs to reconfigure the filtering characteristics, tuning frequencies is also an important feature for tBPFs. Generally, the frequency tuning and TZ controlling are independent, which would increase the number of design variables. To overcome this issue with limited tuning elements, two demonstrations have been reported in [136, 137]. Nevertheless, the mechanism of how to control the TZ was not discussed and the shortage of theoretical analysis leads to a limited tuning performance because of mismatch among coupling coefficients. Furthermore, they are only applicable to second-order microstrip tBPFs, and still there is a lack of theoretical guidance for arbitrary orders of tBPFs with one switchable TZ.

In this section, a methodology for tBPFs with one switchable TZ by only tuning resonant frequencies is presented, which can be applied to arbitrary filtering orders ($n \geq 2$). The switching mechanism of TZ is theoretically interpreted through coupling matrix synthesis and the performance of reconfigured filter has the same return loss level using a Chebyshev filtering function [14]. As an example, a fourth-order waveguide tBPF is experimentally demonstrated according to the theoretical guidance.

4.2.2 Methodology of controlling one TZ

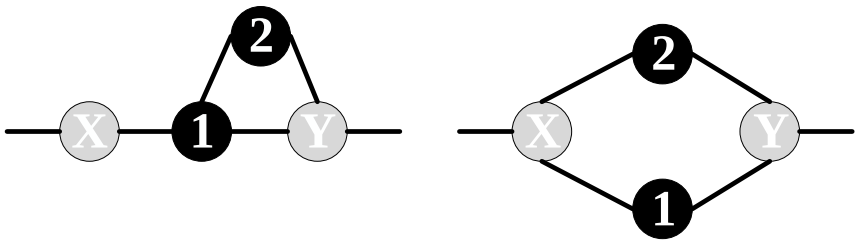

(a) (b)

Figure 4.11 Sub-topology of a BPF with one TZ. (a) Tri-section cascaded. (b) Box-like section cascaded

The methodology of controlling one TZ is introduced by coupling matrix analysis. One possible sub-topology to control one TZ is shown in Fig. 4.11(a). The location of TZ can be expressed by [108]

$$s = j\left(\frac{M_{12}M_{2Y}}{M_{1Y}} - M_{22}\right). \tag{4.11}$$

From (4.11), we can conclude: If the location of TZ needs to be symmetrically rotated, the signs of M_{22} (corresponding to the resonant frequency of node 2) and one of the coupling coefficients in the tri-section should be opposite in Fig. 4.11(a) (The black nodes numbered 1 and 2 represent resonators and the grey nodes numbered X and Y can be non-resonator, resonator, source or load. Solid line segments indicate couplings).

To solve this problem, coupling matrix rotation [97] is applied to eliminate the coefficient M_{12} with the equation and rotation angle θ as follows

$$M_R = R \cdot M \cdot R^T, \tag{4.12}$$

$$\theta = \frac{1}{2}\tan^{-1}\left(\frac{2M_{12}}{M_{22}-M_{11}}\right). \tag{4.13}$$

where M_R represents the matrix M after rotation. The rotation of matrix R is defined by rotation angle θ. R^T is the transpose of R. In R, all diagonal entries are 1 and off-diagonal entries are 0, except that $R_{11} = R_{22} = cos\theta$ and $R_{12} = -R_{21} = sin\theta$.

The rotated topology [139] is depicted in Fig. 4.11(b) and the corresponding location of TZ can be expressed by [108]:

$$s = -j\frac{M_{2X}M_{11}M_{2Y} + M_{1X}M_{1Y}M_{22}}{M_{2X}M_{2Y} + M_{1X}M_{1Y}}. \tag{4.14}$$

As can be seen, if only the signs of M_{11} and M_{22} (*i.e.* resonant frequencies of nodes 1 and 2) are changed, the location of TZ can be symmetrically rotated on the lower and upper sides of the passband. Hence, the minimum order to control one TZ by only tuning resonant frequencies is 2 (nodes X and Y represent source and load) and it is suitable for arbitrary filtering orders ($n \geq 2$).

Finally, the synthesis procedures to symmetrically switch one TZ on lower and upper sides of passband are summarized as follows:

1) The coupling matrix can be synthesized through a Chebyshev filtering function according to [14].
2) After coupling matrix simplification, the corresponding topology can be derived, which is partially the same as that in Fig. 4.11(a).
3) The final topology can be obtained by implementing coupling matrix rotations through (4.12) and (4.13).

Repeating the synthesis procedure, the return loss levels are the same if all the signs of the diagonal entries in the coupling matrix are altered.

4.2.3 Synthesis and design of waveguide BPF

As a demonstration and validation, a fourth-order waveguide BPF is synthesized and designed with the following specifications: in-band return loss (RL) of 26 dB, location of TZ switched between -1.6j and +1.6j, a center frequency of 10.8 GHz with 3-dB bandwidth of 380 MHz.

4.2.3.1 Synthesis of coupling matrices

With RL of 26 dB and position of TZ at -1.6j, the normalized coupling matrix can be synthesized using a Chebyshev filtering function in [14]

$$M = \begin{bmatrix} 0 & 1.1715 & 0 & 0 & 0 & 0 \\ 1.1715 & -0.0891 & 1.0675 & 0 & 0 & 0 \\ 0 & 1.0675 & -0.1527 & -0.6190 & 0.5968 & 0 \\ 0 & 0 & -0.6190 & 0.6819 & 0.8851 & 0 \\ 0 & 0 & 0.5968 & 0.8851 & -0.0891 & 1.1715 \\ 0 & 0 & 0 & 0 & 1.1715 & 0 \end{bmatrix}. \tag{4.15}$$

It can be seen all the mainline couplings are positive except for M_{23}. The next step is to substitute (4.12) and (4.13) into (4.15) to eliminate M_{23}, and the obtained coupling matrix is shown below

$$M = \begin{bmatrix} 0 & 1.1715 & 0 & 0 & 0 & 0 \\ 1.1715 & 0.0891 & 0.9425 & 0.5013 & 0 & 0 \\ 0 & 0.9425 & 0.4819 & 0 & -0.9425 & 0 \\ 0 & 0.5013 & 0 & -0.1011 & 0.5012 & 0 \\ 0 & 0 & -0.9425 & 0.5012 & 0.0891 & 1.1715 \\ 0 & 0 & 0 & 0 & 1.1725 & 0 \end{bmatrix}. \tag{4.16}$$

The corresponding responses of the matrix in (4.16) are depicted by red curves in Fig. 4.12. As seen, if the signs of the diagonal coefficients in (4.15) are altered, the location of the TZ would be switched to +1.6j while retaining the same RL level, which is also verified by black curves in Fig. 4.12. In short, two complementary frequency responses can be switched between each other by only tuning the resonant frequencies.

For experimental verification, a WR-90 standard-based waveguide-fed tBPF is modeled and simulated in ANSYS HFSS. The electromagnetic model of the tBPF is shown in Fig. 4.13, where all the couplings are realized by inductive coupling irises [140]. In this arrangement, resonators 1 and 4 operate with the fundamental mode TE_{110}, resonators 2 and 3 operate with dual modes TE_{120} and TE_{210}. The tuning screws are deployed at locations where the electric fields are the strongest in the cavity. As shown in Fig. 4.13(a), the screws of depth via_1 (red color) are deployed to tune the fundamental mode, while the screws of depth via_2 and via_3 (blue and black colors) are designed to tune the dual modes. The electric field distributions of the dual modes are depicted in Fig. 4.14. As can be seen, each of the dual modes is tuned using a pair of tuning screws because of two magnitude

peaks. Other screws in the middle of coupling irises are only set to adjust the coupling coefficients after fabrication.

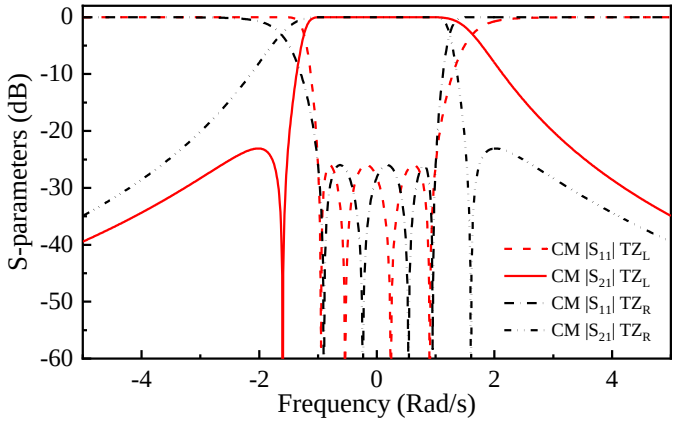

Figure 4.12 Normalized fourth-order frequency responses with one switchable TZ based on coupling matrix synthesis

4.2.3.2 Electromagnetic model of the proposed tBPF

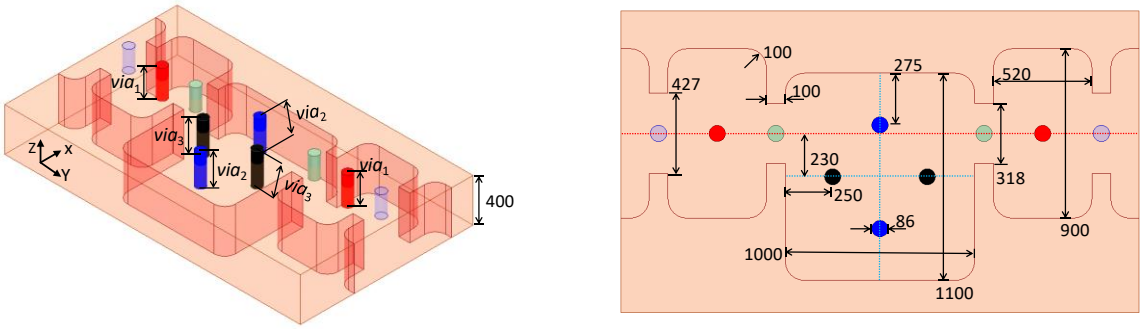

(a) (b)

Figure 4.13 Electromagnetic model of the designed tBPF. (a) 3-D overview. (b) Top view

Unit: mil

The tBPF is tuned by following the model-based vector fitting method proposed in [111, 113] and the coupling matrix shown in (4.16). By only tuning the screw depths *via*$_1$, *via*$_2$, and *via*$_3$, the simulated tunable responses are plotted in Fig. 4.15. As can be seen, frequency tuning and response reconfigurability are achieved simultaneously. The performance of the responses will be getting

worse when the passbands are tuned to lower frequencies. This is because all the physical coupling irises are fixed during the tuning process, introducing a mismatch between initially required and finally achieved coupling strengths. By tuning the screws for couplings, the filtering performance can be refined, the bandwidth can be controlled, and the tuning range can also be extended, but more tuning elements are needed for control. This is actually a trade-off between achieved performance and needed number of tuning elements. The small peaks on the upper side of the passband are excited by screws. Their frequencies would be shifted by tuning screws, and the magnitudes are always lower than -24 dB.

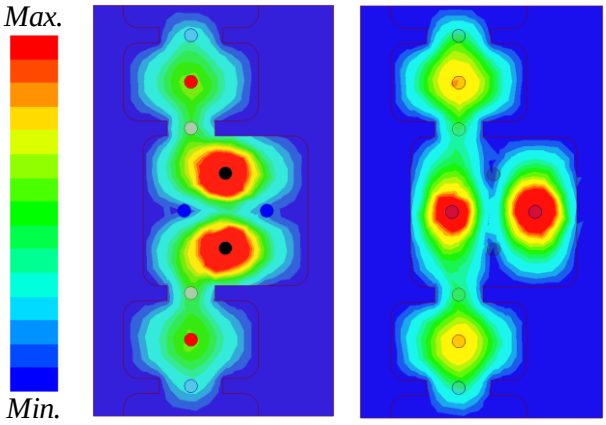

(a) (b)

Figure 4.14 Electric field distributions of the dual modes. (a) TE_{120}. (b) TE_{210}

4.2.3.3 Fabrication and measurement

The photograph of the fabricated tBPF prototype is displayed in Fig. 4.16. It is manufactured on a piece of aluminum 6061-T5. All the tuning screws are assembled and installed on the top cover. The measurement is progressed with WR-90 connectors and vector network analyzer N5224A. Both simulation and measurement results are plotted in Fig. 4.17. As can be seen, when TZ on the lower side of the passband is reconfigured to its upper side, the tuning frequency process will affect the physical coupling strength because of an equivalent wavelength changed in the dual modes. Hence, the absolute value of TZ on the upper side becomes larger which leads to a better out-of-

band rejection.

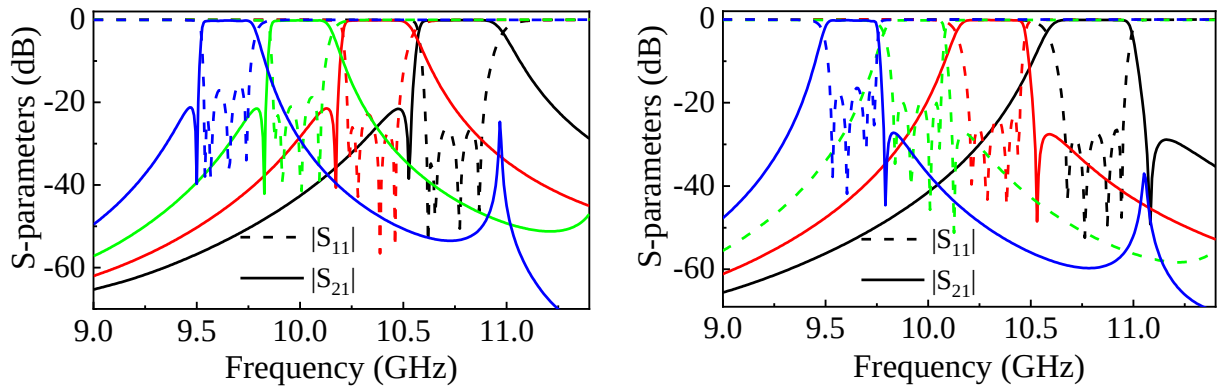

Figure 4.15 Simulated frequency responses of the proposed tBPF by only tuning resonances. (a) TZ on lower side of passband. (b) TZ on upper side of passband

With the filter centered at 10.8 GHz, the measured 3-dB bandwidth, IL, and RL of the response (TZ on the left) are 370 MHz, 0.34 dB, and 26 dB, respectively. The measured tunable performance of the tBPF is given in Fig. 4.18. Both responses, namely TZ on lower and upper sides, are measured with tuning frequency range from 9.5 GHz to 10.8 GHz, insertion loss (IL) from 0.34 dB to 1.40 dB, and 3-dB bandwidth from 230 MHZ to 370 MHz, respectively. The aforementioned magnitude of peaks are always lower than -40 dB. Table 4.1 lists the comparisons of our work with some other related state-of-the-art designs. Besides the switchable TZ, the frequency tuning range is also extended benefitting from the theoretical guidance.

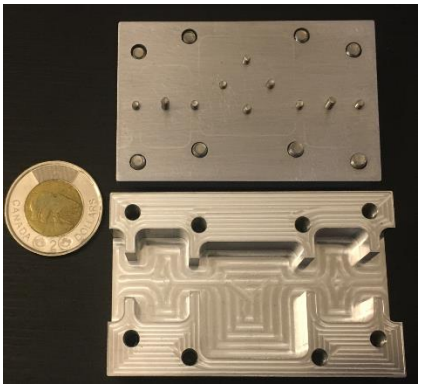

Figure 4.16 Photograph of the fabricated circuit prototype

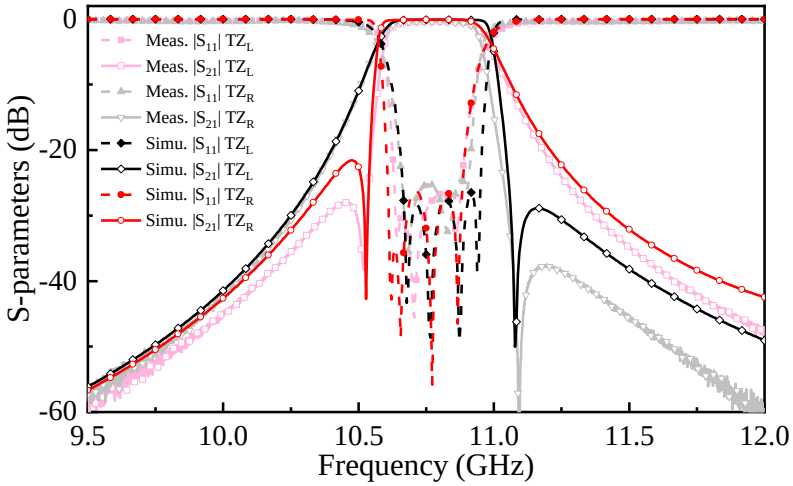

Figure 4.17 Comparison between simulated and measured results of the proposed tBPF with one switchable TZ by only tuning resonances

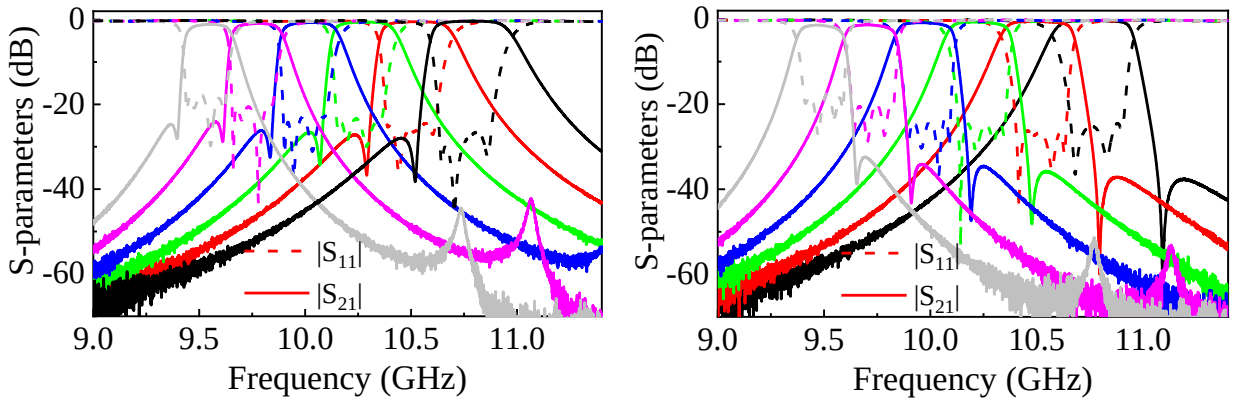

Figure 4.18 Measured frequency responses of the tBPF with frequency tuning. (a) TZ on the lower side of the passband. (b) TZ on the upper side of the passband

4.2.4 Conclusion

A methodology for tBPFs with one switchable TZ is proposed and presented with the demonstration of a fourth-order waveguide tBPF that is synthesized, designed, and verified by merely tuning resonances. The coupling matrix analysis is employed to theoretically guide the design of this type of tBPF with any order, which shows great potential in the development of high-quality and easily tuned reconfigurable waveguide BPFs and diplexers.

Table 4.1 Comparisons with other related state-of-the-art designs

Ref.	Type	f_o (GHz)	FBW @ f_o (%)	F-T Range (GHz)	F-T Pct.	Order	No. of TZ	Switchable TZ
[133]	ML	2.5	4.00	N/A	N/A	4	1	No
[134]	WG	7.5	5.80	N/A	N/A	4	1	No
[123]	COAX	1.8	2.78	N/A	N/A	4	1	Yes
[136]	ML	0.9	4.44	0.86-0.90	4.5%	2	1	Yes
[138]	SIW	8.0	5.00	N/A	N/A	2	1	No
Ours	**WG**	**10.8**	**3.42**	**9.50-10.80**	**12.8%**	**4**	**1**	**Yes**

CHAPTER 5 TUNABLE BANDPASS FILTER WITH WIDE FREQUENCY-TUNING RANGE AND CONSTANT BANDWIDTH USING MODE-SWITCHING CONCEPT

This chapter is basically from one paper, *tunable waveguide bandpass filter with wide frequency-tuning range and constant bandwidth using mode-switching concept*, and presents an approach to the development of tunable waveguide bandpass filters (BPFs) with a wide frequency-tuning range (FTR) while preserving a constant absolute bandwidth (ABW). The key to realize this feature is that the fundamental mode and the common mode in a rectangular cavity can be switched by controlling tuning elements. In deploying a tuning element in the center of a cavity, a frequency-tuning band can be formed by perturbing the fundamental mode. When the tuning element is connected to the top and bottom walls of the cavity, the fundamental mode is switched to the common mode. In this case, the lower band would be shifted to a higher band, which can then be tuned by extra tuning elements assigned to the common mode. The lower and higher bands can be combined by a suitable length-to-width ratio of the rectangular cavity to realize a wide FTR.

For demonstration, a Ku-band tunable BPF is fabricated and measured with an ABW of 360±10 MHz to achieve a 30.2% tuning range from 12.78 GHz to 17.30 GHz. Then, this configuration is investigated for introducing reconfigurable transmission zeros (TZs), which can be switched between the lower and upper sides of a passband. For verification, a Ku-band tunable BPF with one reconfigurable TZ is measured with a constant ABW of 400±10 MHz. When the TZ is on the left-hand side of the passband, the BPF yields a 31.2% tuning range from 12.41 GHz to 17.00 GHz, and when the TZ is on the right-hand side of the passband, it produces a 32.90% tuning range from 12.29 GHz to 17.13 GHz.

5.1 Introduction

Tunable bandpass filters (BPFs) are vital components in channelized and multifunction wireless systems. They are attractive and indispensable as they are set to replace generally required filter banks and decrease system volume, weight, and cost. With the development of emerging multi-standard and multi-function systems, tunable BPFs are required to exhibit a wide frequency-tuning range to cover as many frequency bands or channels as possible. Furthermore, a constant ABW is also crucial during the frequency tuning process to ensure a consistent quality channelized

information flow. Hence, the methods to design a wider FTR of BPFs with a constant ABW have received much attention and have become a challenging research topic.

Various approaches have been proposed in the last few decades [23, 24, 50, 73, 83, 85, 86, 141-149] in the development of wide FTR BPFs. The first method combines several tuning bands into one using switchable components such as switches, PIN diodes, or diplexers [141-145]. In [141], a microstrip line-based resonator was soldered with PIN diodes and varactor diodes. The lower-band and higher-band were tuned by varactor diodes and these two bands can be switched by PIN diodes in the same circuit. A larger than 3.3 frequency-tuning ratio was obtained because the two bands were contiguously jointed. In [142], two PIN diodes were employed to switch between the two channels of a tunable diplexer. These channels were designed in individual circuits and independently tuned by varactor diodes. The frequency-tuning ratio was 3.7 after the two channels were combined. Generally, this method can achieve a very wide FTR in microstrip technology. However, its operating frequency band is usually limited to the sub-6 GHz band due to insertion loss (IL) issues.

Cavity-based resonators have been studied and implemented for high-frequency applications. Perturbing resonant modes using electric and/or magnetic tuning elements can continuously shift center frequencies (CFs) [23, 24, 50, 73, 83, 85, 86, 146-149]. In [50], two-dimensionally tuned substrate integrated waveguide (SIW) cavities were realized by ferrite slabs and capacitors together, which are easier to realize a constant ABW. They not only allow for changing CFs but also optimize other key parameters simultaneously. A total FTR of 10.1% was experimentally achieved at 12 GHz. In [23], a tunable cavity composed of a resonating cavity and a dielectric perturbator was presented. A FTR of 20.6% at 11 GHz was realized by varying the rotation angle of the perturbator. Furthermore, some innovative configurations were employed to tune CFs while maintaining a constant ABW [85, 86]. In [85], a high-Q tunable waveguide BPF was configured with double septa to achieve a constant ABW in tuning CFs. A FTR of 9.0% at 15 GHz was obtained on the basis of a single tuning element. It can be observed that it is more difficult to create a wide FTR at a higher frequency. Meanwhile, the cavity-based resonators always make use of the same resonant modes in the previous developments.

In this work, tunable waveguide BPFs with a constant ABW are presented and demonstrated. Two modes, namely the fundamental mode and the common mode, can be switched in the same

rectangular cavity. The lower-band and higher-band generated by the two modes are combined with a suitable length-to-width ratio to realize a wide FTR at high frequencies.

The rest of the chapter is arranged as follows. The mechanism behind switching the two modes in the same cavity is introduced in Section 5.2. A Ku-band tunable BPF is designed, fabricated, and measured in Section 5.3. Based on the same configuration, the possibility to realize a tunable BPF having reconfigurable TZs is investigated, and a second-order BPF with one reconfigurable TZ is demonstrated in Section 5.4. Finally, the conclusion is drawn in Section 5.5.

5.2 Mechanism of two switchable modes in a cavity

The challenges to realize a wide FTR can be understood from the following four aspects:

(a) The resonant frequency of an operating mode must be tunable in a wide FTR. The fractional FTR is defined by

$$FTR = \frac{2\left(f_H - f_L\right)}{f_H + f_L}, \tag{5.1}$$

where f_H and f_L represent the CFs of the highest and lowest bands, respectively. Meanwhile, unloaded quality factor Qu of the cavity is a potential issue because it determines the IL of the response during the tuning process.

(b) The physical internal coupling coefficients should be compatible with the desired dynamic tuning range, which is defined as [108]

$$k_{ij} = \frac{M_{ij} * BW}{f_o} \ (i \neq j,\ i, j \neq S \text{ or } L), \tag{5.2}$$

where k_{ij} and M_{ij} are the physical internal coupling coefficient and internal coupling coefficient in a normalized coupling matrix, respectively. f_o and BW are the CF and ABW of the passband, respectively.

Considering the FTR defined in (5.1) and the constant ABW, the required physical internal coupling coefficient should be within the interval

$$k_{ij} \in \left[\frac{M_{ij} * BW}{f_H}, \frac{M_{ij} * BW}{f_L} \right]. \tag{5.3}$$

It is well-known that the value of M_{ij} is determined by a lowpass prototype filter, which affects the required dynamic range of k_{ij}. Besides, a wider BW needs a larger dynamic range of k_{ij}.

(c) The physical external quality factor needs to meet the required dynamic range, which is defined as [108]

$$\begin{aligned} Q_{eS} &= \frac{f_o}{BW * M_{S1}^2} \\ Q_{eL} &= \frac{f_o}{BW * M_{NL}^2} \end{aligned}. \tag{5.4}$$

where Q_{eS} and Q_{eL} are the physical external quality factors of input and output resonators, respectively [150]. N is the order of the filter. S and L denote source and load, respectively.

Considering the FTR defined in (5.1), the required physical external quality factors should meet

$$\begin{aligned} Q_{eS} &\in \left[\frac{f_L}{BW * M_{S1}^2}, \frac{f_H}{BW * M_{S1}^2} \right] \\ Q_{eL} &\in \left[\frac{f_L}{BW * M_{NL}^2}, \frac{f_H}{BW * M_{NL}^2} \right] \end{aligned}. \tag{5.5}$$

It can be seen from (5.3) and (5.5) that a wider BW, a larger value of M_{ij}, M_{S1}, and M_{NL}, and a wider FTR are a challenge for the physical realization of internal and external coupling coefficients.

(d) Spurious modes should be suppressed between f_L and f_H. The spurious modes mainly include two parts. In the first part, the higher-order modes are generated by the cavity. Effective ways to avoid them mainly include setting suitable excitation positions and changing the shape of resonant cavities. Therefore, the higher-order modes will not be excited or will stay far away from the targeted passband. In the second part, the spurious modes are generated by both tuning elements and cavities, which are tuned into the FTR. The states of the tuning elements—no matter how the resonant frequencies or the internal/external couplings are controlled—are different during the tuning process, which leads to a new spurious mode excitation or a resonant frequency shift of the existing spurious

mode. These modes are more difficult to suppress. Generally, the manner with which they will be addressed depends on the specific reason for the spurious mode resonances.

In short, the final FTR is restricted by these four mentioned aspects. If any one of these conditions is not satisfied, the realizable range of the FTR will be reduced.

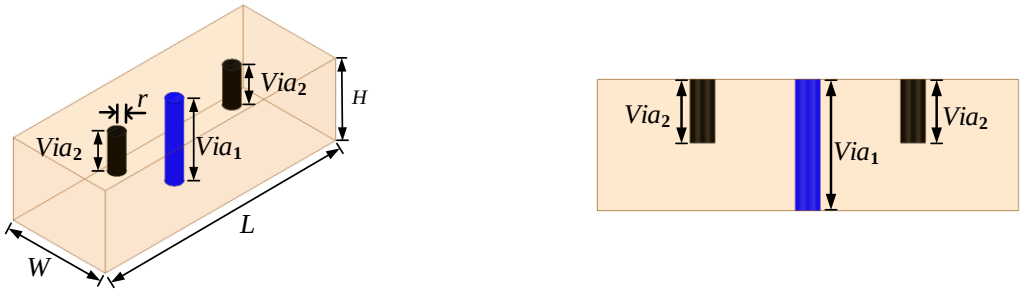

(a) (b)

Figure 5.1 Perspective view of a rectangular cavity with tuning screws. (a) 3-D view. (b) Side view

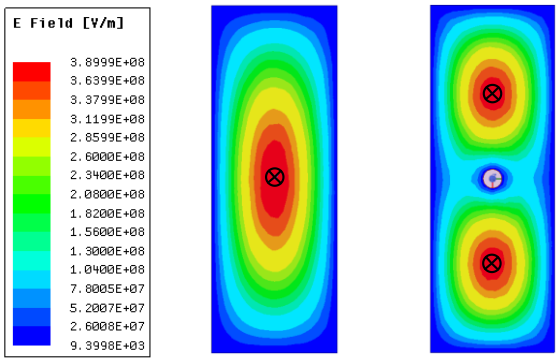

(a) (b)

Figure 5.2 Electric field distributions of two modes. (a) Fundamental mode. (b) Common mode

The two switchable modes in the same cavity are regarded as the operating modes to better meet the constraints. The fundamental mode in a rectangular cavity is chosen as the first operating mode, as shown in Fig. 5.1. The resonant frequency can be calculated by the following equation [151]

$$f_{mnl} = \frac{c}{2\pi\sqrt{\mu_r \varepsilon_r}} \sqrt{\left(\frac{m\pi}{W}\right)^2 + \left(\frac{l\pi}{L}\right)^2}, \tag{6}$$

where c is the velocity of light in a vacuum. μ_r and ε_r are the relative permeability and permittivity of a substrate, respectively. m and l are the numbers of variation in x- and z-direction, respectively.

The electric field distribution of the fundamental mode, TE_{101}, is depicted in Fig. 5.2(a). Loading a tuning screw with radius r at the center of the cavity would perturb the CF of the fundamental mode. The depth of the tuning screw in the blue color is defined by Via_1. A larger value of Via_1 leads to a lower resonant frequency of TE_{101}.

When the value of Via_1 equals the height of cavity H, or in other words when the screw is connected to the top and bottom layer of the cavity, the common mode as the second operating mode is generated. The resonant frequency of the common mode is higher than that of the fundamental mode. The electric field distribution of the common mode is shown in Fig. 5.2(b). As expected, two electric field peaks are in phase. Then, two extra tuning screws in black color are deployed in the cavity where the electric field is the most intensive. The depth of the extra tuning screws in the black color is defined by Via_2. The resonant frequency of the common mode can be tuned to a lower frequency with a larger value of Via_2.

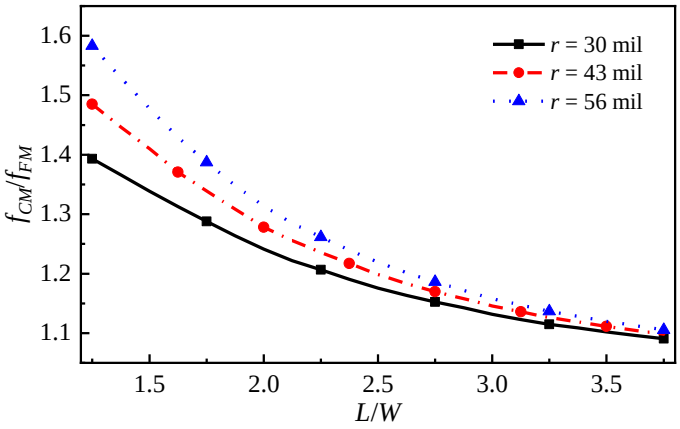

Figure 5.3 Frequency ratio of common mode to fundamental mode with various values of r under different length-to-width ratios of the cavity

If these two tuning frequencies generated by the two operating modes are overlapped, a wider FTR can be realized. Under this circumstance, the initial resonant frequencies of both modes and their tuning ability are investigated.

The initial resonant frequencies of both modes are simulated by the eigenmode analysis in the High-Frequency Structure Simulator (HFSS). With fixed W = 400 mil, different length-to-width ratios of the cavity are achieved by sweeping L. The frequency ratio of the common mode to the fundamental mode with various values of r is depicted in Fig. 5.3 (W = 400 mil. H = 311 mil. CM: common mode. FM: fundamental mode). With the same length-to-width ratio, the larger the value of r, the higher the resonant frequency of the common mode. The frequency ratio of the common mode to the fundamental mode decreases as the length-to-width ratio increases, suggesting that the initial resonant frequencies of the two modes are closer to each other.

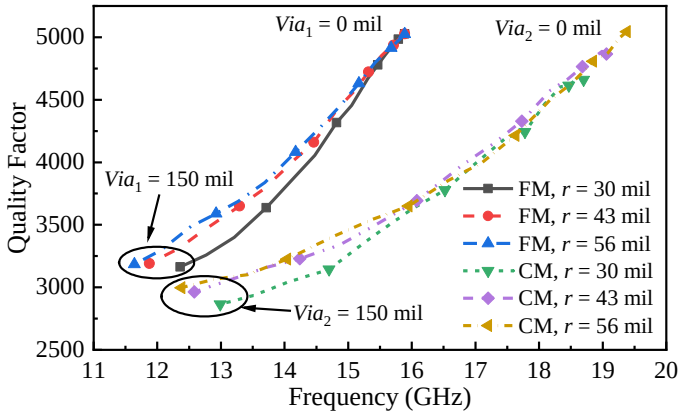

Figure 5.4 Unloaded quality factors Q_u of the fundamental mode and common mode with different values of r

To demonstrate the tuning capability of both modes, the length-to-width ratio of 2.5 is chosen as an example. Then, the values of Via_1 and Via_2 are swept from 0 mil to 150 mil. The frequency tuning range as well as the Q_u of both modes are given in Fig. 5.4 (H = 311 mil. CM: common mode. FM: fundamental mode). The FTR of the fundamental mode is from 11.5 GHz to 16.0 GHz with Qu from 3200 to 5000, while that of the common mode is from 12.5 GHz to 19.5 GHz with Qu from 2800 to 5000. At the overlapped frequencies, the Qu of the fundamental mode is higher than that of the common mode. Therefore, the higher-band can be realized by the common mode while the lower-

band can be realized by the fundamental mode to decrease the IL of responses during the tuning process. As a potential advantage, the required physical internal/external coupling coefficients may be easier to satisfy with the constraints.

Three different values of *r* are chosen based on the real radius size of the screws. Regardless of having a fundamental mode or common mode, it can be seen that a larger value of *r* brings up a wider FTR and a higher Qu. However, because of the wider FTR, a larger radius of the tuning screw is more sensitive to tune the same frequency.

In a practical filter design, the coupling irises for the internal and external couplings affect the initial resonant frequency as well as the FTR. After adding the irises, the initial resonant frequency of the mode will become lower and the corresponding FTR will become smaller. Accordingly, the initial length-to-width ratio of the cavity should be adjusted based on design specifications.

5.3 Tunable BPF with constant ABW

To experimentally validate the proposed concept, a second-order Ku-band BPF is designed, fabricated, and measured. There are two reasons for the selection of this second-order filter as a demonstration. First, the second-order filter design involves the four aspects mentioned in Section 5.2. Overcoming all the challenges in the realization of a wide FTR can be thus properly demonstrated with this BPF. Second, the order of a BPF is not an important factor affecting the FTR. Generally, in a lower-order filter, the values of the internal/external coupling coefficients in the normalized coupling matrix are larger. It can be observed in (5.3) and (5.5) that a larger value of normalized coupling coefficients requires a larger dynamic range of the physical coupling coefficients. However, a lower-order filter also exhibits a larger bandwidth in the normalized coupling matrix response. Considering these two aspects, the order of a filter does not have much impact on the couplings' physical realization.

The designed 3-dB ABW is 360 MHz and the required return loss (RL) is 23 dB. A normalized coupling matrix is synthesized using the Chebyshev filtering function [14], which is given by

$$[M]=\begin{bmatrix} 0 & 1.3459 & 0 & 0 \\ 1.3459 & 0 & 1.9446 & 0 \\ 0 & 1.9446 & 0 & 1.3459 \\ 0 & 0 & 1.3459 & 0 \end{bmatrix}. \tag{5.7}$$

The values of M_{12} and M_{S1} are 1.9446 and 1.3459, respectively. They are prepared for calculation in (5.3) and (5.5).

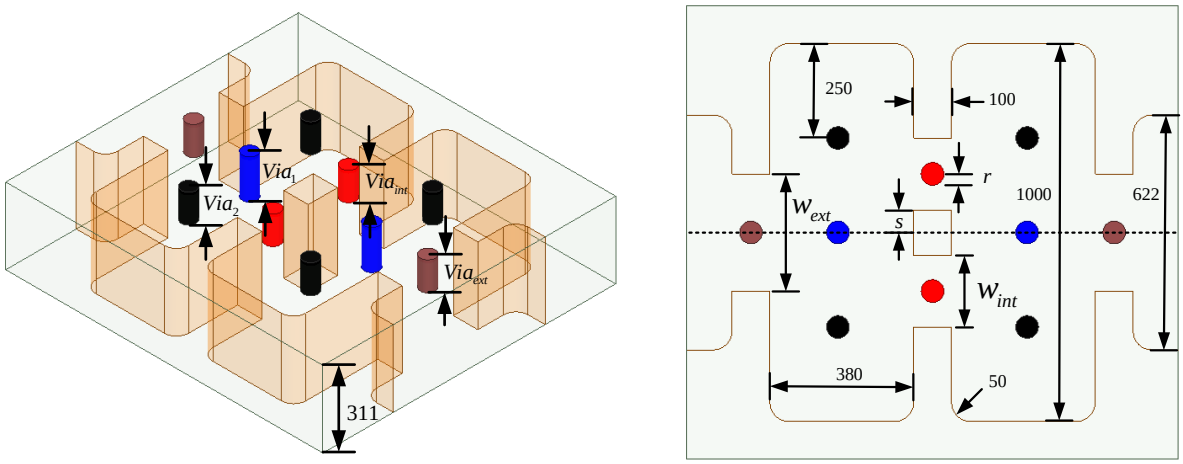

(a) (b)

Figure 5.5 The electromagnetic model of the proposed second-order BPF. (a) 3-D view. (b) Top view

The electromagnetic model of the second-order BPF is shown in Fig. 5.5. Two cavities are cascaded as resonator 1 and resonator 2. Each resonator is realized by two operating modes, which are tuned and switched using black and blue tuning screws. The width of the cavity is reduced from 400 mil to 380 mil because the coupling irises decrease the resonant frequencies of the resonator.

5.3.1 Internal coupling

As seen in Fig. 5.5(b), the physical internal coupling consists of two coupling irises and two tuning screws in the red color. The two irises are set symmetrically to prevent the excitation of spurious modes. The width of the internal coupling iris is defined by w_{int}. Considering the E-field

distributions of both modes shown in Fig. 5.2, the coupling irises should be shifted from the horizontal centerline to obtain a constant ABW over the whole tuning range. The distance is defined by *s*. The internal coupling coefficients are swept with different widths of coupling irises and various offset distances, as shown in Fig. 5.6 (FM: fundamental mode. CM: common mode. r = 30 mil). The product of physical coupling coefficient k_{ij} and resonant frequency f_o is set as the y-axis. As observed, no matter the mode, fundamental or common, the product (k_{ij}*f_o) is larger with wider coupling irises. If the value of s is increased, with the same value of w_{int}, the product of the fundamental mode is decreased while that of the common mode is increased.

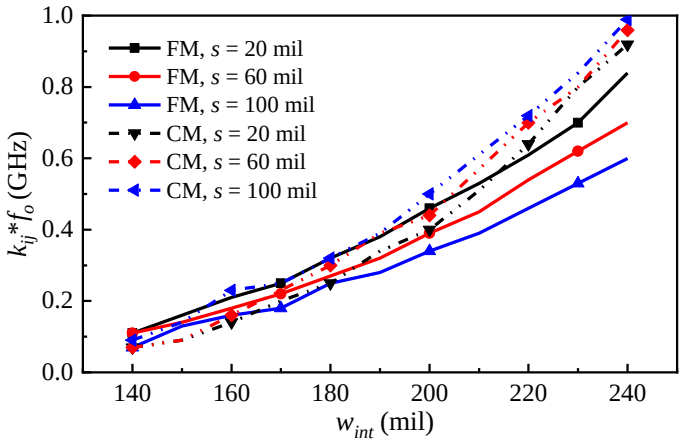

Figure 5.6 The internal coupling coefficients of both modes versus the width of the internal coupling irises as well as the offset distances

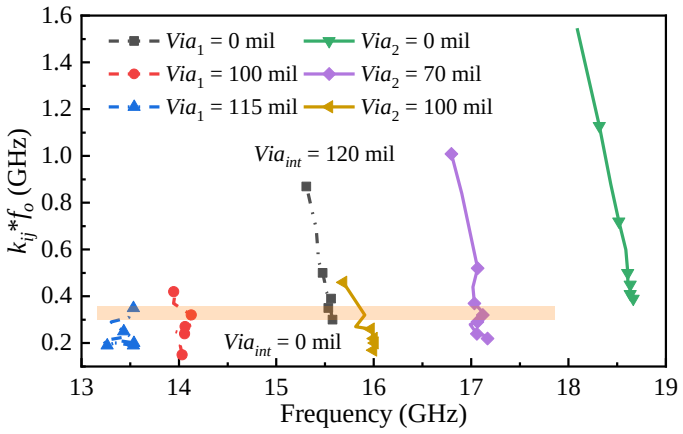

Figure 5.7 The dynamic range of the product of the physical internal coupling and the resonant frequency at different frequencies by sweeping the value of Via_{int}

As an example, the value of w_{int} is chosen as 190 mil and the value of s is chosen as 60 mil to estimate the dynamic range of the product. The depth of the red tuning screws is defined by Via_{int}, which is swept from 0 mil to 120 mil. Six different resonant frequencies are chosen to observe the dynamic range of the product with different values of Via_{int}. The results are depicted in Fig. 5.7. As observed, the product is bigger for a larger value of Via_{int}. If the resonant frequency of each mode is higher, the dynamic range of the product is larger. The common dynamic range of the products at different resonant frequencies can be implemented to realize a constant ABW. If the dynamic range of the product is chosen from 0.29 to 0.35 (the orange bar), the calculated ABW can be ranged from 410 MHz to 495 MHz because the value of M_{ij} is known from (5.7). The resonant frequency at around 18.5 GHz generated by the common mode cannot be employed to achieve a constant ABW response, which means that the FTR is decreased caused of the dynamic range of the physical internal coupling. This situation can be improved by decreasing the value of s and then again sweeping the values of Via_{int}. If the order of the BPF is higher than two, the other internal coupling irises can be designed by repeating the procedure mentioned above.

5.3.2 External coupling

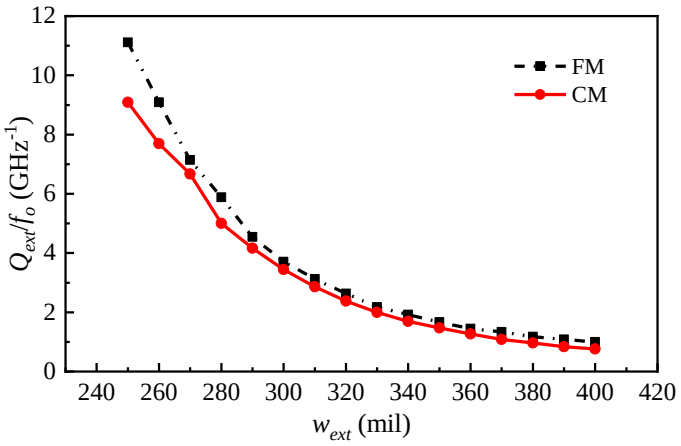

Figure 5.8 Physical external coupling coefficients of both modes versus the width of the external coupling iris

The physical external coupling consists of a coupling iris and a tuning screw, which are marked in brown color, as seen in Fig. 5.5(b). The coupling iris is located along the horizontal centerline to

avoid the excitation of higher-order modes. The width of the physical external coupling iris is defined by w_{ext}. The external coupling coefficients of both modes are swept with various values of w_{ext}, as shown in Fig. 5.8 (FM: fundamental mode. CM: common mode. r = 30 mil). The quotient of the physical external coupling Q_{ext} divided by resonance frequency f_o is set as the y-axis. It can be seen that a wider external coupling iris generates a smaller quotient (Q_{ext}/f_o) for both modes. Compared to the quotient of the fundamental mode, the quotient of the common mode is smaller for the same width of the external coupling iris.

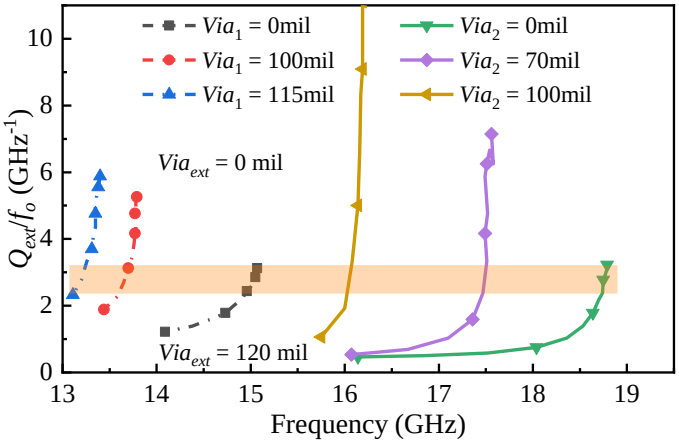

Figure 5.9 The dynamic range of the quotient at different frequencies by sweeping the value of Via_{ext}

As an example, the value of w_{ext} is chosen to be 310 mil to exhibit the dynamic range of the quotient. The depth of the brown tuning screw is defined by Via_{ext}, which is swept from 0 mil to 120 mil. Six different resonant frequencies, the same as in Fig. 5.7, are chosen to estimate the dynamic range of the quotient with different values of Via_{ext}. The results are given in Fig. 5.9. In this case, the quotient is smaller for a larger value of Via_{ext}. If the resonant frequencies of each mode are higher, the dynamic range of the quotient is smaller. If the dynamic range of the quotient is chosen from 2.3 to 3.1 (the orange bar), the calculated ABW can be ranged from 490 MHz to 660 MHz because the external coupling coefficients are known from (5.7). The ABW can be made smaller by decreasing the width of the external coupling iris w_{ext} and vice versa.

5.3.3 Filter design, fabrication, and measurement

The physical structure of a tunable BPF is designed based on the coupling matrix in (5.7). Each coupling coefficient in the coupling matrix can be mapped to the physical structure of the filter one by one. Each internal coupling iris can be adjusted by s and w_{int} accordingly, while each external coupling iris can be adjusted by w_{ext}. After optimization, the simulated results are depicted in Fig. 5.10. The constant ABW is 360 MHz, which is smaller than the calculated bandwidth (around 490 MHz) because the internal and external couplings affect each other in the final model. The dynamic range of each coefficient would also be decreased, which is caused by the coupling irises. The simulated FTR is 31.0%. Thereinto, the fundamental mode can be tuned from 12.73 GHz to 14.61 GHz, while the common mode can be tuned from 14.61 GHz to 17.40 GHz. It can be observed that the spurious mode is close to the highest band when the fundamental mode is tuned to a lower frequency. In this case, the spurious mode limits the FTR.

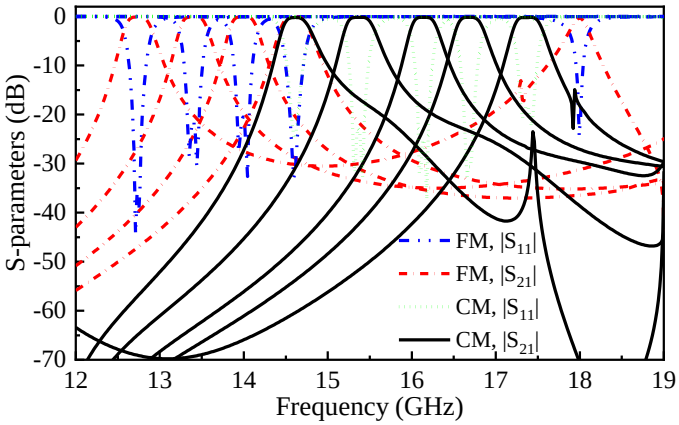

Figure 5.10 Simulated results of the tunable BPF with constant ABW

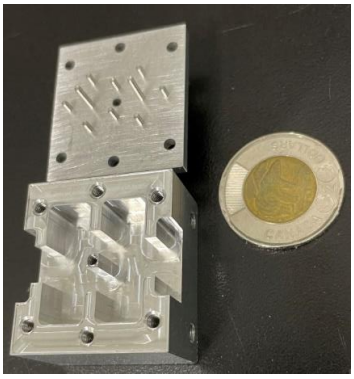

Figure 5.11 Photograph of the fabricated prototype

The photograph of the fabricated prototype is shown in Fig. 5.11 (FM: fundamental mode. CM: common mode). The filter is made on a piece of aluminum 6061-T5. All the tuning screws are deployed on the top cover. It is measured with the vector network analyzer Keysight N5224A and two WR62 connectors. The measured results are given in Fig. 5.12 (FM: fundamental mode. CM: common mode). The measured FTR is 30.1% with a constant ABW of 360 MHz ± 10 MHz. The fundamental mode can be tuned from 12.78 GHz to 14.51 GHz, while the common mode can be tuned from 14.62 GHz to 17.30 GHz. Notably, the common mode can be tuned to a lower frequency, but the overlapped frequency will be replaced by the fundamental mode due to the IL issue. The IL during the tuning process is from 0.3 dB to 1.7 dB, which can be improved by silver plating. The measured results are consistent with the simulated results.

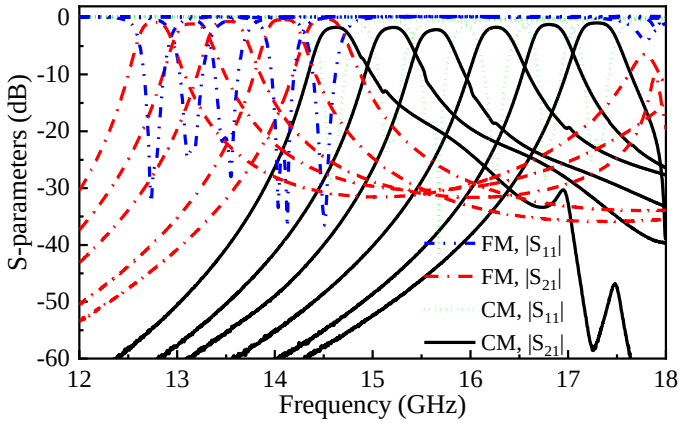

Figure 5.12 Measured results of the tunable BPF

5.4 Tunable BPF with one reconfigurable TZ

This configuration is studied for the purposes of introducing reconfigurable TZs. Limited by the configuration itself, the cross-coupling [9, 20, 74] is introduced with difficulty in this situation because of the coupling iris design. An in-line topology using frequency-dependent couplings (FDCs) [75, 76, 96] is employed to introduce reconfigurable TZs. A filter with one reconfigurable TZ is designed, fabricated, and measured. The designed 3-dB ABW is 400 MHz, and the required RL is 23 dB. The TZ can be reconfigured between +4.8j to -4.8j.

5.4.1 Synthesis of the coupling matrix

The filter order of two is chosen for the same reason. The normalized coupling matrix is synthesized

using the Chebyshev filtering function [108]. After rotating and normalizing [98], the coupling matrices with an FDC topology are given as follows:

$$M = \begin{bmatrix} 0 & 1.2616 & 0 & 0 \\ 1.2616 & \mp 0.7891 & 1.8905 & 0 \\ 0 & 1.8905 & \mp 0.7892 & 1.2616 \\ 0 & 0 & 1.2616 & 0 \end{bmatrix} \tag{5.8}$$

$$C = \begin{bmatrix} 0 & 0 & 0 & 0 \\ 0 & 1 & \mp 0.3939 & 0 \\ 0 & \mp 0.3939 & 1 & 0 \\ 0 & 0 & 0 & 0 \end{bmatrix}, \tag{5.9}$$

where M is the constant coupling matrix, and C is the capacitance matrix. It can be observed that if the signs are changed from negative to positive in the diagonal coupling coefficients, M_{11} and M_{22}, in M and the mainline coupling coefficient, C_{12}, in C, then the location of TZ can be switched from +4.8j to -4.8j. The corresponding responses in matrices (5.8) and (5.9) are depicted in Fig. 5.13 (TZR: Transmission zero on the right side of the passband. TZL: Transmission zero on the left side of the passband). As observed, the location of TZ is switched from the upper side to the lower side of the passband, and the responses retain the same RL level.

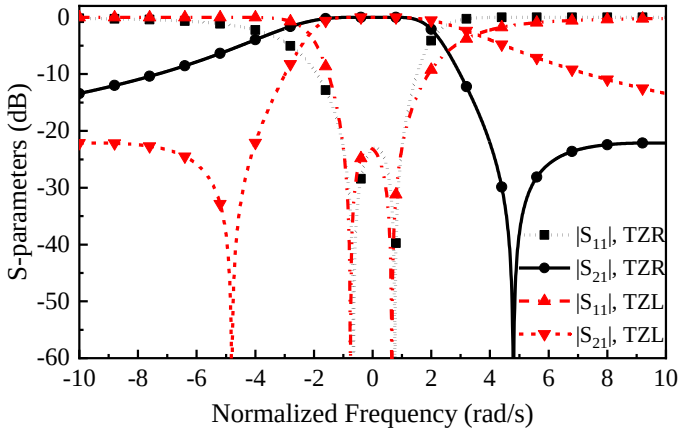

Figure 5.13 Normalized second-order filter responses with one reconfigurable TZ based on coupling matrix synthesis

5.4.2 Filter design with one reconfigurable TZ

The electromagnetic model of the filter with one reconfigurable TZ is shown in Fig. 5.14. It can be seen that the method to control the physical external coupling coefficients as well as the method to turn both operating modes of the fundamental and common mode are the same as mentioned in Section 5.3. The resonator 1 and resonator 2 are frequency-dependent coupled by the two red partial-height posts.

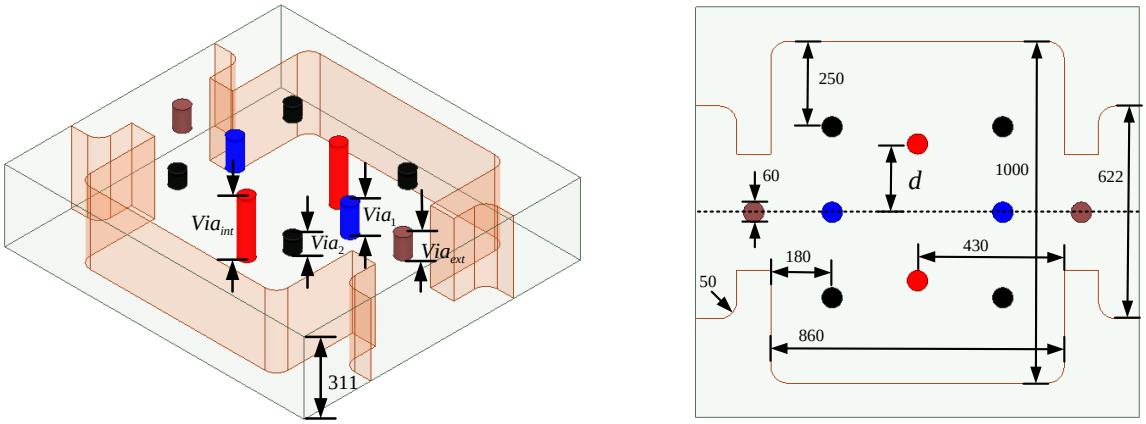

(a) (b)

Figure 5.14 The electromagnetic model of the proposed second-order BPF with one reconfigurable TZ. (a) 3-D view. (b) Top view

The method to physically control the location of TZ is investigated in detail. The depth of the red posts is defined by Via_{int}, and its position which shifted from the horizontal centerline is defined by d. The common mode is obtained by Via_1 = 311 mil and Via_2 = 0 mil. First, with d fixed at 200 mil and the depth of the partial-height posts tuned, the corresponding locations of TZ are given in Fig. 5.15(a). Thus, the positions of TZ shift to a lower frequency with a larger value of Via_{int}. Then, with Via_{int} fixed at 155 mil and the posts' position moved far away from the horizontal centerline, the corresponding location of TZ are described in Fig. 5.15(b). As observed, the positions of TZ also shift to a lower frequency if the posts move closer to the sidewall. Therefore, both the parameters of d and Via_{int} can control the location of TZ. Finally, with a fixed bandwidth and both d and Via_{int}

tuned simultaneously, it can be observed in Fig. 5.15(c) that the TZ is close to the passband if the posts are closer to the sidewall with a shorter depth. Since *d* is fixed and Via_{int} can be tuned in the physical structure, the value of *d* mainly determines the initial position of TZ, and the value of Via_{int} is employed to reconfigure the location of TZ.

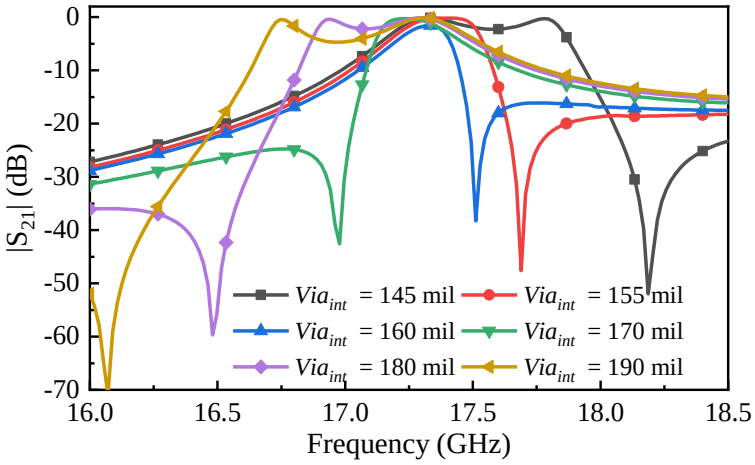

(a)

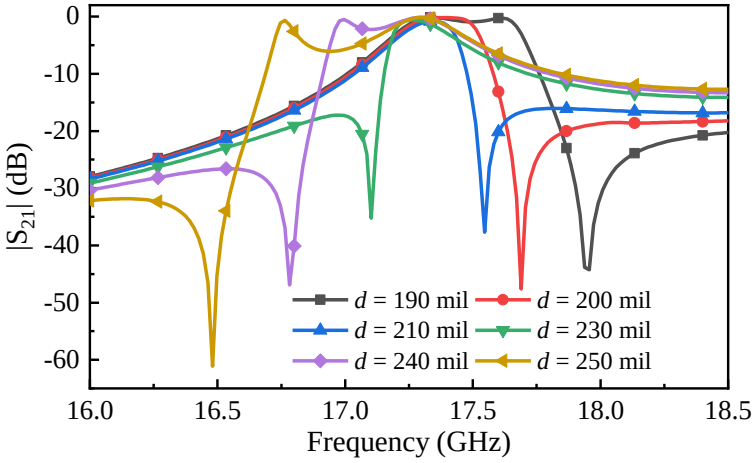

(b)

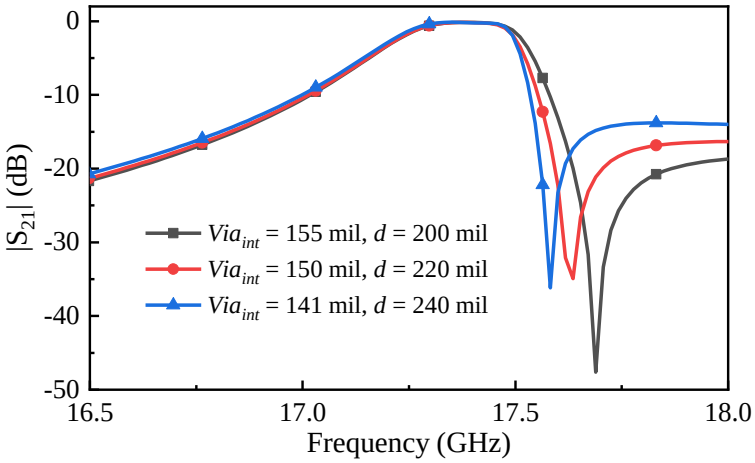

(c)

Figure 5.15 Physical realization of the frequency-dependent coupling for the common mode with Via_1 = 311 mil and Via_2 = 0 mil. (a) S-parameters responses by tuning the depth of the partial-height posts with fixed d = 200 mil. (b) S-parameters responses by moving the posts far away from the horizontal centerline with fixed Via_{int} = 155 mil. (c) S-parameters responses for controlled locations of TZ by simultaneously changing d and Via_{int}

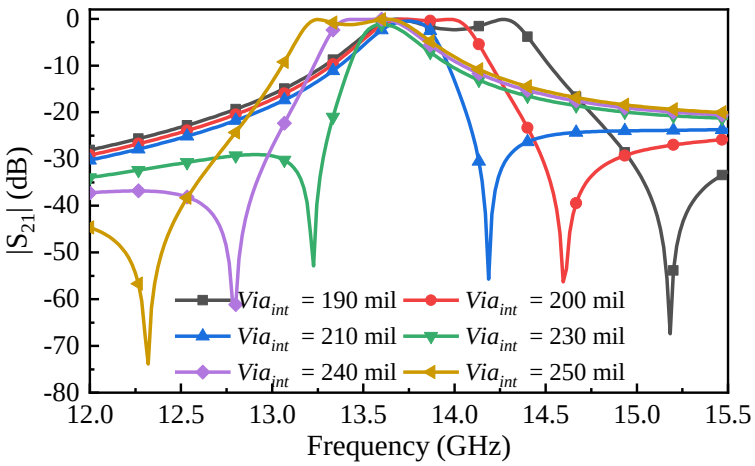

(a)

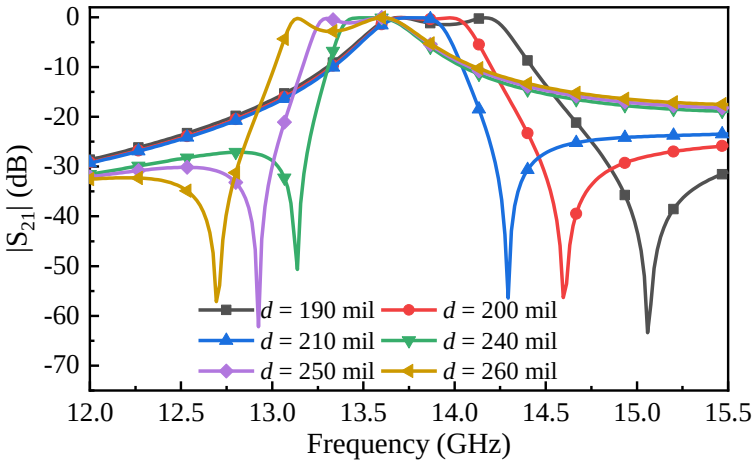

(b)

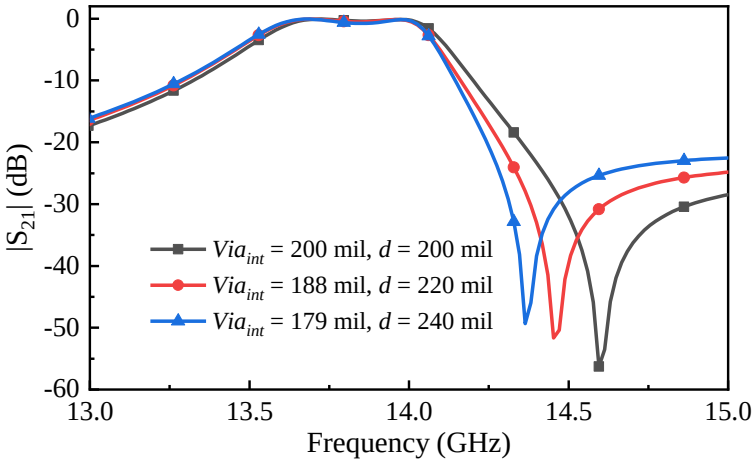

(c)

Figure 5.16 Physical realization of the frequency-dependent coupling for the fundamental mode with Via_1 = 0 mil and Via_2 = 0 mil. (a) S-parameters responses by tuning the depth of the partial-height posts with fixed d = 200 mil. (b) S-parameters responses by moving the posts far away from the horizontal centerline with fixed Via_{int} = 200 mil. (c) S-parameters responses for controlled locations of TZ by simultaneously changing d and Via_{int}

The same way to physically control the location of TZ is validated on the fundamental mode. The fundamental mode is obtained by Via_1 = 0 mil and Via_2 = 0 mil. First, by maintaining d = 200 mil and tuning the depth of partial-height posts, the corresponding locations of TZ are given in Fig.

5.16(a). As described, the positions of TZ shift to a lower frequency with a larger value of Via_{int}, which is similar to the feature of the common mode. Then, by maintaining Via_{int} = 200 mil and moving the position of posts far away from the horizontal centerline, the corresponding locations of TZ are described in Fig. 5.16(b). As can be seen, the positions of TZ also shift to a lower frequency if the posts move closer to the sidewall, which is also consistent with the feature of common mode. Finally, by maintaining the same bandwidth and tuning both d and Via_{int} simultaneously, it can be observed in Fig. 5.16(c) that the TZ is close to the passband if the posts are closer to the sidewall with a shorter depth.

In conclusion, the location of TZ can be deployed and tuned by a fixed value of d and a tunable value of Via_{int}. This method is effective for both fundamental and common modes. The simulated results after optimization are depicted in Fig. 5.17 (FM: fundamental mode. CM: common mode). The simulated FTR is 32.06% if the TZ is on the left side of the passband. As shown in Fig. 5.17(a), the passband can be tuned from 12.44 GHz to 17.19 GHz with a constant ABW of 400 MHz. The simulated FTR is 32.85% if the TZ is on the right side of the passband. As shown in Fig. 5.17(b), the passband can be tuned from 12.49 GHz to 17.40 GHz with the same constant ABW. A slight difference between the two FTRs is mainly caused by the initial resonant frequencies of the two modes.

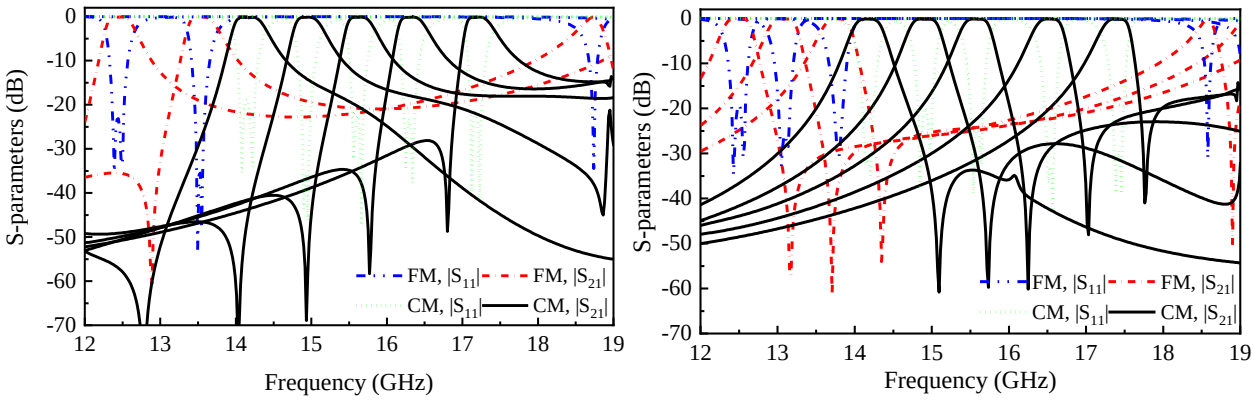

Figure 5.17 Simulated results of the tunable BPF. (a) TZ on the left side of the passband. (b) TZs on the right side of the passband

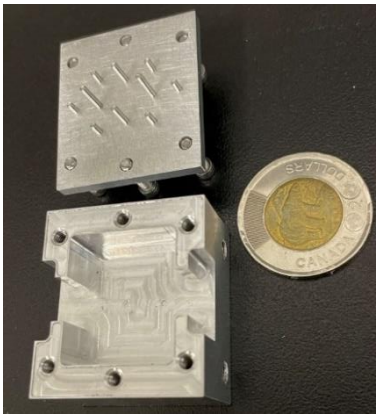

Figure 5.18 Photograph of the fabricated tunable BPF with one reconfigurable TZ

5.4.3 Fabrication and measurement

The photograph of the fabricated tunable BPF with one reconfigurable TZ is shown in Fig. 5.18. The filter is also made on a piece of aluminum 6061-T5, and all the tuning screws are arranged and integrated on the top cover. The measured results are shown in Fig. 5.19 (FM: fundamental mode. CM: common mode). The measured FTR is 31.20% if the TZ is on the left side of the passband. As seen in Fig. 5.19(a), the passband can be tuned from 12.41 GHz to 17.00 GHz with a constant ABW of 400 MHz ± 10 MHz. The IL during the tuning process is changed from 0.6 dB to 1.4 dB. The measured FTR is 32.90% if the TZ is on the right side of the passband. As seen in Fig. 5.19(b), the passband can be tuned from 12.29 GHz to 17.13 GHz with a constant ABW of 400 MHz ± 10 MHz. The IL during tuning ranges from 0.4 dB to 1.3 dB. No matter the TZ's location on the left or right side of the passband, the RL level of the response is always better than 20 dB during the tuning process.

Table 5.1 lists the comparisons with other related state-of-the-art tunable filter designs whose operating frequencies are above 6 GHz. It is seen that our designs not only achieve a very wide FTR with a constant ABW but also introduce reconfigurable TZs. It should be noted that a higher-order filter can be realized by cascading the corresponding number of cavities. For example, a third-order BPF with one TZ can be realized by cascading three rectangular cavities which are coupled by one FDC iris and one internal coupling iris, as mentioned in Section 5.3. To increase the number of reconfigurable TZs, more structures having FDC irises, as shown in Fig. 5.14, can be cascaded.

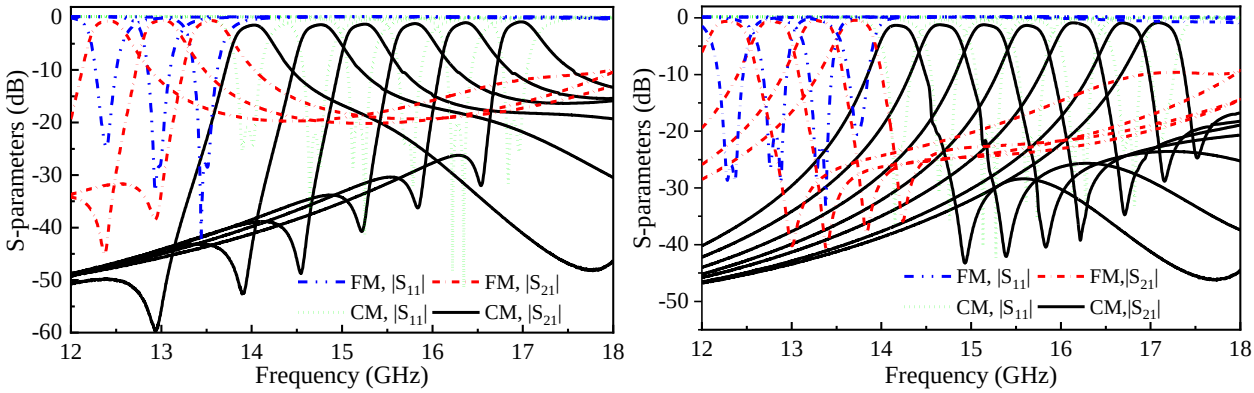

Figure 5.19 Measured results of the tunable BPF. (a) TZ on the left side of the passband. (b) TZ on the right side of the passband

Table 5.1 Comparisons with other related state-of-the-art designs

Ref.	f_H (GHz)	f_L (GHz)	FTR* 100%	ABW (MHz)	Filter Order	No. of TZ	Reconfigurable TZ
[50]	11.95	10.80	10.11	450	2	0	N.A.
[23]	12.19	9.92	20.53	516	3	0	N.A.
[85]	16.20	14.80	9.04	300	4	0	N.A.
[73]	11.68	11.29	3.40	50	4	2	No
[146]	26.45	25.55	3.46	32	5	0	N.A.
[147]	19.48	19.00	2.50	54.5	4	0	N.A.
[24]	19.7	19.36	1.74	180	4	0	N.A.
[148]	12.30	11.62	5.69	200	4	0	N.A.
Our works	**17.30**	**12.78**	**30.10**	**360**	**2**	**0**	**N.A.**
	17.07	**12.30**	**32.48**	**400**	**2**	**1**	**Yes**

Ref.: Reference. FTR: Frequency tuning range. ABW: Absolute bandwidth. No. of TZ: Number of transmission zero. N.A.: Not applicable.

5.5 Conclusion

This chapter presents the configuration for a wide FTR of BPFs with a constant ABW. Two modes can be switched and tuned in the same rectangular cavity. Two bands generated by two operating

modes can be combined into one to realize a wide FTR with a suitable length-to-width ratio in the rectangular cavity. Moreover, this configuration is investigated in detail for introducing reconfigurable TZs. Two demonstrations with and without reconfigurable TZs have been designed, fabricated, and measured. The measured results show that both designs have yielded over 30% FTRs.

CHAPTER 6 BAND-RECONFIGURABLE TUNABLE BANDPASS FILTERS BASED ON MODE-SWITCHING CONCEPT

This chapter is basically copied from one paper, *band-reconfigurable tunable bandpass filters based on mode-switching concept*, and presents a method for the development of band-reconfigurable tunable bandpass filters (BPFs) using a mode-switching concept. The key to realize this feature is that the first higher-order mode of TE_{201} can be switched to the diagonal modes using tuning elements in the square waveguide cavity. A pair of tuning elements are deployed on the diagonal line of a cavity while the other pair is deployed on its anti-diagonal line. If the two pairs of tuning elements have the same depths in the cavity, the first higher-order mode of TE_{201} can be realized and its resonant frequency can be tuned. If the tuning elements have different depths, TE_{201} mode can be switched to the diagonal modes, whose resonant frequencies can be tuned individually.

Accordingly, the corresponding tunable BPF can be reconfigured between single- and dual-band states. Moreover, a flexible number of transmission poles can also be implemented in the dual-band state. For experimental verifications, two band-reconfigurable tunable BPFs are designed, fabricated, and measured in Ku-band. The first design has 2 and 2+2 poles in the single- and dual-band states, respectively, whereas the second design introduces one transmission zero (TZ), which has 3 and 3+2 poles in the single- and dual-band states, respectively. Regardless of single- and dual-band responses, each band can be frequency-tuned.

6.1 Introduction

Reconfigurable bandpass filters (BPFs) are attractive in recent years because they play a key role in modern communication systems not only to meet the requirements of multi-standard and multi-function systems, but also to replace the filter banks to decrease volume, weight, and cost. From the perspective of the response of a single-band BPF, tunable center frequency (CF) is the most common feature as it covers a wide range of operating bands to replace many fixed-frequency BPFs. Generally, the electric and/or magnetic field perturbations can be employed to realize this function [41, 50, 53, 144]. In [50], a two-dimensionally tuned substrate integrated waveguide (SIW) BPF with a 20% tuning range at CF of 12 GHz is realized using varactor diodes and ferrite slabs

together. Additionally, by introducing transmission zeros (TZs) at the upper or lower side of the passband, the out-of-band suppression can be enhanced so that the crosstalk between channels can be reduced. The approach to introducing TZs on the imaginary axis of the complex plane includes cross-coupling scenarios [20, 22, 74, 97], frequency-dependent couplings (FDCs) [76, 95, 96], and extracted-pole topologies [116, 152, 153]. In [22], a box-like topology-based waveguide BPF has one controllable TZ and a 12.8% tuning range at 10 GHz, which can simultaneously control the location of the TZ and the CF by only tuning the resonant frequencies of the coupled resonators.

To better meet the requirements of multiple standards, the filter is required to extend operating bands. This topic is very attractive and has been widely investigated in recent years [85, 141, 142, 154, 155]. The first method is to use switchable components, such as switches, PIN diodes, or diplexers, to switch the initial resonant frequency first and then tune the CF of the band. In [141], PIN diodes are used to switch in or out the quarter-wavelength or half-wavelength microstrip line-based resonators for low-band or high-band modes, and varactor diodes are used to tune the CF of the band. Eventually, an extra-wide frequency tuning range from 550 MHz to 1900 MHz by combining low- and high-bands is obtained. The second method is to design two or multiple simultaneous operating bands in a BPF [156-160]. Each band is required to be independently frequency-tuned. In [158], a dual-band BPF is designed based on evanescent-mode cavity resonators with two capacitive loadings. There are two independently tunable passbands covering 1.156 GHz to 1.741 GHz of the lower band and 2.242 GHz to 3.648 GHz of the higher band. However, the limitation is that the number of bands in both methods cannot be changed.

Band-reconfigurable BPFs can flexibly control the number of the operating bands and extend the operating frequencies [48, 161-166]. In [162], the filter configuration can be converted from a two-pole dual-passband mode to a four-pole single-passband mode using a switchable J-inverter. Each band can be frequency-tuned using silicon varactors and the number of passbands can be changed by PIN diodes. However, the total number of poles cannot be altered. In [163], a band-switchable SIW tunable BPF can have a passband either in S- or X- band, or have two passbands in S- and X-band at the same time. The single-passband response can be regarded as the only part of the dual-passband response. Although the number of poles could be changed with the number of passbands, the band switching does not introduce another response.

In this work, band-reconfigurable tunable BPFs using the mode-switching concept are presented and demonstrated. Not only the total number of poles can be changed, but also the passbands could also be switched from a single-band to a dual-band with different CFs. The key to realize this feature is that the first higher-order mode of TE_{201} can be switched to two diagonal modes using tuning elements in a square cavity. At the same time, the tuning elements can be employed to tune the resonant frequencies of each mode.

The rest of the chapter is organized as follows. The resonator structure is introduced in Section 6.2. In Section 6.3, a band-reconfigurable BPF, which has 2 and 2+2 poles in the single- and dual-band states, respectively, is designed, fabricated, and measured in Ku-band. In Section 6.4, the other design, which has 3 and 3+2 poles in the single- and dual-band states, respectively, introduces one TZ in the response of the three-pole band. Notably, the dual-band state has a different number of poles in the passbands. At last, the conclusion is drawn in Section 6.5.

6.2 Resonator structure

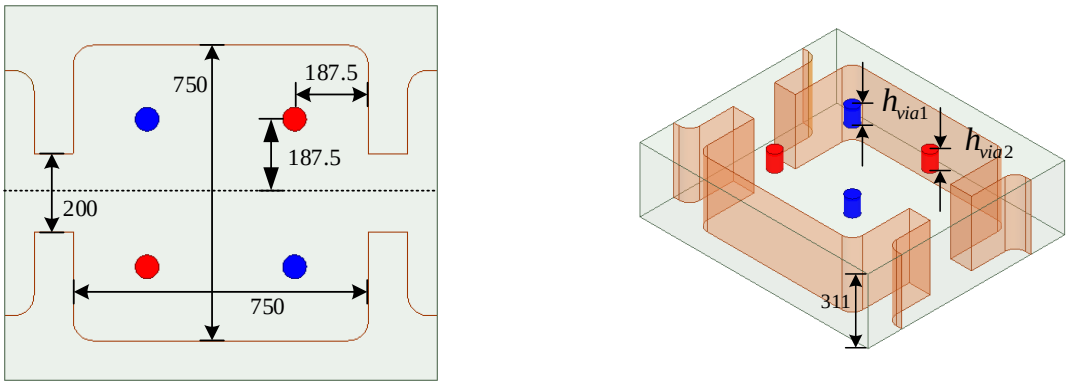

(a) (b)

Figure 6.1 Perspective view of a square waveguide cavity with tuning screws. (a) Top view. (b) 3-D view

A square waveguide cavity is shown in Fig. 6.1. A pair of tuning screws in blue color is deployed on the diagonal line of the cavity while the other pair in red color is deployed on its anti-diagonal

line, as shown in Fig. 6.1(a). The depth of the tuning screws in blue and red colors in the cavity are defined as h_{via1} and h_{via2}, respectively, as shown in Fig. 6.1(b). If $h_{via1} = h_{via2}$, the first higher-order mode of TE_{201} would be excited, and its electric field distribution is depicted in Fig. 6.2(a). If h_{via1} and h_{via2} have different depths, the mode TE_{201} would be switched to two diagonal modes, named diagonal mode 1 and diagonal mode 2, and their electric field distributions are depicted in Fig. 6.2(b) and Fig. 6.2(c), respectively.

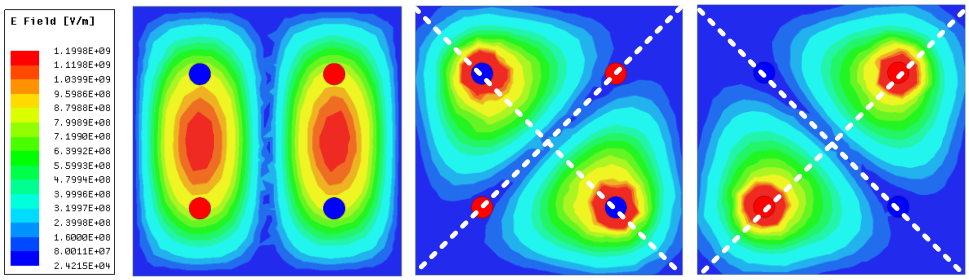

(a) (b) (c)

Figure 6.2 Electrical field distributions of the three modes. (a) Mode TE_{201}. (b) Diagonal mode 1. (c) Diagonal mode 2

The initial resonant frequency of TE_{201} mode can be calculated using the following equation [151]

$$f_{mnl} = \frac{c\sqrt{m^2 + l^2}}{2L\sqrt{\mu_r \varepsilon_r}}. \tag{6.1}$$

where c is the velocity of light in a vacuum, μ_r and ε_r are the relative permeability and permittivity of a substrate, respectively, L is the length of the square waveguide cavity, m and l are the numbers of variations in x- and z-directions, respectively.

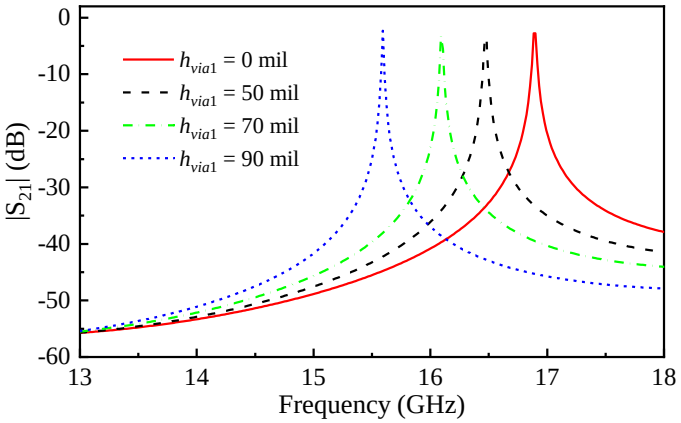

(a)

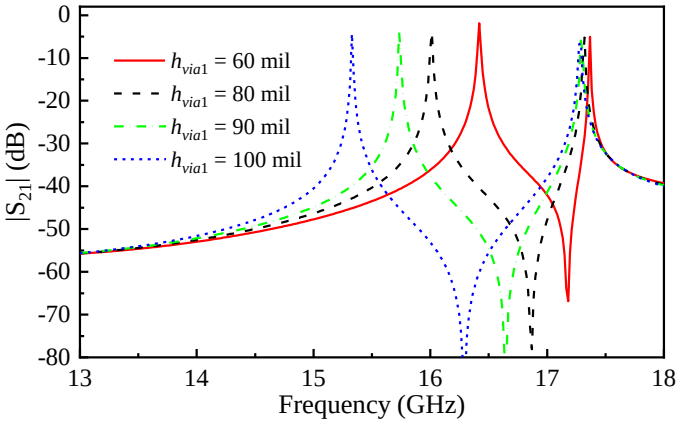

(b)

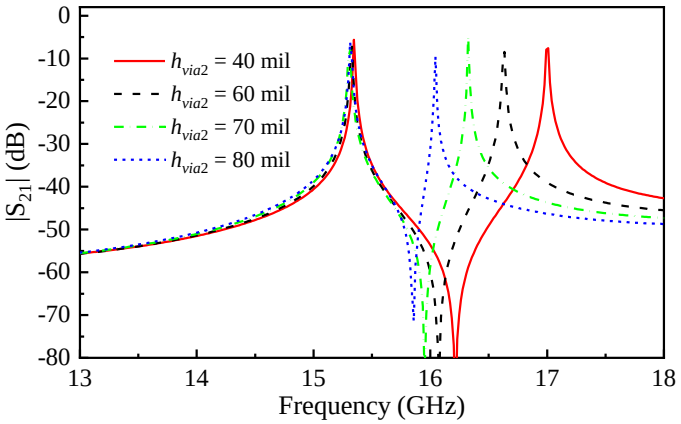

(c)

Figure 6.3 Frequency tuning for each mode. (a) TE_{201} mode with $h_{via1} = h_{via2}$. (b) Diagonal mode 1 with h_{via2} = 0 mil. (c) Diagonal mode 2 with h_{via1} = 100 mil

Then, the frequency-tuning characteristics of the modes are simulated in the High Frequency Structure Simulator (HFSS). If $h_{via1} = h_{via2}$, the resonant frequency of mode TE_{201} becomes lower when the depth of the tuning screws becomes deeper. As shown in Fig. 6.3(a), the resonant frequency of TE_{201} mode is tuned from 15.6 GHz to 17.0 GHz when the value of h_{via1} is changed from 0 mil to 90 mil. If h_{via2} = 0 mil and sweeping the value of h_{via1} from 60 mil to 100 mil, the resonant frequency of diagonal mode 2 is maintained at around 17.5 GHz while the resonant frequency of diagonal mode 1 is tuned from 15.3 GHz to 16.4 GHz, as shown in Fig. 6.3(b). Similar to [71], one TZ is also generated between the two resonant frequencies to enhance the out-of-band suppression[71, 80-82] If h_{via1} = 100 mil and sweeping the value of h_{via2} from 40 mil to 80 mil, the resonant frequency of diagonal mode 1 is maintained at around 15.3 GHz while the resonant frequency of diagonal mode 2 is tuned from 16.0 GHz to 17.0 GHz, as shown in Fig. 6.3(c). Since the two diagonal modes are orthogonal and the deployed tuning screws for one diagonal mode almost do not affect the resonant frequency of the other diagonal mode, the resonant frequencies of the two diagonal modes can be tuned individually.

The unloaded quality factors Q_us of the modes are simulated by eigenmode analysis in the HFSS. By sweeping the value of h_{via1} from 0 mil to 150 mil, the relationships between the resonant frequencies and the Q_us are shown in Fig. 6.4 (The curve of TE_{201} mode is extracted with $h_{via2} = h_{via1}$. The curve of diagonal mode 1 is extracted with h_{via2} = 0 mil. The characteristic curve of diagonal mode 2 is the same as the curve of diagonal mode 1). As observed, these two curves are almost overlapped, which means that these modes have the same frequency-tuning ability as well as the same Q_u at the same frequency.

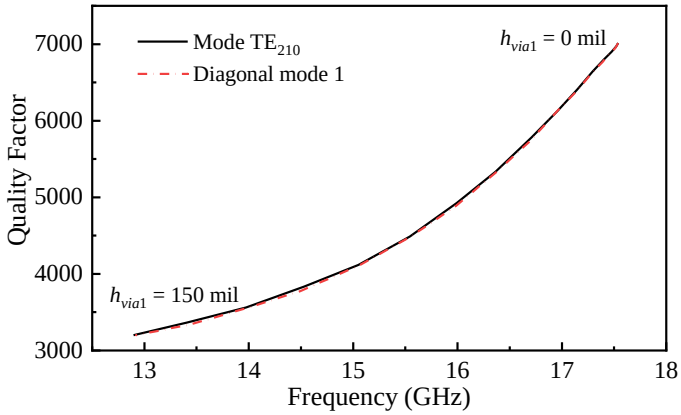

Figure 6.4 Unloaded quality factors Q_us of the first higher-order mode of TE_{201} and diagonal mode 1 by sweeping h_{via1} from 0 mil to 150 mil

6.3 Band–reconfigurable BPF with the same numbers of poles in the passbands

6.3.1 Coupling topology and geometric configuration

A band-reconfigurable BPF operating at Ku-band is designed, fabricated, and measured. The physical structure of the filter is realized by two cascaded cavities mentioned in Section II. If the filter operates on the single-band state, it has 2 poles and the corresponding topology is given in Fig. 6.5(a). Each cavity has one resonator, which is implemented by TE_{201} mode. The physical external quality factor and internal coupling coefficient are defined by Q_{ext} and k_{12}, respectively. If the filter operates on the dual-band state, it has 2+2 poles and the corresponding topology is given in Fig. 6.5(b). Each cavity has two resonators, which are implemented by the diagonal modes 1 and 2. The superscripts I and II denote the lower and the upper bands, respectively. The lower band is realized by the diagonal mode 1 and the corresponding physical external quality factor and internal coefficient are defined by Q_{ext}^{I} and k_{12}^{I}, respectively. The upper band is realized by the diagonal mode 2 and the corresponding physical external quality factor and internal coefficient are defined by Q_{ext}^{II} and k_{12}^{II}, respectively.

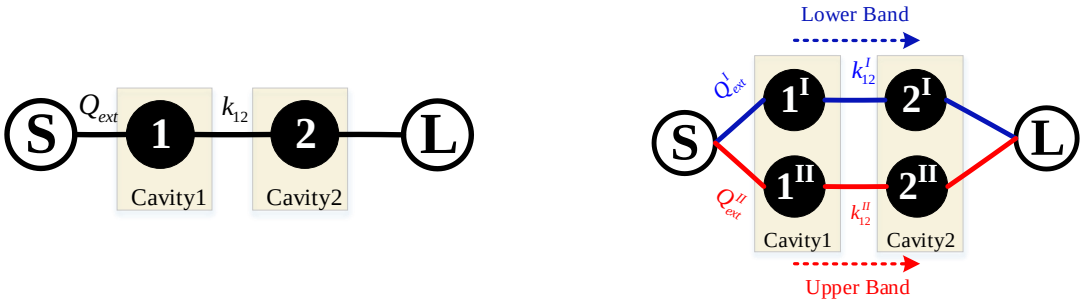

(a) (b)

Figure 6.5 Coupling topology for the corresponding model of the band-reconfigurable BPF. (a) Topology for single-band state implemented by TE_{201} mode. (b) Topology for dual-band state implemented by the diagonal modes 1 and 2

The electromagnetic model of the filter is depicted in Fig. 6.6. As seen in Fig. 6.6(a), the pair of blue tuning screws are set to tune the resonant frequency of diagonal mode 1, while the pair of red tuning screws are set to tune the resonant frequency of diagonal mode 2. The physical external quality factors and internal couplings are realized by inductive irises. As seen in Fig. 6.6(b), the width of the external coupling iris is defined by w_{ext} and the distance shifted from the centerline of the cavity is defined by s_{ext}. The width of the internal coupling iris is defined by w_{int} and the distance shifted from the centerline of the cavity is defined by s_{int}.

6.3.2 Specifications, coupling matrices, and coupling designs

As an example, the initial specifications of the filter design require the return loss (RL) of 20 dB in each band, the CFs of 14.80 GHz and 16.90 GHz at lower and upper bands, respectively. The 3dB-bandwidths are 320 MHz and 200 MHz at lower and upper bands, respectively.

A normalized coupling matrix is synthesized using the Chebyshev filtering function [14], which is given by

$$M = \begin{bmatrix} 0 & 1.2247 & 0 & 0 \\ 1.2247 & 0 & 1.6583 & 0 \\ 0 & 1.6583 & 0 & 1.2247 \\ 0 & 0 & 1.2247 & 0 \end{bmatrix}. \tag{6.2}$$

The normalized internal and external coupling coefficients are 1.6583 and 1.2247, respectively.

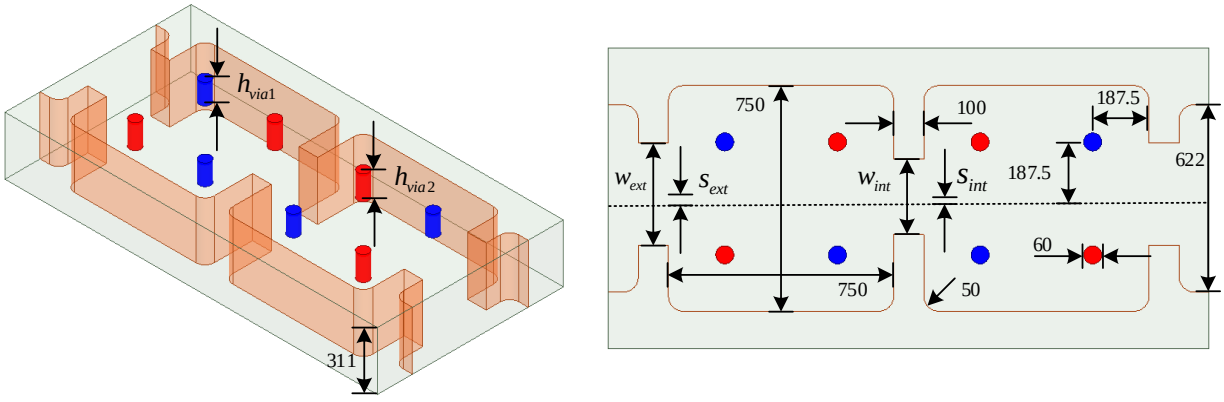

(a) (b)

Figure 6.6 The electromagnetic model of the band-reconfigurable BPF with the same numbers of poles in the passbands. (a) 3-D view. (b) Top view

The relationship between the normalized internal coupling coefficient M_{ij} and the physical internal coupling coefficient k_{ij} can be described below

$$k_{ij} = \frac{BW * M_{ij}}{f_o}. \tag{6.3}$$

where BW and f_o represent the bandwidth and CF of the band, respectively.

According to the CFs and bandwidths needed, the required physical internal coupling coefficients k_{12}^{I} and k_{12}^{II} in the lower and upper bands are 0.0151 and 0.0083, respectively.

To satisfy the values of k_{12}^{I} and k_{12}^{II} at the same time, the first step is to set h_{via1} = 100 mil and h_{via2} = 0 mil to reach the initial CFs at 14.80 GHz and 16.90 GHz, respectively. Then, sweeping the

value of w_{int} from 200 mil to 300 mil and the value of s_{int} from -20 mil to 20 mil simultaneously, the relationship between k_{12}^{I} and k_{12}^{II} is described in Fig. 6.7. It can be observed that both values of k_{12}^{I} and k_{12}^{II} become larger with a larger value of w_{int}. If the value of s_{int} is increased, the value of k_{12}^{I} becomes smaller while the value of k_{12}^{II} becomes larger. Therefore, both physical internal coupling coefficients can be flexibly selected by controlling the value of w_{int} and s_{int} simultaneously.

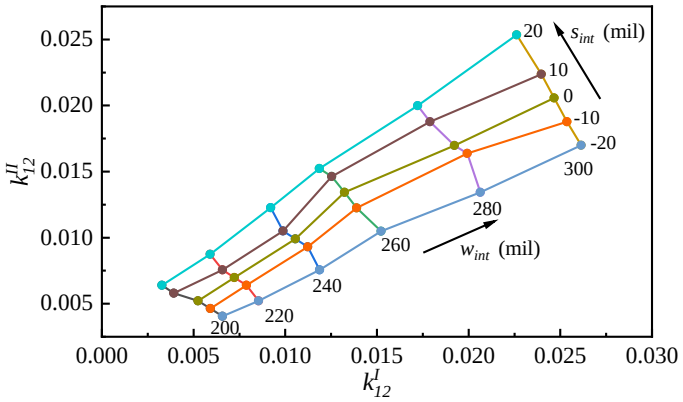

Figure 6.7 The relationship between k_{12}^{I} and k_{12}^{II} by sweeping values of w_{int} and s_{int} simultaneously

The relationship between the normalized external coupling coefficient M_{S1} ($M_{S1} = M_{2L}$) and the physical external quality factor Q_{ext} can be described below

$$Q_{ext} = \frac{f_o}{BW * M_{S1}^2}. \tag{6.4}$$

The required physical external quality factors Q_{ext}^{I} and Q_{ext}^{II} in the lower and upper bands are 73.08 and 133.52, respectively, which can be calculated through (6.4).

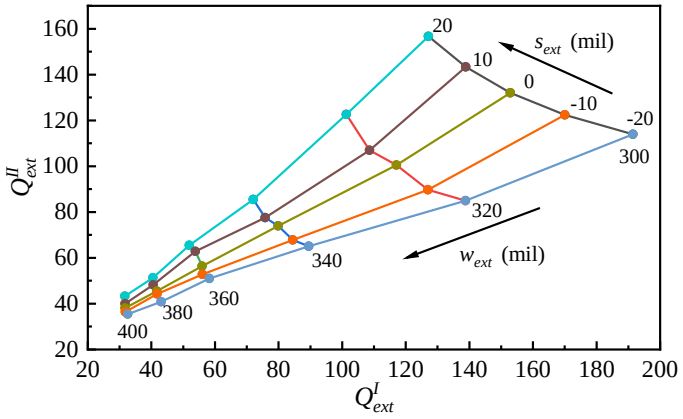

Figure 6.8 The relationship between Q^{I}_{ext} and Q^{II}_{ext} by sweeping values of w_{ext} and s_{ext} simultaneously

To satisfy the values of Q^{I}_{ext} and Q^{II}_{ext} at the same time, the value of w_{ext} is swept from 300 mil to 400 mil and the value of s_{ext} is swept from -20 mil to 20 mil simultaneously. The relationship between Q^{I}_{ext} and Q^{II}_{ext} is depicted in Fig. 6.8. It can be observed that both values of Q^{I}_{ext} and Q^{II}_{ext} become smaller with a larger value of w_{ext}. If the value of s_{ext} is increased, the value of Q^{I}_{ext} becomes smaller while the value of Q^{II}_{ext} becomes larger. Hence, both physical external quality factors can be satisfied simultaneously with suitable values of w_{ext} and s_{ext}.

Consequently, in the dual-band state, the physical external quality factors and internal coupling coefficients can be realized by adjusting w_{int}, s_{int}, w_{ext}, and s_{ext} together. The bandwidth ratio of lower and upper bands is controllable. However, in the single-band state, it may have over-coupling or under-coupling issues because all the coupling irises are selected. The required physical external quality factor and internal coupling coefficient in the single-band state are determined by the selected resonant frequency.

Since the change of s_{int} from -20 mil to 20 mil has almost no effect on the physical internal coupling coefficient, the coefficient k_{12} is selected by sweeping the value of w_{int} from 200 mil to 300 mil and by tuning h_{via1} and h_{via2} (h_{via1} = h_{via2}) from 30 mil to 90 mil at the same time. The relationship between w_{int} and k_{12} with various resonant frequencies is shown in Fig. 6.9. For each resonant frequency, the physical internal coupling coefficient k_{12} becomes larger with a wider w_{int}. For a

fixed value of w_{int}, k_{12} becomes smaller with a lower resonant frequency. Since w_{int} will be fixed after the dual-band state design, the k_{12} is determined by the selected resonant frequency, which is controlled by the depth of tuning screws.

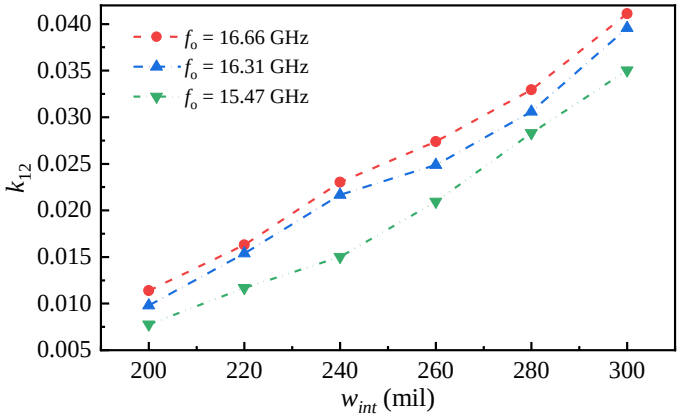

Figure 6.9 The relationship between w_{int} and k_{12} with various resonant frequencies: f_o = 16.66 GHz with h_{via1} = 30 mil and h_{via2} = 30 mil; f_o = 16.31 GHz with h_{via1} = 60 mil and h_{via2} = 60 mil; f_o = 15.47 GHz with h_{via1} = 90 mil and h_{via2} = 90 mil

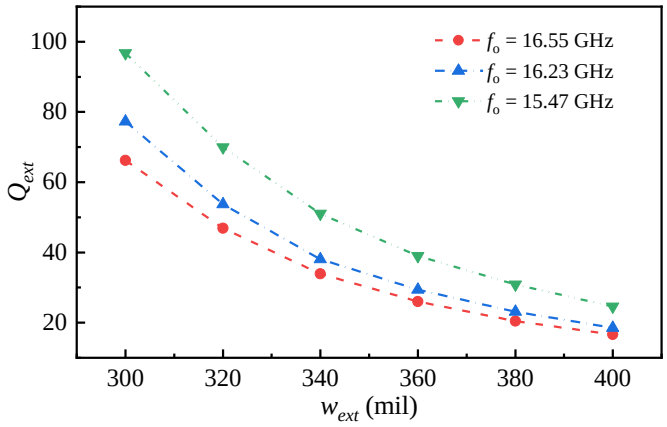

Figure 6.10 The relationship between w_{ext} and Q_{ext} with various resonant frequencies: f_o = 16.55 GHz with h_{via1} = 30 mil and h_{via2} = 30 mil; f_o = 16.23 GHz with h_{via1} = 60 mil and h_{via2} = 60 mil; f_o = 15.47 GHz with h_{via1} = 90 mil with h_{via2} = 90 mil

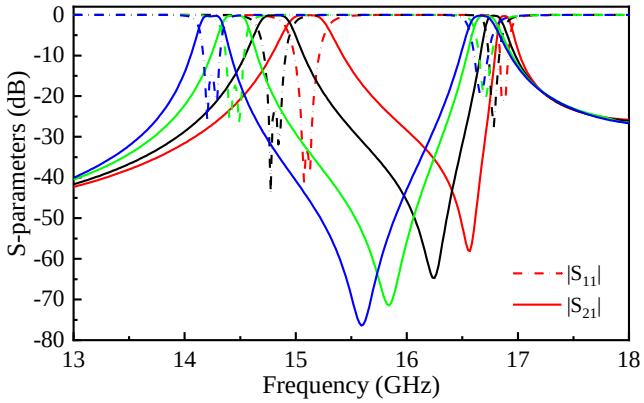

(a)

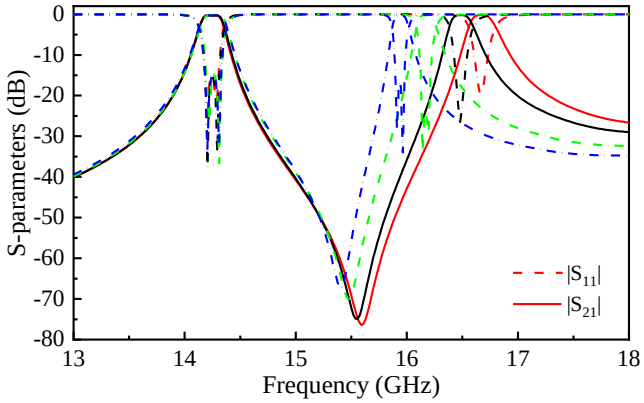

(b)

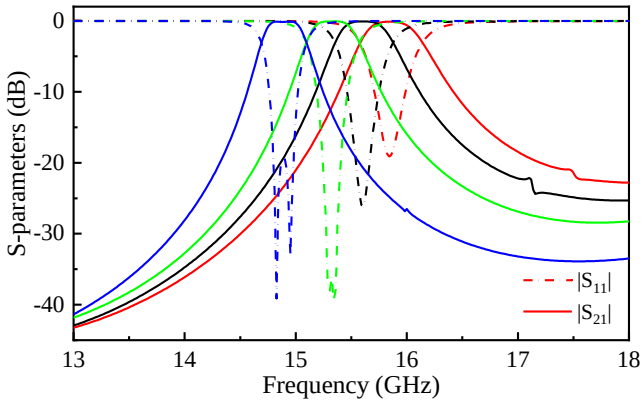

(c)

Figure 6.11 Simulated frequency-tuning performance of the band-reconfigurable BPF. (a) Tunable lower band by tuning h_{via1} from 90 mil to 115 mil and maintaining h_{via2} = 30 mil. (b) Tunable upper band by tuning h_{via2} from 30 mil to 80 mil and maintaining h_{via1} = 115 mil. (c) Tunable single-band by tuning h_{via1} from 0 mil to 90 mil with $h_{via1} = h_{via2}$

Since the change of s_{ext} from -20 mil to 20 mil has almost no effect on the physical external quality factor, the coefficient Q_{ext} is selected by sweeping the value of w_{ext} from 300 mil to 400 mil and tuning h_{via1} and h_{via2} ($h_{via1} = h_{via2}$) from 30 mil to 90 mil at the same time. The relationship between w_{ext} and Q_{ext} with various resonant frequencies is shown in Fig. 6.10. The physical external quality factor Q_{ext} becomes smaller with a larger value of w_{ext}. For a fixed value of w_{ext}, Q_{ext} becomes larger with a lower resonant frequency. Since w_{ext} will be fixed after the dual-band state design, the Q_{ext} is also determined by the resonant frequency. In short, the possible over- or under-coupling issues can be overcome by selecting a suitable initial resonant frequency in the single-band state.

6.3.3 Simulation, fabrication, and measurement

The physical structure of the band-reconfigurable BPF shown in Fig. 6.6 can be designed accordingly. After optimization, the values of w_{int}, s_{int}, w_{ext}, and s_{ext} are 250 mil, 5 mil, 340 mil, and 15 mil, respectively. The reason for the difference between the optimized and calculated values is that the existing coupling irises affect the resonant frequencies as well as the coupling coefficients.

The simulated frequency-tuning performance of the band-reconfigurable BPF is depicted in Fig. 6.11. In the lower band, the initial CF of the band is 15.11 GHz with a 3dB-bandwidth of 380 MHz, which is realized by h_{via1} = 90 mil and h_{via2} = 30 mil. Then, sweeping the h_{via1} from 90 mil to 115 mil and maintaining h_{via2} = 30 mil, the CFs of the lower band can be tuned from 14.24 GHz to 15.11 GHz, as shown in Fig. 6.11(a). Two overlapped TZs are generated between the bands and their locations can be moved by tuning CFs. In the upper band, the initial CF of the band is 16.68 GHz with a 3dB-bandwidth of 250 MHz, which is realized by h_{via1} = 115 mil and h_{via2} = 30 mil. Then, sweeping the h_{via2} from 30 mil to 80 mil and maintaining h_{via1} = 115 mil, the CFs of the lower band can be tuned from 15.93 GHz to 15.68 GHz, as shown in Fig. 6.11(b). In the single-band state, the initial CF of the band is 15.85 GHz with a 3dB-bandwidth of 570 MHz, which is realized by h_{via1} = 0 mil and h_{via2} = 0 mil. Then, sweeping the h_{via1} and h_{via2} from 0 mil to 90 mil ($h_{via1} = h_{via2}$), the CFs of the lower band can be tuned from 14.89 GHz to 15.85 GHz, as shown in Fig. 6.11(c).

The electric field distribution of each band is given in Fig. 6.12. It can be observed in Fig. 6.12(a) and (b) that the electric field distributions of diagonal mode 1 and diagonal mode 2 are not as

orthogonal as shown in Fig. 6.2, and week couplings between them are inevitably produced which are caused by inductive coupling irises. In Fig. 6.12(c), the electric field distribution of TE_{201} mode is consistent with the field distribution in Fig. 6.2(a).

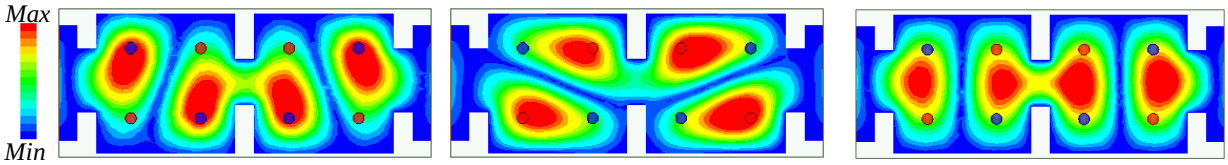

(a) (b) (c)

Figure 6.12 Electric field distribution in the band-reconfigurable BPF. (a) f_o = 15.11 GHz in the dual-band state with h_{via1} = 90 mil and h_{via2} = 30 mil (lower band). (b) f_o = 16.90 GHz in the dual-band state with h_{via1} = 90 mil and h_{via2} = 30 mil (upper band). (c) f_o = 15.76 GHz in the single-band state with h_{via1} = 30 mil and h_{via2} = 30 mil

The photograph of the fabricated prototype is shown in Fig. 6.13. The band-reconfigurable BPF is made on a piece of aluminum 6061-T5 and all the tuning screws are deployed on the top cover. As observed, all the coupling irises are fixed. It is measured with the vector network analyzer Keysight N5224A and two WR62 connectors. The measured frequency-tuning performance is given in Fig. 6.14. In the lower band, the initial CF, 3dB-bandwidth, RL, and insertion loss (IL) of the band are 15.10 GHz, 366 MHz, 19.81 dB, and 0.62 dB, respectively. The CFs of the lower band can be tuned from 13.95 GHz to 15.10 GHz with IL ranging from 0.62 dB to 3.0 dB, as shown in Fig. 6.14(a). In the upper band, the initial CF, 3dB-bandwidth, RL, and insertion loss (IL) of the band are 16.62 GHz, 288 MHz, 20.49 dB, and 0.86 dB, respectively. The CFs of the upper band can be tuned from 15.64 GHz to 16.62 GHz with IL ranging from 0.62 dB to 2.95 dB, as shown in Fig. 6.14(b). In the single-band state, the initial CF, 3dB-bandwidth, RL, and insertion loss (IL) of the band are 15.85 GHz, 547 MHz, 14.44 dB, and 0.27 dB, respectively. The CFs of the single-band can be tuned from 14.73 GHz to 15.85 GHz with IL ranging from 0.27 dB to 1.12 dB, as shown in Fig. 6.14(c). The IL can be improved by silver-plating and the measured frequency-tuning results are consistent with the simulated results.

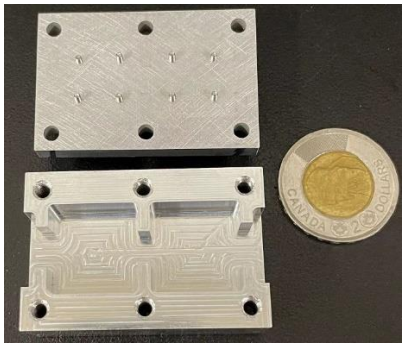

Figure 6.13 Photograph of the fabricated prototype for the band-reconfigurable BPF with the same number of poles in the passband

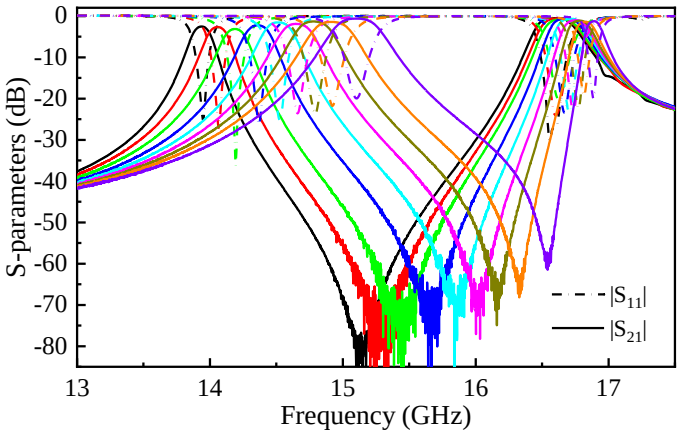

(a)

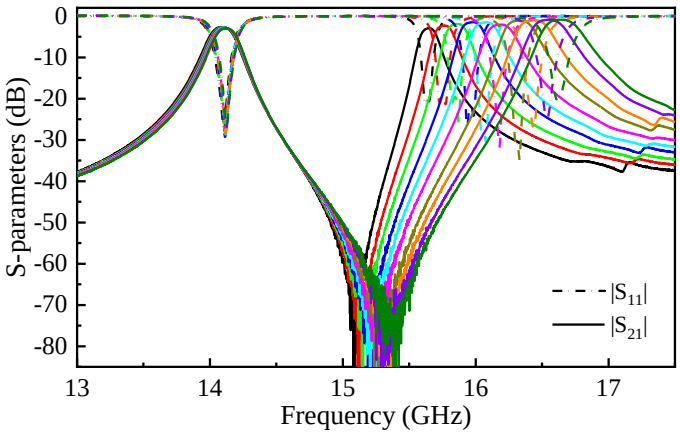

(b)

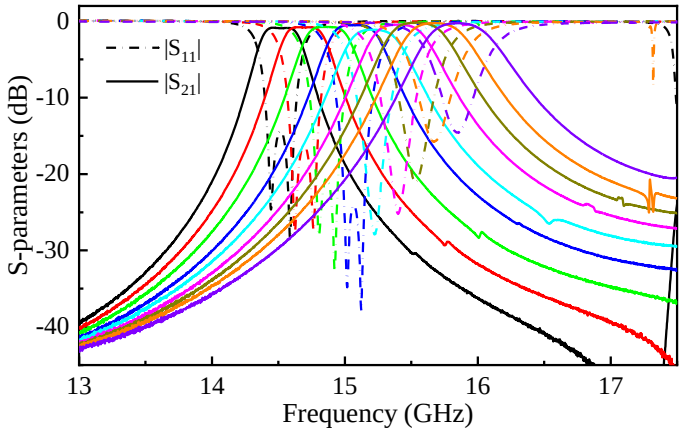

(c)

Figure 6.14 Measured frequency-tuning performance of the band-reconfigurable BPF. (a) Tunable lower band. (b) Tunable upper band. (c) Tunable single-band

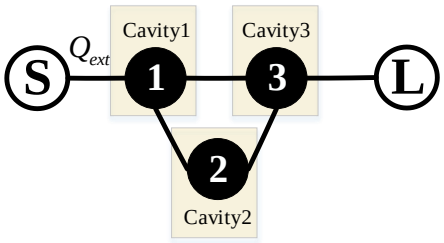

(a)

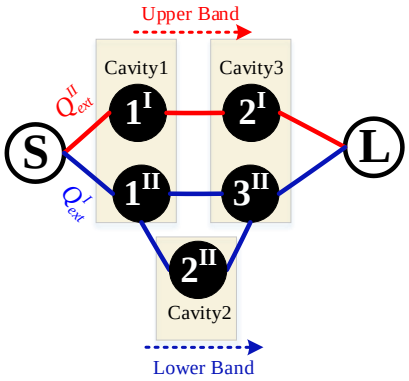

(b)

Figure 6.15 Coupling topology for corresponding model of the band-reconfigurable BPF. (a) Topology for the single-band state implemented by TE_{201} mode in cavity 1, 2, and 3. (b) Topology for the dual-band state implemented by the diagonal modes 1 and 2 in cavities 1 and 3 as well as TE_{201} mode in cavity 2

6.4 Band-reconfigurable BPF with different numbers of poles in the passbands

6.4.1 Coupling topology and geometric configuration

The filter in Section 6.3 has the same number of poles in the passband because each cavity can be switched from one resonator to two resonators. However, it is also possible to have a different number of poles in the passband by cascading these cavities and traditional rectangular waveguide cavities. The other demo of the band-reconfigurable BPF operating at Ku-band is designed, fabricated, and measured. The physical structure of the filter is realized by two square cavities introduced in Section 6.2 and one traditional rectangular waveguide cavity together. If the filter operates in the single-band state, it has 3 poles, and the corresponding topology is given in Fig. 6.15(a). Each cavity is implemented by TE_{201} mode and one TZ can be generated on the lower or upper side of the passband. If the filter operates on the dual-band state, it has 3+2 poles and the corresponding topology is given in Fig. 6.15(b). Cavity 2 is implemented by mode TE_{201} while cavities 1 and 3 have two resonances which are implemented by the diagonal modes 1 and 2. Either the lower passband or the upper band can have 3 poles. As an example, the lower band is set to have 3 poles which are realized by diagonal mode 1 and TE_{201}, and the upper band has 2 poles which are realized by diagonal mode 2.

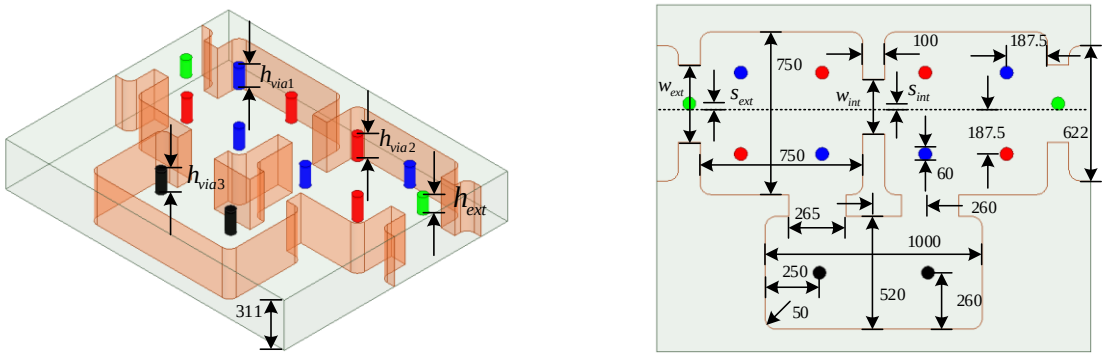

(a) (b)

Figure 6.16 The electromagnetic model of the band-reconfigurable BPF with different numbers of poles in the passbands. (a) 3-D view. (b) Top view

The electromagnetic model of the filter is depicted in Fig. 6.16. As seen in Fig. 6.16(a), the pair of black tuning screws are set to tune the resonant frequency of mode TE_{201} in cavity 2 and the corresponding depth is defined by h_{via3}. The green tuning screws are set to control the physical external coupling strength and the corresponding depth is defined by h_{ext}. As seen in Fig. 6.16(a) and (b), other parameters, such as h_{via1} s_{int}, and w_{int}, are the same as the definition introduced in Section 6.3.

6.4.2 Specifications, coupling matrices, and coupling designs

As a demonstration, the initial specifications of the filter design require the RL of 20 dB in each band, the CFs of 14.80 GHz and 16.70 GHz at lower and upper bands, respectively. In the lower band, it has 3 poles and the location of TZ is -1.8j. The 3dB-bandwidths are 390 MHz and 340 MHz at lower and upper bands, respectively.

The normalized coupling matrix for the upper band is given in (2) and the lower band is synthesized using the Chebyshev filtering function [14], which is given by

$$M = \begin{bmatrix} 0 & 1.0838 & 0 & 0 & 0 \\ 1.0838 & -0.1517 & 0.8755 & 0.6424 & 0 \\ 0 & 0.8755 & 0.6066 & -0.8755 & 0 \\ 0 & 0.6424 & -0.8755 & -0.1517 & 1.0838 \\ 0 & 0 & 0 & 1.0838 & 0 \end{bmatrix}. \tag{6.5}$$

The design processing from the normalized internal/external coupling coefficients to the corresponding physical internal/external coupling coefficients is the same as the method introduced in Section 6.3. The only difference is that the mode TE_{201} in cavity 2 maintains the same operating mode even though the band of the filter is reconfigured. The potential problem is that the couplings are not matched to deteriorate the response of the filter. There are two approaches to keep the same RL level in each passband. The first method is that change the value of coupling coefficients M_{12} and M_{23} (M_{12} = -M_{23}). Meanwhile, the position of TZ will be moved. The second method is that control the external coupling coefficient to achieve a good matching. Considering frequency-tuning of the band will cause mismatch and controlling of physical external coupling coefficient can compensate for mismatch, therefore, the second method is adopted in this example.

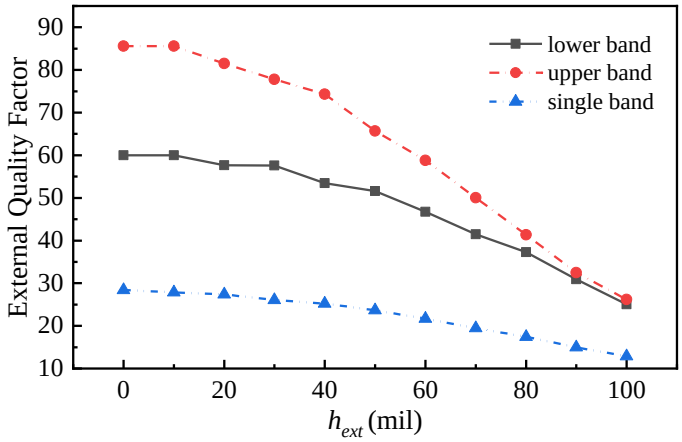

Figure 6.17 Physical external quality factors for each band by tuning h_{ext} with w_{ext} = 355 mil: Dual-band state with h_{via1} = 100 mil and h_{via2} = 0 mil; single-band state with h_{via1} = 0 mil and h_{via2} = 0 mil

Maintaining the w_{ext} = 355 mil and sweeping h_{ext} from 0 mil to 100 mil, the physical external quality factor of each band is shown in Fig. 6.17. In the dual-band state (h_{via1} = 100 mil and h_{via2} = 0 mil), the physical external quality factor of the lower band can be changed from 25.1 to 60.0 and the physical external quality factor of the upper band can be changed from 26.2 to 85.6. In the single-band state (h_{via1} = 0 mil and h_{via2} = 0 mil), the qualify factor can be changed from 12.9 to 28.4. It can be observed that the physical external quality factor of each band will be decreased if the value of h_{ext} is increased. In addition to adjusting the value of w_{ext}, the value of s_{ext}, and selecting the resonant frequency in the single-band state (explained in Section 6.3), the value of h_{ext} provides an additional dynamic range to match the physical external coupling coefficients needed in each passband.

6.4.3 Simulation, fabrication, and measurement

The physical structure of the band-reconfigurable BPF shown in Fig. 6.16 can be designed accordingly. After final optimization, the values of w_{int}, s_{int}, w_{ext}, and s_{ext} are 250 mil, -30 mil, 355 mil, and -45 mil, respectively. The simulated frequency-tuning performance of the filter is depicted in Fig. 6.18. In the lower band, the initial CF of the band is 14.82 GHz with 3dB-bandwidth of 390 MHz, which is realized by h_{via1} = 84 mil, h_{via2} = 0 mil, h_{via3} = 78 mil, and h_{ext} = 75 mil. The CFs of

the lower band can be tuned from 13.97 GHz to 14.82 GHz, as shown in Fig. 6.18(a). In the upper band, the initial CF of the band is 16.72 GHz with 3dB-bandwidth of 340 MHz, which is realized by h_{via1} = 100 mil, h_{via2} = 10 mil, h_{via3} = 89 mil, and h_{ext} = 70 mil. The CFs of the upper band can be tuned from 15.99 GHz to 16.72 GHz, as shown in Fig. 6.18(b). In the single-band state, the initial CF of the band is 15.56 GHz with 3dB-bandwidth of 490 MHz, which is realized by h_{via1} = 24 mil, h_{via2} = 45 mil, h_{via3} = 35 mil, and h_{ext} = 0 mil. The CFs of the band can be tuned from 14.47 GHz to 15.56 GHz, as shown in Fig. 6.18(c).

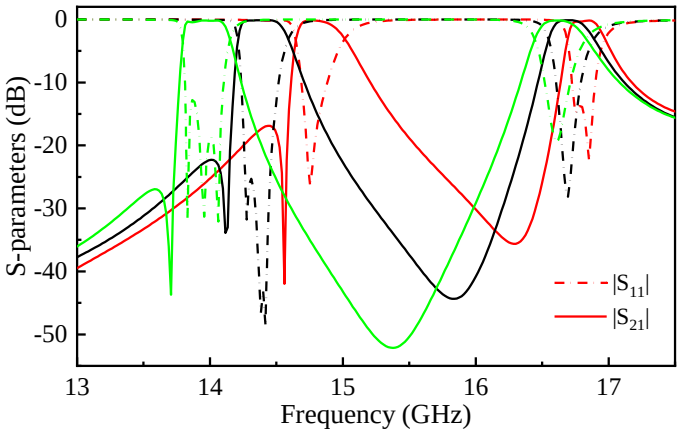

(a)

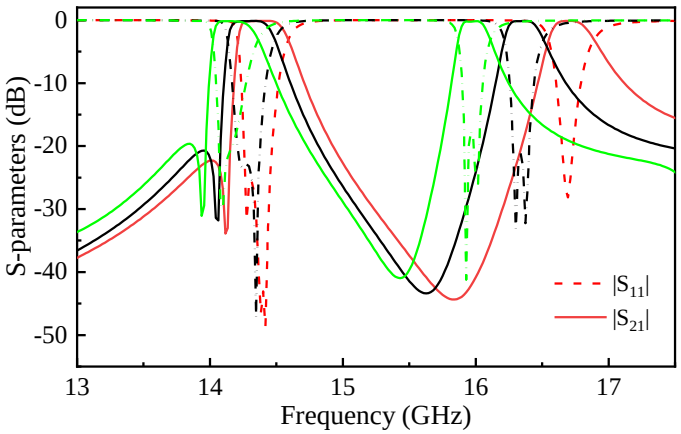

(b)

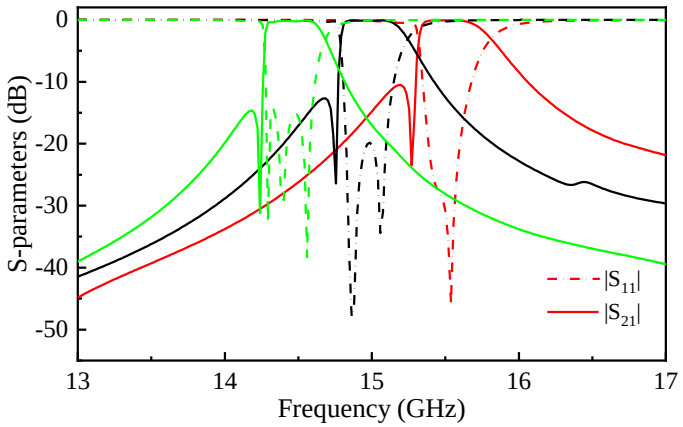

(c)

Figure 6.18 Simulated frequency-tuning performance of the band-reconfigurable BPF with different number of poles in the passband. (a) Tunable lower band. (b) Tunable upper band. (c) Tunable single-band

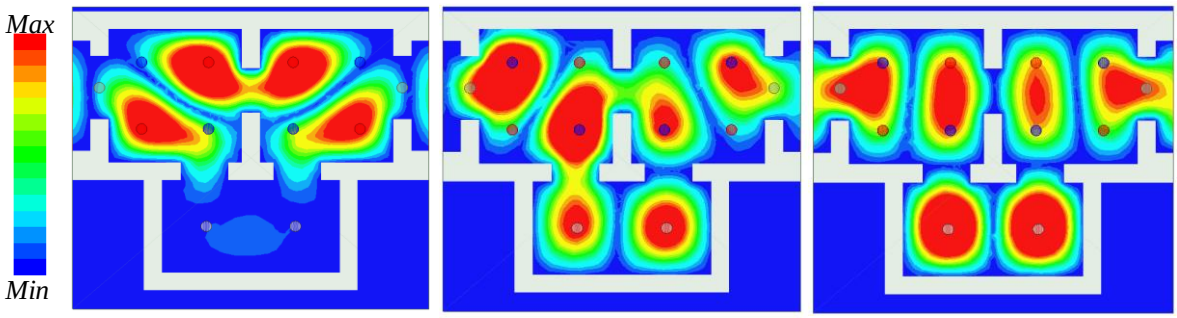

(a) (b) (c)

Figure 6.19 Electric field distributions in the band-reconfigurable BPF. (a) f_o = 14.37 GHz in the dual-band state with h_{via1} = 100 mil, h_{via2} = 10 mil, and h_{via3} = 89 mil (lower band). (b) f_o = 16.70 GHz in the dual-band state with h_{via1} = 89 mil, h_{via2} = 30 mil, and h_{via3} = 90 mil (upper band). (c) f_o = 15.00 GHz in the single-band state with h_{via1} = 80 mil, h_{via2} = 80 mil, and h_{via3} = 73 mil

The electric field distribution of each band is given in Fig. 6.19. In the lower band, the diagonal mode 1 in cavity 1 is coupled to the TE_{201} mode in cavity 2 and the diagonal mode 1 in cavity 3,

respectively. Also, the modes in cavities 2 and 3 are coupled, as shown in Fig. 6.19(a). In the upper band, only the diagonal mode 2 in cavity 1 is coupled to the diagonal mode 2 in cavity 3, as shown in Fig. 6.19(b). In the single band state, mode TE_{201} in cavity 1, cavity 2, and cavity 3 are coupled with each other, as shown in Fig. 6.19(c).

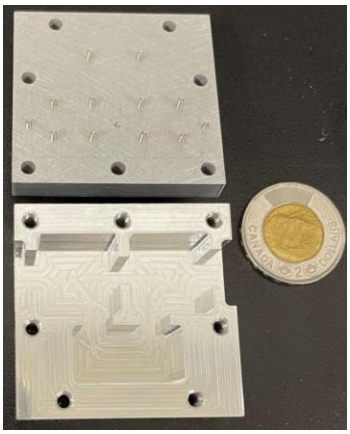

Figure 6.20 Photograph of the fabricated prototype for the band-reconfigurable BPF with the different number of poles in the passband

The photograph of the fabricated prototype for the band-reconfigurable BPF with a different number of poles in the passband is shown in Fig. 6.20. As observed, all the internal coupling irises are fixed, and the external coupling irises have tuning screws to adjust coupling strength. The measurement method is the same as used in Section 6.3. The measured frequency-tuning performance is depicted in Fig. 6.21. In the lower band, the initial CF, 3dB-bandwidth, RL, and insertion loss (IL) of the band are 14.81 GHz, 370 MHz, 28.72 dB, and 1.94 dB, respectively. The CFs of the lower band can be tuned from 13.84 GHz to 14.81 GHz with IL ranging from 1.49 dB to 3.35 dB, as shown in Fig. 6.21(a). In the upper band, the initial CF, 3dB-bandwidth, RL, and insertion loss (IL) of the band are 16.69 GHz, 430 MHz, 24.00 dB, and 2.27 dB, respectively. The CFs of the upper band can be tuned from 15.85 GHz to 16.69 GHz with IL ranging from 2.27 dB to 4.75 dB, as shown in Fig. 6.21(b). In the single band state, the initial CF, 3dB-bandwidth, RL, and insertion loss (IL) of the band are 15.55 GHz, 510 MHz, 17.11 dB, and 0.84 dB, respectively. The CFs of the single-band can be tuned from 14.17 GHz to 15.55 GHz with IL ranging from 0.84 dB to 2.61 dB, as shown in

Fig. 6.21(c). The peaks beyond the passband in Fig. 6.19(c) result from the interference modes excited by tuning screws, which can be modified by silver-plating.

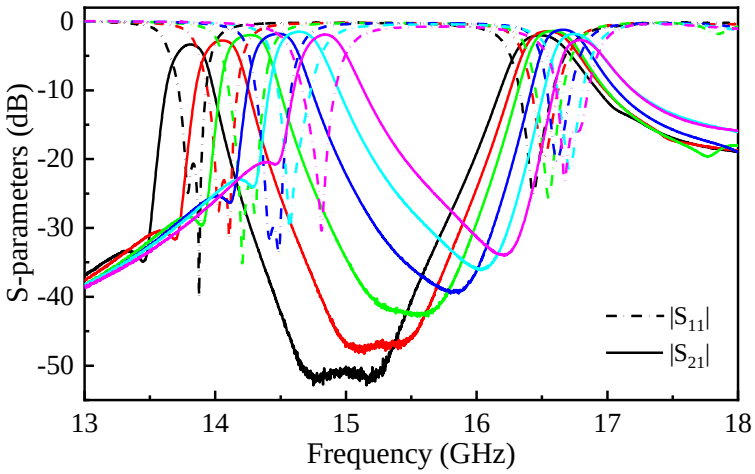

(a)

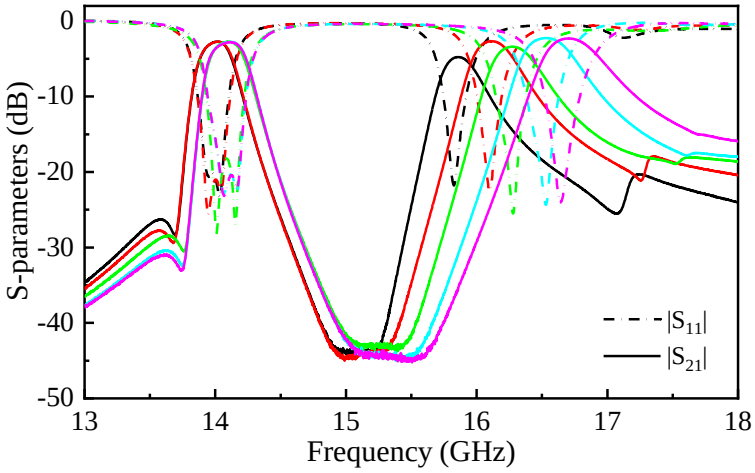

(b)

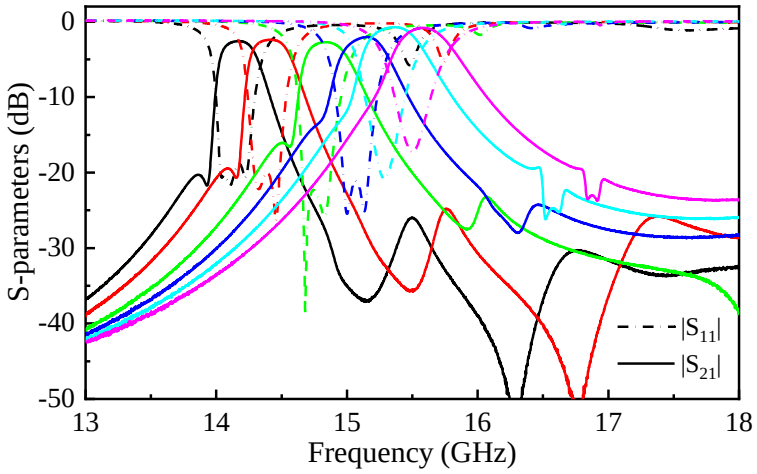

(c)

Figure 6.21 Measured frequency-tuning performance of the band-reconfigurable BPF with different number of poles in the passband. (a) Tunable lower band. (b) Tunable upper band. (c) Tunable single-band

Table 6.1 lists the comparisons with other related state-of-the-art multi-band/band-reconfigurable BPF designs. It can be observed that in our designs not only each band can be frequency-tuned, but also the number of poles in each band can be flexibly controlled.

6.5 Conclusion

The approach to the development of band-reconfigurable BPFs using the mode-switching concept is presented in this chapter. The operating modes can be switched between the TE_{201} and corresponding diagonal modes using tuning elements in the same square cavity. Moreover, two demos have been designed, fabricated, and measured in Ku-band. Regardless of single- or dual-band states, not only each band can be frequency-tuned, but also the number of poles in each band can be flexibly controlled. The measured results exhibit both band-reconfigurable and frequency-tuning capability, which shows great potential in the development of multi-standard and multi-function communication and sensing systems.

Table 6.1 Comparisons with some other related state-of-the-art designs

Ref.	Type	State	Band	f_o (GHz)	FBW@ f_o(%)	F-T Range (GHz)	F-T Pct. (%)	Order	No. of TZs
[156]	ML	1	Lower/ Upper	0.86/ 1.33	4.50/ 10.50	0.79-0.86/ 1.20-1.33	8.48/ 10.28	3/3	1/1
[157]	ML+WG	1	Lower/ Upper	8.22/ 10.56	N/A/ N/A	7.51-8.22/ 9.34-10.56	9.00/ 12.30	2/2	0/2
[158]	SIW	1	Lower/ Upper	1.74/ 3.65	8.97/ 15.15	1.16-1.74/ 2.42-3.65	40.00/ 40.53	2/2	0/0
[162]	ML	1	Lower/ Upper	0.90/ 1.07	9.78/ 8.60	0.69-0.90/ 0.85-1.07	26.4/ 22.92	2/2	0/0+2LU
		2	Single	1.08	14.63	0.75-1.08	36.07	4	1
[48]	SIW	1	Lower/ Upper	4.63/ 7.02	N/A/ N/A	N/A	N/A	2/4	0/0
		2	Lower	4.60	N/A	N/A	N/A	2	0
		3	Upper	7.19	N/A	N/A	N/A	4	0
		4	No band	N/A	N/A	N/A	N/A	0	N/A
[163]	SIW	1	Lower/ Upper	3.00/9.00	5.10/ 3.40	2.00-3.00/ 8.00-9.00	40.00/ 11.76	2/2	0/0
		2	Lower	3.00	5.10	2.00-3.00	40.00	2	0
		3	Upper	9.00	3.40	8.00-9.00	11.76	2	0
This work	**WG design1**	**1**	**Lower/ Upper**	**15.10/ 16.62**	**2.42/ 1.73**	**13.95-15.10/ 15.64-16.62**	**7.92/ 6.08**	**2/2**	**0/0+2LU**
		2	**Single**	**15.85**	**3.45**	**14.73-15.85**	**7.32**	**2**	**0**
	WG design2	**1**	**Lower/ Upper**	**14.81/ 16.69**	**2.50/ 2.58**	**13.84-14.81/ 15.85-16.69**	**6.77/ 5.16**	**3/2**	**1/0**
		2	**Single**	**15.55**	**3.28**	**14.17-15.55**	**9.29**	**3**	**1**

CHAPTER 7 VOLUME CONTROLLABLE RESONATOR FOR THZ APPLICATIONS

In this chapter, a volume controllable resonator for THz applications is presented. The resonator contains a cavity with a metal post in the middle of the cavity. The proposed resonator is made of a larger resonant cavity compared to that of the fundamental mode while it maintains an unloaded quality factor similar to that of the fundamental mode. The volume of the resonator is controllable at the same resonant frequency as that of the conventional counterpart by changing the diameter of a metal post in the middle of the cavity. Thanks to the larger space of the resonator, it has the potential to overcome the processing precision issue, to reduce the fabrication difficulty, and to bring up the possibility of resonant mode in the future. For experimental verification, a third-order THz bandpass filter has been designed, fabricated, and measured. The resulting resonant cavity exhibits a size almost twice that of fundamental mode.

7.1 Introduction

Judging from the fundamental wavelength effects, the lower the operating frequency is, the larger the resonant cavity of the fundamental mode becomes. To avoid the size- and weight-related disadvantages of communication systems at lower frequencies, there are many technologies of resonance have been proposed, such as coaxial cavity [33, 149, 167], dielectric cavity [30, 135, 168, 169], *etc*. By implementing these types of cavities, the volume of resonator will be smaller, and the weight of system will be lightened, making commercialization more viable. At the same time, the quality factor of such resonant cavities does not drop in spite of a volume reduction, which is crucial for insertion loss.

At higher frequencies, especially for THz bands, that would be the other scenario because the higher the frequency is, the smaller the resonant cavity of the fundamental mode becomes. Therefore, those techniques applied to low frequencies are no longer should be avoided at high frequencies because the volume is too small to be appreciable. In fact, a new scheme that allows an increasing volume of resonator while maintaining its quality factor close to that of the fundamental mode resonator, should be developed and studied for THz filter applications.

There are three potential ways to increase the effective volume of a resonator, including controlling the length-to-width (L/W) ratio of a rectangular cavity, applying higher-order modes, and deploying an entirely new mode. First, in the rectangular cavity, the resonant frequency of the fundamental mode can be calculated by the standard equation [151]. It can be concluded that the volume of the cavity is smallest if the L/W ratio is equal to 1. In other words, the volume of the cavity becomes larger as the L/W ratio becomes larger. However, the limitation in applications is that larger aspect ratios can also excite potential higher-order modes close to and detrimental to the passband, which depend on the internal/external coupling positions. Second, the higher-order modes lead to a larger space compared to the fundamental mode. However, there are usually more than one higher-order modes that can be excited, and their resonant frequencies are very close to each other. It is difficult to excite only one higher-order mode with suitable coupling irises, which challenges the level of out-of-band rejections. Third, volume controllable resonant modes can be considered, which consist of an empty cavity and a metal post located in the centre of a cavity. Generally, the larger the cavity is, the lower the resonant frequency becomes. Instead, the larger diameter of the post is, the higher the resonant frequency becomes. Therefore, the resulting size of the cavity at the same frequency is controlled by the size of the cavity and the diameter of the post together. The details are given in Section 7.2.

In this work, a third-order THz bandpass filter using the proposed mode is designed, fabricated, and measured. Compared to the fundamental mode resonator operating at the same frequency, the designed resonant cavity can be made almost twice larger.

The rest of the chapter is organized as follows. The potential methods for THz filter design and applications are introduced in Section 7.2, especially, the volume controllable resonant modes are investigated in detail. Then, a third-order THz bandpass filter is designed, fabricated, and measured in Section 7.3. Finally, the conclusion is drawn in Section 7.4.

7.2 Potential methods for THz filter applications

7.2.1 Larger L/W ratio of cavity for the fundamental mode

In this section, the fundamental mode in a rectangular cavity will be examined. The initial resonant frequency of the TE_{110} mode can be calculated using the following equation [151]

$$f_{mn} = \frac{c}{2\sqrt{\mu_r \varepsilon_r}} \sqrt{\left(\frac{m}{W}\right)^2 + \left(\frac{n}{L}\right)^2} \ . \tag{7.1}$$

where c is the velocity of light in a vacuum, μ_r and ε_r are the relative permeability and permittivity of a substrate, respectively, L and W is the length and width of a rectangular waveguide cavity, respectively. m and n are the numbers of variations in x- and y-directions, respectively.

Substituting m = 1 and n =1 into 7.1, let

$$f_{ab} = \frac{4 f_{11}^2 \mu_r \varepsilon_r}{c^2} = \left(\frac{1}{W}\right)^2 + \left(\frac{1}{L}\right)^2 = \frac{W^2 + L^2}{W^2 L^2} \ . \tag{7.2}$$

Since $W^2 + L^2 \geq 2WL$, Substituting it into 7.2,

$$f_{ab} = \frac{4 f_{11}^2 \mu_r \varepsilon_r}{c^2} \geq \frac{2}{WL} . \tag{7.3}$$

Considering the same resonant frequency, f_{ab} is a constant positive value. Therefore,

$$S = WL \geq \frac{2}{f_{ab}} . \tag{7.4}$$

where S is the volume of the resonant cavity. It has the minimum value when $W = L$. It can be concluded that the volume of the cavity is smallest if L/W ratio is equal to 1 when operating at the same resonant frequency. In other words, the volume of the cavity can be made bigger with a larger L/W ratio.

From the above mathematical derivation, the larger the L/W ratio of the cavity is, the larger the cavity volume is. However, in practical applications, a very larger L/W ratio is not attractive. There are two main aspects to be considered. First, whether the fundamental mode can be excited and whether the internal/external physical coupling coefficients can be satisfied under the corresponding conditions. For example, if the required width of an external coupling iris is wider than the width of a connector at the corresponding frequency, then the obtained physical external coupling coefficient cannot satisfy the design requirements. Second, if the cavity owns a larger L/W ratio, not only the fundamental mode but also higher-order modes will be excited, which

would degrade the out-of-band rejection level. The higher-order modes out of the passband are not expected in the design and how to suppress these modes becomes an additional task.

In conclusion, a rectangular cavity with a larger L/W ratio can increase the volume when operating at the same resonant frequency of the fundamental mode. However, the generated higher-order modes out of passband should be handled in an adequate manner.

7.2.2 Volume controllable resonant modes

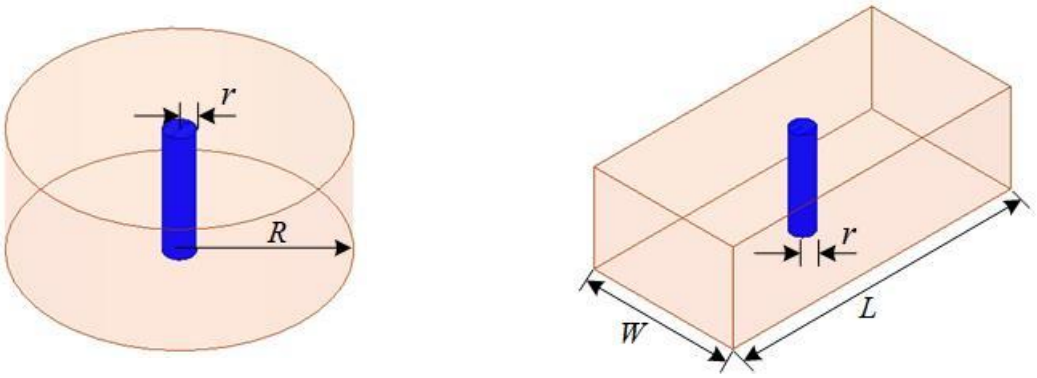

(a) (b)

Figure 7.1 Volume controllable resonant modes. (a) Cylindrical cavity with a metal post in the middle of the cavity. (b) Rectangular cavity with a metal post in the middle of the cavity

Two types of volume controllable resonant modes are investigated in this section. The corresponding cavities contain a cylindrical cavity with a metal post and a rectangular cavity with a metal post in the middle of the cavity, as shown in Fig. 7.1. The length of post is equal to the height of the cavity. Therefore, the metal post connects the top and bottom of the cavity. The details are introduced as follows.

7.2.2.1 Circular mode

As shown in Fig. 7.1(a), the radius of the cylindrical cavity is defined by *R*. The post in the middle of the cavity is connected to both the top and bottom layers. The radius of the post is defined by *r*. The electromagnetic modeling is made by an eigenmode analysis in the ANSYS High Frequency

Structure Simulator (HFSS). The electric field distribution of the mode of interest is shown in Fig. 7.2.

Then, the resonant frequency of the mode of interest is concerned. The relationship between *R* and the corresponding frequency with various values of *r* is depicted in Fig. 7.3. As can be seen, under the same value of *R*, the corresponding resonant frequency becomes higher with a larger value of *r*. In other words, a larger radius of the metal post is set to hold a higher resonant frequency in the same cavity. If the required resonant frequency is the same, a larger radius of the metal post also needs a larger cylindrical cavity, which is meaningful for higher frequency bands. For example, the fundamental mode requires a radius of 30 mil at 150 GHz while the proposed mode can extend to the radius of 50 mil at the same frequency if *r* = 9mil.

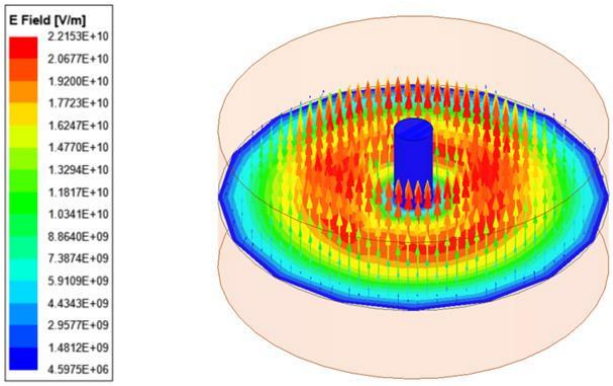

Figure 7.2 Electric field distribution of the mode of interest in a cylindrical cavity

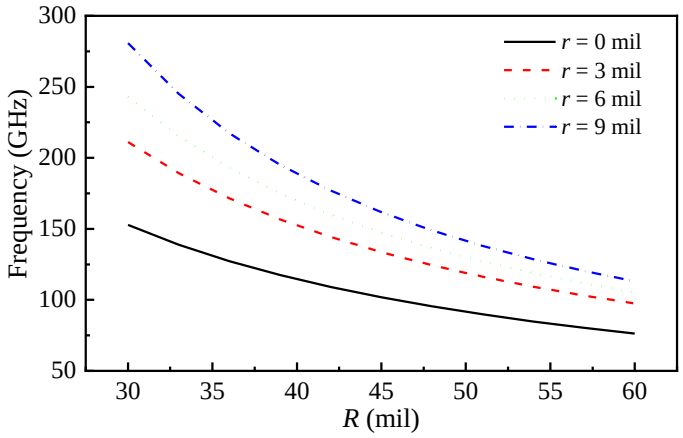

Figure 7.3 Relationship between the resonant frequency of the desired mode in the cylindrical cavity and *R* with different *r*

The unloaded quality factors Q_us of the wanted modes in the cylindrical cavity are given in Fig. 7.4. First, the Q_u of the fundamental mode is higher than that of the proposed mode. Second, the Q_u of the fundamental mode decreases if R increases. However, the Q_u of the proposed mode does not decrease or even increase a little bit if R increases. Third, the Q_u of the proposed mode would be increased if r increases.

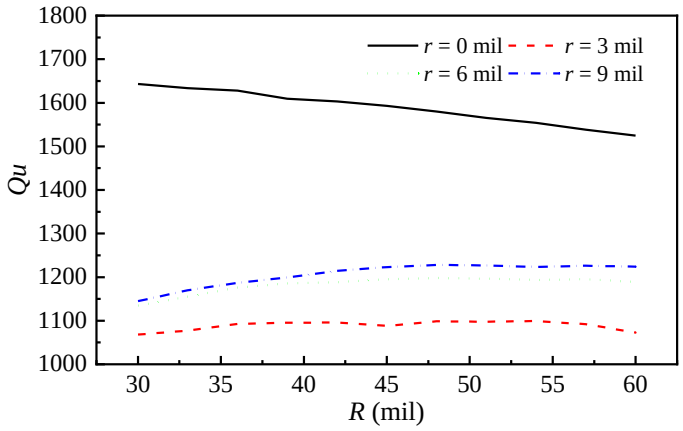

Figure 7.4 Unloaded quality factors Q_us of the desired mode in the cylindrical cavity. Finite conductivity: aluminum

7.2.2.2 Rectangular mode

As shown in Fig. 7.1(b), the length and width of the cavity are defined by L and W, respectively. Again, the post in the middle of the cavity is connected to both top and bottom layers. The radius of the post is defined by r. This structure is simulated in ANSYS HFSS and the corresponding electric field distribution is shown in Fig. 7.5. As shown in the figure, two electric field peaks are in phase.

Since the length-to-width ratio of a rectangular cavity has been discussed in Section 7.2.1, the resonant frequency of the mode is investigated by setting $L/W = 2$ for demonstration. The relationship between L and the corresponding frequency with various values of r is depicted in Fig. 7.6. As can be seen, with the same value of L, the corresponding resonant frequency becomes higher for a larger value of r. In other words, a larger radius of the metal post brings up a higher resonant frequency in the same cavity. Obviously, it suggests that the resonant frequency of the

fundamental mode is lower than that of the proposed mode for the same L. If the required resonant frequency is the same, a larger radius of the metal post also needs a larger rectangular cavity, which is an advantage in THz frequency bands.

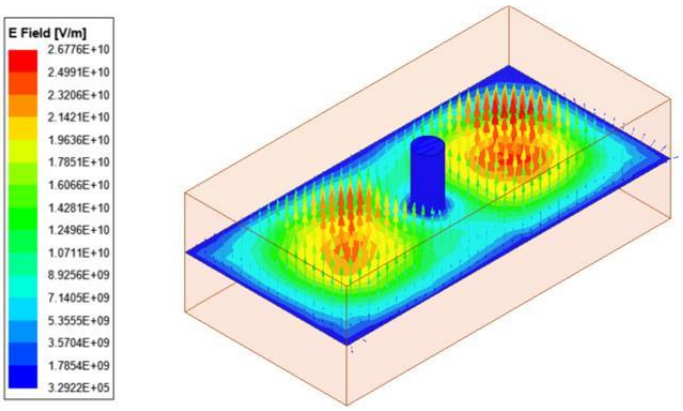

Figure 7.5 Electric field distribution of the wanted mode in a rectangular cavity

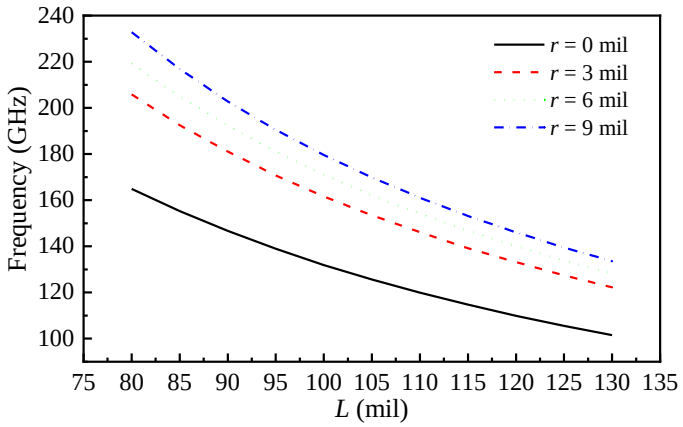

Figure 7.6 Relationship between the resonant frequency of the wanted mode in the rectangular cavity and L with different r

The unloaded quality factors Q_us of the desired modes in the rectangular cavity are given in Fig. 7.7. First, the Q_u of the fundamental mode is higher than that of the proposed mode. Second, the Q_u of the proposed mode would be increased if r increases. Third, compared to the Q_us of the mode in the cylindrical cavity in Fig. 7.4, the unloaded quality factor of the mode in the rectangular cavity

is much closer to that of the fundamental mode in the same size cavity. For instance, if r = 9 mil, the Q_u of the corresponding mode shows a close level to that of the fundamental mode.

In the rectangular cavity, the L/W ratio provides an additional dimension for filter design. By changing the ratio, the proposed mode can be far away from other higher-order modes, or it can work with them together. Therefore, it creates not only a large cavity which presents a good potential for more possibilities (i.e., tunable resonator), but also a flexible design with other modes together.

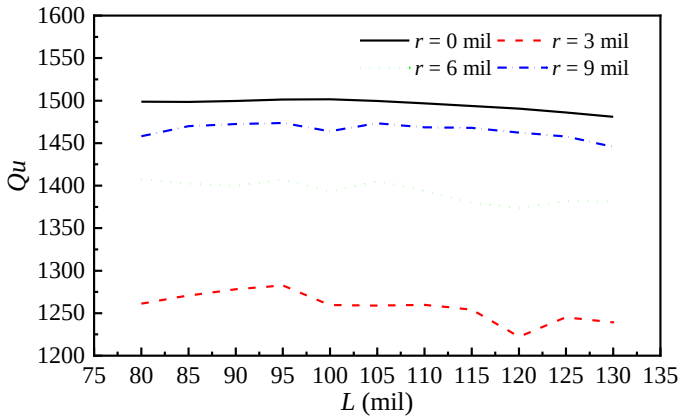

Figure 7.7 Unloaded quality factors Q_us of the desired modes in the rectangular cavity. Finite conductivity: aluminum

It can be concluded that no matter in the cylindrical or rectangular cavity, a larger radius of the metal post leads to a higher resonant frequency as well as a higher Q_u. However, a larger size cavity always brings up a lower resonant frequency. As can be seen in Fig. 7.3 and Fig.7.6, the final size of the cavity at a specific frequency has certain limitations and will not be made arbitrary. On the other hand, the standard connector should be considered in the development as well. Otherwise, the required physical coupling irises of a larger sized cavity may be wider than the size of the connector.

7.3 A third-order THz bandpass filter

As a demonstration and validation, a third-order waveguide THz bandpass filter is synthesized and designed with the following specifications: in-band return loss (RL) of 20 dB, center frequency of

152.5 GHz with 3-dB bandwidth of 5.5 GHz. A normalized coupling matrix can be synthesized using a Chebyshev filtering function in [14]

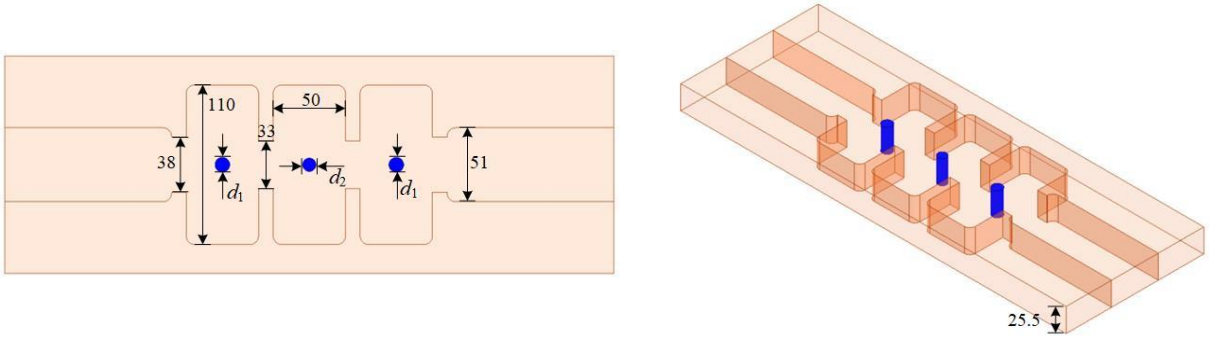

(a) (b)

Figure 7.8 Electromagnetic model of the demonstrated third-order THz bandpass filter using the proposed mode in a rectangular cavity. d_1 = 10.2 mil. d_2 = 9.2 mil. Unit: mil

$$M = \begin{bmatrix} 0 & 1.0825 & 0 & 0 & 0 \\ 1.0825 & 0 & 1.0303 & 0 & 0 \\ 0 & 1.0303 & 0 & 1.0303 & 0 \\ 0 & 0 & 1.0303 & 0 & 1.0825 \\ 0 & 0 & 0 & 1.0825 & 0 \end{bmatrix}. \quad (7.5)$$

The desired mode in the rectangular cavity is selected in this case. A WR-5 standard waveguide-based THz bandpass filter is modelled and simulated in ANSYS HFSS. The electromagnetic model of the filter is shown in Fig. 7.8. There are three rectangular cavities cascaded of the same size. The adjustment of resonant frequencies is mainly controlled by the diameter of the post in the middle of the cavity. The diameters of posts in cavities 1 and 3 are defined by d_1 while the diameter of the post in cavity 2 (middle) is defined by d_2. After optimization, the value of d_1 and d_2 is 10.2 mil and 9.2 mil, respectively. All the other specifications are directly marked in Fig. 7.8.

Figure 7.9 Photograph of the fabricated prototype

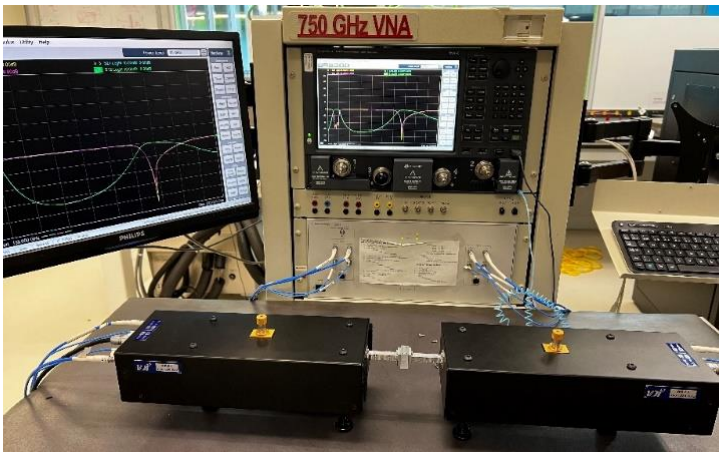

Figure 7.10 Testing platform for the THz bandpass filter

The photograph of the fabricated experimental prototype is shown in Fig. 7.9. The filter is made on a piece of aluminum 6061-T5. It is measured with a vector network analyzer and two WR-5 connectors, as shown in Fig. 7.10.

Both simulation and measurement results are given in Fig. 7.11. First, the measured center frequency of the passband shifts to a lower frequency side compared to the simulated result because the fabricated cavity size will be a little larger than the designed one caused of fabrication tolerance, such as vibration. Second, the return loss level deteriorates significantly. A potential reason is that

the diameter of the posts changing is very sensitive to the responses of the filter, which is verified in ANSYS HFSS. The fabrication tolerance analysis contains two parts, including the cavity size analysis and the post size analysis. In the cavity size analysis, the value of cavity length, internal coupling iris, and external coupling iris is supposed to be 110±0.4 mil, 33±0.4 mil, and 38±0.4 mil, respectively. The simulated results are depicted in Fig. 12(a). As can be seen, even if three parameters are swept, the $|S_{11}|$ of the responses is better than 15 dB. In the post size analysis, the diameter of posts d_1 and d_2 are supposed to be 10.2±0.4 mil and 9.2±0.4 mil, respectively. The simulated results are given in Fig. 12(b). The responses of $|S_{11}|$ are batter than 5 dB. Compared to the cavity size analysis, the post size is much more sensitive. The post-design will be regarded as a topic to be overcome in the future.

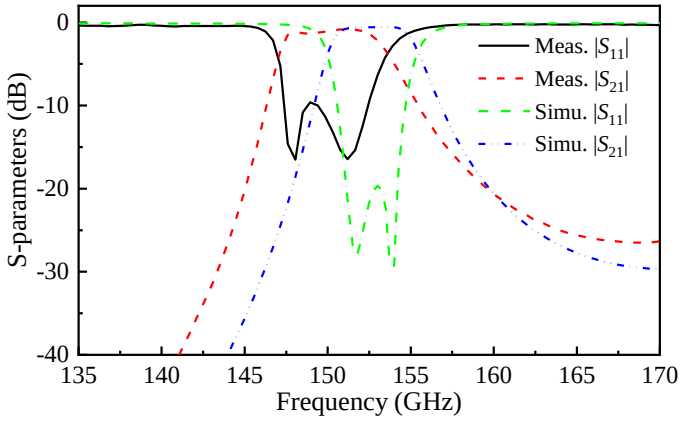

Figure 7.11 Simulated and measured results of the prototyped THz bandpass filter

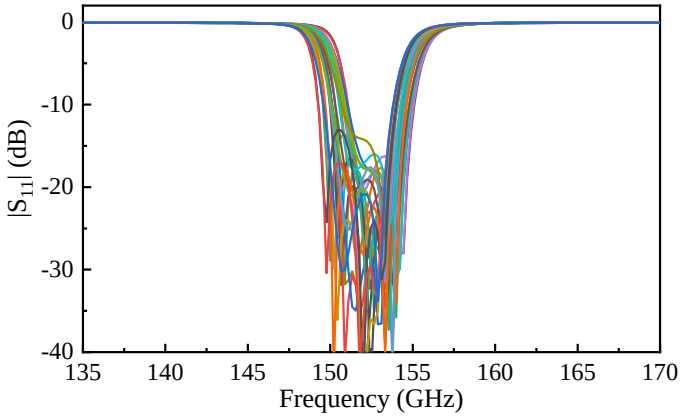

(a)

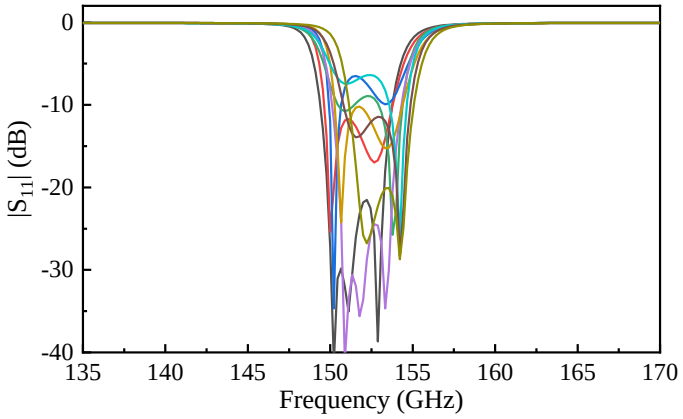

(b)

Figure 7.12 Tolerance analysis of the THz bandpass filter. (a) Sweeping the length of cavity, internal coupling iris and external coupling iris. (b) Sweeping the diameter of posts d_1 and d_2

7.4 Conclusion

In this chapter, a volume controllable resonator for THz filter design and applications is presented. The volume of the resonator can be made controllable at the same resonant frequency by changing the diameter of a loaded post in the middle of the cavity. For experimental verification, a third-order THz bandpass filter has been designed, fabricated, and measured. The resonant cavity can be realized with a size almost twice that of the fundamental mode resonator. It is found that the diameter of the post is still sensitive regarding the responses of the filter, and it will be focused as a future work.

CHAPTER 8 CONCLUSION

8.1 Conclusion

This thesis research has formulated and presented several methodologies for waveguide-based tunable and reconfigurable bandpass filter design and developments. In this work, a set of theoretical derivations have been developed and explored, as well as numerous physical realizations for different tunable and reconfigurable filters have been studied and demonstrated. Tunable bandpass filters with reconfigurable transmission zeros (TZs) on the complex plane were introduced in Chapters 3 and Chapter 4. Then, tunable bandpass filters with a mode-switching concept were investigated, mainly including a class of widely frequency-tuning range filters with constant bandwidth in Chapter 5, and a class of band-reconfigurable tunable filters in Chapter 6. In Chapter 7, a volume controllable resonator for THz filter applications was presented and discussed.

In Chapter 3, a pair of symmetric TZs that can be reconfigured on the complex plane has been investigated. The frequency-tuning performance and the reconfigurable responses can be achieved simultaneously by only tuning resonant frequencies. Therefore, the frequency-tuning performance and reconfigurable performance are considered and controlled together to decrease the number of tuning elements. The physical realization for internal coupling is inductive coupling iris, which is simple, robust, and stable. During the process, a theoretical derivation from the transversal topology to the needed topology is implemented by coupling matrix rotations. Moreover, to achieve the required performance, a number of optimization steps are described in detail, too.

In Chapter 4, an asymmetric TZ that can be made reconfigurable between the positive and negative value on the imaginary axis has been investigated. The frequency-dependent coupling (FDC) technique and the box-like topology are chosen to physically realize tunable and reconfigurable bandpass filters. The FDC technique-based inline bandpass filter can decrease the number of couplings in each node to make the matching network more stable. Meanwhile, the FDC physical structure itself can generate one TZ and the location of the TZ can be tuned by the FDC structure. The advantage of the FDC technique is that the physical inline structure of the filter is simple and the physical structure of FDC coupling is also made simple. The location of TZ can be shifted for a wide frequency tuning range. In the box-like topology, the asymmetric TZ can be controlled with

the frequency-tuning performance together by only tuning resonant frequencies. Meanwhile, the return loss, no matter the location of TZs on the lower or upper side of the passband, maintains the same level during reconfiguring. The advantage of the box-like topology is that the number of tuning elements is decreased, and the frequency-tuning performance as well as reconfigurable responses can be obtained at the same time.

In Chapter 5, how to design a widely frequency-tuning range of a tunable bandpass filter with constant bandwidth is investigated. There are four aspects that restrict the global tuning range, such as frequency tuning range of resonators, internal coupling, external coupling, and bandwidth. In the cavity-based resonator, the final (global) tuning range can be regarded as combining more than one sub-tuning range using a mode-switching concept. If so, the restriction condition of the final tuning range is transformed to a sub-restriction condition in the corresponding separate tuning range, which is much easier for physical realization. In the cavity structure, a tuning element is deployed in the centre of the cavity for perturbing the fundamental mode. However, if the tuning element connects the top and bottom layers of the cavity, the fundamental mode is switched to a common mode, which is resonating at a higher frequency. After adding tuning elements for the common mode, a lower tuning band from the fundamental mode and a higher tuning band from the common mode can be combined for a widely frequency-tuning range using a suitable length-to-width ratio of the cavity. Meanwhile, there is no interference of higher-order modes in the entire tuning range.

In Chapter 6, band-reconfigurable bandpass filters with a cavity-based structure are investigated. The higher-order mode TE_{210} is chosen as the operating mode, which is perturbed by two pairs of tuning elements. Under the same physical cavity, if the two pairs of tuning elements have different depths in the cavity, the TE_{210} mode may be switched to two diagonal modes and one TZ is generated between diagonal modes. Therefore, the single-band tunable bandpass filter can be switched to a dual-band tunable filter with the same tuning elements. In the dual-band state, each band can be frequency-tuned independently. Generally, switching the operating modes, the total number of poles in the passband would be doubled if the cavities are cascaded and the number of poles in each passband should be the same. For instance, the tunable bandpass filter has 2 poles in the single-band state while has 2+2 poles in the dual-band state. Moreover, if this type of cavity is cascaded with other cavities, the number of poles in the passband can be different. In other words,

in the dual-band state, the number of poles in the lower and upper passband are different. For example, the tunable bandpass filter has 3 poles in the single-band state while has 3+2 poles in the dual-band state. Whether the lower or upper passband has a larger number of poles, it can be flexibly designed. The advantage is that one TZ can be introduced, no matter in the lower or upper passband as well as no matter in the lower or upper side of the passband, to enhance out-of-band isolation.

In Chapter 7, a volume controllable resonator for THz filter applications is presented. The resonator has a larger resonant cavity compared to that of the fundamental mode case while it maintains an unloaded quality factor similar to that of the fundamental mode. The resulting volume of the resonator is controllable at the same resonant frequency by changing the diameter of the post in the middle of the cavity. Thanks to a larger volume of the resonator, it has the potential to overcome the processing accuracy issue, to reduce the fabrication difficulty, and to enable the possibility of resonant mode. For experimental verification, a third-order THz bandpass filter has been designed, fabricated, and measured. The resonant cavity can be made almost twice the counterpart of the fundamental mode.

All the tunable and reconfigurable bandpass filters described and studied in Chapter 3 to Chapter 6 are realized by at least two operating modes. The advantage of using more than one operating mode can be deployed to reduce the number of tuning elements, to improve the physical coupling structure, to simplify the coupling topology, or to change the number of passbands. The FDC structure is a special physical structure, which can be regarded as a resonating mode to control the location of TZ. For these tunable and reconfigurable bandpass filters design, a theoretical derivation is required to verify the feasibility, and also a physical implementation is made to validate the development. In Chapter 7, the proposed volume controllable resonator presents good potential for THz filter applications thanks to its larger size cavity.

8.2 Future work

Although this Ph.D. thesis has attempted a detailed development of theoretical derivation and physical realization for tunable and reconfigurable bandpass filters, there is still a lot of future work that should be envisioned and continued for the exploitation of reconfigurable filters and devices with the following considerations:

1. In this work, the tuning screws are chosen as the tuning elements for tunable filters. However, it can be replaced by many other tuning schemes introduced in Chapter 2. It can be considered for tuning speed, insertion loss, automation (programmable control), size, or even accuracy, *etc*. For example, in the THz field, a new tuning methodology should be explored for reconfigurable THz filters.
2. In this work, higher-order modes are selected as operating modes. However, half or quarter modes can be considered to replace the higher-order modes of interest in this work to decrease the size of the cavity and the number of tuning elements. For instance, the widely frequency-tuning range tunable bandpass filter in Chapter 5 can be considered to replace the common mode to decrease the number of tuning elements.
3. In this work, the waveguide cavity structure is chosen to verify various filter performances. However, the waveguide can be replaced by other structures, such as SIW. For example, in [170], a fully reconfigurable dual-mode bandpass filter is realized by mounting varactor diodes on SIW, as shown in Fig. 7.1.

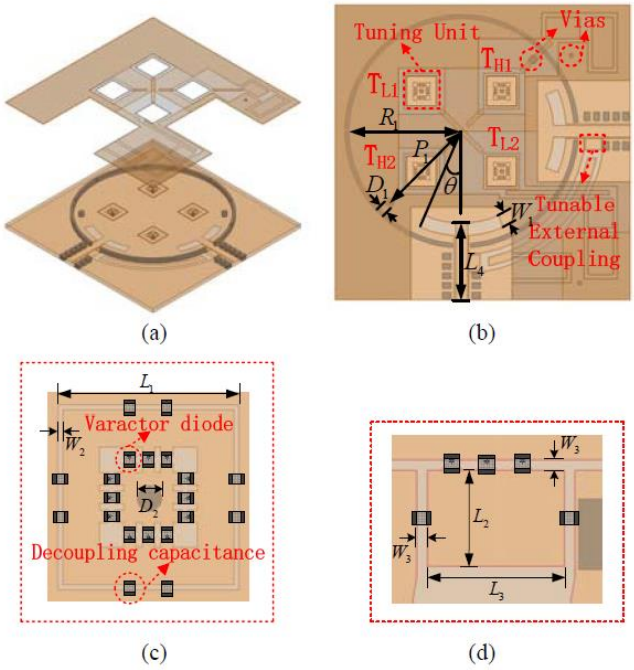

Figure 8.1 Topology of our proposed reconfigurable dual-mode bandpass filter. (a) 3D view of the proposed bandpass filter. (b) Top view of the proposed bandpass filter. (c) Top view of one of tuning unit circuits. (d) Top view of one of external coupling circuits[170]

4. In this work, only the tunable and reconfigurable bandpass filters are studied, designed and measured. In general, tunable and reconfigurable bandstop filter, diplexer, and antenna can be designed with the same theoretical principle and guidance. What's more, the reconfigurable or switchable states between bandpass and bandstop filter can be considered in the future.
5. At last but not least, the methodology for tuning and reconfiguring filters at higher-operating frequencies should be explored such as THz. It is a new era for tunable and reconfigurable devices.

REFERENCES

[1] A. E. Williams, "A four-cavity elliptic waveguide filter," *IEEE Transactions on Microwave Theory and Techniques,* vol. 18, no. 12, pp. 1109-1114, Dec. 1970.

[2] J. Tao, X. G. Huang, X. Lin, Q. Zhang, and X. Jin, "A narrow-band subwavelength plasmonic waveguide filter with asymmetrical multiple-teeth-shaped structure," *Optics Express,* vol. 17, no.16, pp. 13989-13994, Jun. 2009.

[3] A. E. Atia and A. E. Williams, "Narrow-bandpass waveguide filters," *IEEE Transactions on Microwave Theory and Techniques,* vol. 20, no. 4, pp. 258-265, Apr. 1972.

[4] C. Caloz and T. Itoh, "Application of the transmission line theory of left-handed (LH) materials to the realization of a microstrip" LH line"," in *IEEE Antennas and Propagation Society International Symposium (IEEE Cat. No. 02CH37313)*, 2002, pp. 412-415 vol.2.

[5] J.-S. Park, J.-S. Yun, and D. Ahn, "A design of the novel coupled-line bandpass filter using defected ground structure with wide stopband performance," *IEEE Transactions on Microwave Theory and Techniques,* vol. 50, no. 9, pp. 2037-2043, Sept. 2002.

[6] S. B. Cohn, "Parallel-coupled transmission-line-resonator filters," *IRE Transactions on Microwave Theory and Techniques,* vol. 6, no. 2, pp. 223-231, Apr. 1958.

[7] Z.-C. Hao, W. Hong, J.-X. Chen, X.-P. Chen, and K. Wu, "Compact super-wide bandpass substrate integrated waveguide (SIW) filters," *IEEE Transactions on Microwave Theory and Techniques,* vol. 53, no. 9, pp. 2968-2977, Sept. 2005.

[8] K. Wu, D. Deslandes, and Y. Cassivi, "The substrate integrated circuits-a new concept for high-frequency electronics and optoelectronics," in *6th International Conference on Telecommunications in Modern Satellite, Cable and Broadcasting Service, 2003. TELSIKS 2003.*, 2003, pp. P-III.

[9] X.-P. Chen and K. Wu, "Substrate integrated waveguide cross-coupled filter with negative coupling structure," *IEEE Transactions on Microwave Theory and Techniques* , vol. 56, no. 1, pp. 142-149, Jan. 2008.

[10] G. A. Campbell, "Physical theory of the electric wave-filter," *The Bell System Technical Journal,* vol. 1, no. 2, pp. 1-32, Nov. 1922.

[11] L. Weinberg, "Explicit formulas for Tschebyscheff and Butterworth ladder networks," *Journal of Applied Physics,* vol. 28, pp. 1155-1160, Mar. 1957.

[12] R. Levy, "Tables of element values for the distributed low-pass prototype filter," *IEEE Transactions on Microwave Theory and Techniques,* vol. 13, no. 5, pp. 514-536, Sept. 1965.

[13] A. Atia, A. Williams, and R. Newcomb, "Narrow-band multiple-coupled cavity synthesis," *IEEE Transactions on Circuits and Systems,* vol. 21, no. 5, pp. 649-655, Sept. 1974.

[14] R. J. Cameron, "General coupling matrix synthesis methods for Chebyshev filtering functions," *IEEE Transactions on Microwave Theory and Techniques* , vol. 47, no. 4, pp. 433-442, Apr. 1999.

[15] R. J. Cameron, "Advanced coupling matrix synthesis techniques for microwave filters," *IEEE Transactions on Microwave Theory and Techniques*, vol. 51, no. 1, pp. 1-10, Jan. 2003.

[16] N. Vahabisani, S. Khan, and M. Daneshmand, "Microfluidically reconfigurable rectangular waveguide filter using liquid metal posts," *IEEE Microwave and Wireless Components Letters*, vol. 26, no. 10, pp. 801-803, Oct. 2016.

[17] R. R. Mansour, F. Huang, S. Fouladi, W. D. Yan, and M. Nasr, "High-Q tunable filters: Challenges and potential," *IEEE Microwave Magazine*, vol. 15, no. 5, pp. 70-82, July-Aug. 2014.

[18] R. R. Mansour, "High-Q tunable dielectric resonator filters," *IEEE Microwave Magazine*, vol. 10, no. 6, pp. 84-98, Oct. 2009.

[19] K. Entesari, A. P. Saghati, V. Sekar, and M. Armendariz, "Tunable SIW structures: antennas, VCOs, and filters," *IEEE Microwave Magazine*, vol. 16, no. 5, pp. 34-54, Jun. 2015.

[20] X.-P. Chen and K. Wu, "Substrate integrated waveguide filters: Design techniques and structure innovations," *IEEE Microwave Magazine*, vol. 15, no. 6, pp. 121-133, Sept.-Oct. 2014.

[21] W. Lin, P. Zhao, T.-H. Lee, T. Liu, J.-J. Laurin, and K. Wu, "Tunable bandpass filters with reconfigurable symmetric transmission zeros on real or imaginary axis," *IEEE Journal of Microwaves*, vol. 2, no. 1, pp. 145-161, Jan. 2022.

[22] W. Lin, K. Zhou, and K. Wu, "Tunable bandpass filters with one switchable transmission zero by only tuning resonances," *IEEE Microwave and Wireless Components Letters*, vol. 31, no. 2, pp. 105-108, Feb. 2021.

[23] A. Perigaud, O. Tantot, N. Delhote, S. Verdeyme, S. Bila, D. Pacaud, *et al.*, "Continuously tuned Ku-band cavity filter based on dielectric perturbers made by ceramic additive manufacturing for space applications," *Proceedings of the IEEE*, vol. 105, no. 4, pp. 677-687, Apr. 2017.

[24] S. Nam, B. Lee, C. Kwak, and J. Lee, "A new class of K-band high-Q frequency-tunable circular cavity filter," *IEEE Transactions on Microwave Theory and Techniques*, vol. 66, no. 3, pp. 1228-1237, Mar. 2018.

[25] S. Fouladi, F. Huang, W. D. Yan, and R. R. Mansour, "High-Q narrowband tunable combline bandpass filters using MEMS capacitor banks and piezomotors," *IEEE Transactions on Microwave Theory and Techniques*, vol. 61, no. 1, pp. 393-402, Jan. 2013.

[26] R. Zhang and R. R. Mansour, "Low-cost dielectric-resonator filters with improved spurious performance," *IEEE Transactions on Microwave Theory and Techniques*, vol. 55, no. 10, pp. 2168-2175, Oct. 2007.

[27] P. Petrov, N. M. Alford, O. Buslov, V. Keis, I. Kotelnikov, P. Kulik, *et al.*, "Tuneable two-pole one-dielectric-resonator filter with elliptic characteristics," *Integrated Ferroelectrics*, vol. 66, no. 1, pp. 261-266, Jan. 2004.

[28] L. Pelliccia, F. Cacciamani, P. Farinelli, and R. Sorrentino, "High-Q tunable waveguide filters using ohmic RF MEMS switches," *IEEE Transactions on Microwave Theory and Techniques*, vol. 63, no. 10, pp. 3381-3390, Oct. 2015.

[29] M. Iskander, M. Nasresfahani, and R. Mansour, "A constant-Q tunable combline bandpass filter using angular tuning technique," in *2014 44th European Microwave Conference*, 2014, pp. 1103-1106.

[30] W. D. Yan and R. R. Mansour, "Tunable dielectric resonator bandpass filter with embedded MEMS tuning elements," *IEEE Transactions on Microwave Theory and Techniques*, vol. 55, no. 1, pp. 154-160, Jan. 2007.

[31] F. Huang, S. Fouladi, and R. R. Mansour, "High-Q tunable dielectric resonator filters using MEMS technology," *IEEE Transactions on Microwave Theory and Techniques*, vol. 59, no. 12, pp. 3401-3409, Dec. 2011.

[32] J. Krupka, A. Abramowicz, and K. Derzakowski, "Magnetically tunable filters for cellular communication terminals," *IEEE Transactions on Microwave Theory and Techniques*, vol. 54, no. 6, pp. 2329-2335, Jun. 2006.

[33] Ö. Acar, T. K. Johansen, and V. Zhurbenko, "A high-power low-loss continuously tunable bandpass filter with transversely biased ferrite-loaded coaxial resonators," *IEEE Transactions on Microwave Theory and Techniques*, vol. 63, no. 10, pp. 3425-3432, Oct. 2015.

[34] E. Polat, R. Reese, M. Jost, C. Schuster, M. Nickel, R. Jakoby, *et al.*, "Tunable liquid crystal filter in nonradiative dielectric waveguide technology at 60 GHz," *IEEE Microwave and Wireless Components Letters*, vol. 29, no. 1, pp. 44-46, Jan. 2019.

[35] J. Ossorio, J. Vague, V. E. Boria, and M. Guglielmi, "Exploring the tuning range of channel filters for satellite applications using electromagnetic-based computer aided design tools," *IEEE Transactions on Microwave Theory and Techniques*, vol. 66, no. 2, pp. 717-725, Feb. 2018.

[36] M. Armendariz, V. Sekar, and K. Entesari, "Tunable SIW bandpass filters with PIN diodes," in *the 40th European Microwave Conference*, 2010, pp. 830-833.

[37] S. Sirci, J. Martinez, M. Taroncher, and V. Boria, "Varactor-loaded continuously tunable SIW resonator for reconfigurable filter design," in *2011 41st European Microwave Conference*, 2011, pp. 436-439.

[38] S. Lee, J.-M. Kim, J.-M. Kim, Y.-K. Kim, and Y. Kwon, "Millimeter-wave MEMS tunable low pass filter with reconfigurable series inductors and capacitive shunt switches," *IEEE Microwave and Wireless Components Letters*, vol. 15, no. 10, pp. 691-693, Oct. 2005.

[39] K. Entesari and G. M. Rebeiz, "A 12-18-GHz three-pole RF MEMS tunable filter," *IEEE Transactions on Microwave Theory and Techniques*, vol. 53, no. 8, pp. 2566-2571, Aug. 2005.

[40] V. Sekar, M. Armendariz, and K. Entesari, "A 1.2–1.6-GHz substrate-integrated-waveguide RF MEMS tunable filter," *IEEE Transactions on Microwave Theory and Techniques*, vol. 59, no. 4, pp. 866-876, Apr. 2011.

[41] A. Anand, J. Small, D. Peroulis, and X. Liu, "Theory and design of octave tunable filters with lumped tuning elements," *IEEE Transactions on Microwave Theory and Techniques,* vol. 61, no. 12, pp. 4353-4364, Dec. 2013.

[42] F. Mira, J. Mateu, and C. Collado, " Mechanical tuning of substrate integrated waveguide filters," *IEEE Transactions on Microwave Theory and Techniques,* vol. 63, no. 12, pp. 3939-3946, Dec. 2015.

[43] F. Huang, J. Zhou, and W. Hong, "Ku band continuously tunable circular cavity SIW filter with one parameter," *IEEE Microwave and Wireless Components Letters,* vol. 26, no. 4, pp. 270-272, Apr. 2016.

[44] P. Adhikari, W. Yang, and D. Peroulis, "A 20–26.5-GHz PCB bandpass filter tuned with contactless tuners," *IEEE Microwave and Wireless Components Letters*, vol. 29, no. 8, pp. 513-515, Aug. 2019.

[45] M. Abdelfattah and D. Peroulis, "High-Q tunable evanescent-mode cavity SIW resonators and filters with contactless tuners," *IEEE Transactions on Microwave Theory and Techniques*, vol. 67, no. 9, pp. 3661-3672, Sept. 2019.

[46] S. Adhikari, Y.-J. Ban, and K. Wu, "Magnetically tunable ferrite loaded substrate integrated waveguide cavity resonator," *IEEE Microwave and Wireless Components Letters*, vol. 21, no. 3, pp. 139-141, Mar. 2011.

[47] S. Courrèges, Y. Li, Z. Zhao, K. Choi, A. Hunt, S. Horst, *et al.*, "A Ka-band electronically tunable ferroelectric filter," *IEEE Microwave and Wireless Components Letters*, vol. 19, no. 6, pp. 356-358, Jun. 2009.

[48] S. N. McClung, S. Saeedi, and H. H. Sigmarsson, "Band-reconfigurable filter with liquid metal actuation," *IEEE Transactions on Microwave Theory and Techniques*, vol. 66, no. 6, pp. 3073-3080, Jun. 2018.

[49] A. Ghiotto, S. Adhikari, and K. Wu, "Ferrite-loaded substrate integrated waveguide switch," *IEEE Microwave and Wireless Components Letters*, vol. 22, no. 3, pp. 120-122, Mar. 2012.

[50] S. Adhikari, A. Ghiotto, and K. Wu, "Simultaneous electric and magnetic two-dimensionally tuned parameter-agile SIW devices," *IEEE Transactions on Microwave Theory and Techniques*, vol. 61, no. 1, pp. 423-435, Jan. 2013.

[51] S. Moon, H. H. Sigmarsson, H. Joshi, and W. J. Chappell, "Substrate integrated evanescent-mode cavity filter with a 3.5 to 1 tuning ratio," *IEEE Microwave and Wireless Components Letters*, vol. 20, no. 8, pp. 450-452, Aug. 2010.

[52] E. J. Naglich, J. Lee, D. Peroulis, and W. J. Chappell, "Extended passband bandstop filter cascade with continuous 0.85–6.6-GHz coverage," *IEEE Transactions on Microwave Theory and Techniques*, vol. 60, no. 1, pp. 21-30, Jan. 2012.

[53] J. Lee, E. J. Naglich, H. H. Sigmarsson, D. Peroulis, and W. J. Chappell, "Tunable inter-resonator coupling structure with positive and negative values and its application to the field-programmable filter array (FPFA)," *IEEE Transactions on Microwave Theory and Techniques*, vol. 59, no. 12, pp. 3389-3400, Dec. 2011.

[54] T.-H. Lee, B. Lee, S. Nam, Y.-S. Kim, and J. Lee, "Frequency-tunable tri-function filter," *IEEE Transactions on Microwave Theory and Techniques,* vol. 65, no. 11, pp. 4584-4592, Nov. 2017.

[55] B. Lee, S. Nam, T.-H. Lee, and J. Lee, "Third-order frequency-agile substrate-integrated waveguide filter with a pair of transmission zeros," *IEEE Microwave and Wireless Components Letters,* vol. 27, no. 6, pp. 566-568, Jun. 2017.

[56] B. Lee, S. Nam, B. Koh, C. Kwak, and J. Lee, "K-band frequency tunable substrate-integrated-waveguide resonator filter with enhanced stopband attenuation," *IEEE Transactions on Microwave Theory and Techniques,* vol. 63, no. 11, pp. 3632-3640, Nov. 2015.

[57] K. Lee, T.-H. Lee, C.-S. Ahn, Y.-S. Kim, and J. Lee, "Reconfigurable dual-stopband filters with reduced number of couplings between a transmission line and resonators," *IEEE Microwave and Wireless Components Letters,* vol. 25, no. 2, pp. 106-108, Feb. 2015.

[58] S.-W. Jeong, G. Lee, J. Lee, and J. Lee, "Frequency-Tunable Absorptive Bandpass Filter Using Substrate-Integrated Waveguide Structure," *IEEE Transactions on Microwave Theory and Techniques,* vol. 69, no. 12, pp. 5351-5359, Dec. 2021.

[59] M. Abdelfattah, R. Zhang, and D. Peroulis, "High-selectivity tunable filters with dual-mode SIW resonators in an L-shaped coupling scheme," *IEEE Transactions on Microwave Theory and Techniques,* vol. 67, no. 12, pp. 5016-5028, Dec. 2019.

[60] X. Y. Zhang and Q. Xue, "Novel dual-mode dual-band filters using coplanar-waveguide-fed ring resonators," *IEEE Transactions on Microwave Theory and Techniques,* vol. 55, no. 10, pp. 2183-2190, Oct. 2007.

[61] E. J. Naglich, J. Lee, H. H. Sigmarsson, D. Peroulis, and W. J. Chappell, "Intersecting parallel-plate waveguide loaded cavities for dual-mode and dual-band filters," *IEEE Transactions on Microwave Theory and Techniques,* vol. 61, no. 5, pp. 1829-1838, May 2013.

[62] S. Adhikari, S. Hemour, A. Ghiotto, and K. Wu, "Magnetically tunable ferrite-loaded half-mode substrate integrated waveguide," *IEEE Microwave and Wireless Components Letters,* vol. 25, no. 3, pp. 172-174, Mar. 2015.

[63] B. You, S. Lu, L. Chen, and Q. Gu, "A half-mode substrate-integrated filter with tunable center frequency and reconfigurable bandwidth," *IEEE Microwave and Wireless Components Letters,* vol. 26, no. 3, pp. 189-191, Mar. 2016.

[64] M. F. Hagag, M. A. Khater, M. D. Sinanis, and D. Peroulis, "Ultra-compact tunable filtering rat-race coupler based on half-mode SIW evanescent-mode cavity resonators," *IEEE Transactions on Microwave Theory and Techniques,* vol. 66, no. 12, pp. 5563-5572, Dec. 2018.

[65] L.-S. Wu, X.-L. Zhou, W.-Y. Yin, C.-T. Liu, L. Zhou, J.-F. Mao, *et al.*, "A new type of periodically loaded half-mode substrate integrated waveguide and its applications," *IEEE Transactions on Microwave Theory and Techniques,* vol. 58, no. 4, pp. 882-893, Apr. 2010.

[66] C.-X. Zhou, C.-M. Zhu, and W. Wu, "Tunable dual-band filter based on stub-capacitor-loaded half-mode substrate integrated waveguide," *IEEE Transactions on Microwave Theory and Techniques,* vol. 65, no. 1, pp. 147-155, Jan. 2017.

[67] V. Sekar and K. Entesari, "A half-mode substrate-integrated-waveguide tunable filter using packaged RF MEMS switches," *IEEE Microwave and Wireless Components Letters,* vol. 22, no. 7, pp. 336-338, Jul. 2012.

[68] J. Guo, B. You, and G. Q. Luo, "A miniaturized eighth-mode substrate-integrated waveguide filter with both tunable center frequency and bandwidth," *IEEE Microwave and Wireless Components Letters,* vol. 29, no. 7, pp. 450-452, Jul. 2019.

[69] R. J. Cameron, M. Yu, and Y. Wang, "Direct-coupled microwave filters with single and dual stopbands," *IEEE Transactions on Microwave Theory and Techniques,* vol. 53, no. 11, pp. 3288-3297, Nov. 2005.

[70] M. Yu, W.-C. Tang, A. Malarky, V. Dokas, R. Cameron, and Y. Wang, "Predistortion technique for cross-coupled filters and its application to satellite communication systems," *IEEE Transactions on Microwave Theory and Techniques,* vol. 51, no. 12, pp. 2505-2515, Dec. 2003.

[71] S. Amari and U. Rosenberg, "Characteristics of cross (bypass) coupling through higher/lower order modes and their applications in elliptic filter design," *IEEE Transactions on Microwave Theory and Techniques,* vol. 53, no. 10, pp. 3135-3141, Oct. 2005.

[72] G. Macchiarella, G. G. Gentili, C. Tomassoni, S. Bastioli, and R. V. Snyder, "Design of waveguide filters with cascaded singlets through a synthesis-based approach," *IEEE Transactions on Microwave Theory and Techniques,* vol. 68, no. 6, pp. 2308-2319, Jun. 2020.

[73] B. Gowrish and R. R. Mansour, "A dual-mode frequency reconfigurable waveguide filter with a constant frequency spacing between transmission zeros," in *2020 IEEE/MTT-S International Microwave Symposium (IMS),* 2020, pp. 811-814.

[74] J. B. Thomas, "Cross-coupling in coaxial cavity filters-a tutorial overview," *IEEE Transactions on Microwave Theory and Techniques,* vol. 51, no. 4, pp. 1368-1376, Apr. 2003.

[75] H. Wang and Q.-X. Chu, "An inline coaxial quasi-elliptic filter with controllable mixed electric and magnetic coupling," *IEEE Transactions on Microwave Theory and Techniques,* vol. 57, no. 3, pp. 667-673, Mar. 2009.

[76] P. Zhao and K. Wu, "Cascading fundamental building blocks with frequency-dependent couplings in microwave filters," *IEEE Transactions on Microwave Theory and Techniques,* vol. 67, no. 4, pp. 1432-1440, Apr. 2019.

[77] X.-P. Chen and K. Wu, "Substrate integrated waveguide filters: Practical aspects and design considerations," *IEEE Microwave Magazine,* vol. 15, no. 7, pp. 75-83, Nov.-Dec. 2014.

[78] K. Zhou and K. Wu, "Multichannel substrate integrated waveguide diplexers based on orthogonal dual modes and split-type multiband responses," *IEEE Transactions on Microwave Theory and Techniques,* vol. 70, no. 1, pp. 356-366, Jan. 2022.

[79] K. Zhou and K. Wu, "Wide-stopband substrate-integrated waveguide filtering crossovers with flexibly allocated channel frequencies and bandwidths," *IEEE Transactions on Microwave Theory and Techniques,* vol. 69, no. 7, pp. 3264-3274, Jul. 2021.

[80] K. Zhou and K. Wu, "Miniaturized diplexers with large frequency ratios Based on common half-mode dual-mode SIW junction-cavities," *IEEE Transactions on Microwave Theory and Techniques,* vol. 69, no. 12, pp. 5343-5350, Dec. 2021.

[81] D. Jia, Q. Feng, Q. Xiang, and K. Wu, "Multilayer substrate integrated waveguide (SIW) filters with higher-order mode suppression," *IEEE Microwave and Wireless Components Letters,* vol. 26, no. 9, pp. 678-680, Sept. 2016.

[82] B. Koh, B. Lee, S. Nam, T.-H. Lee, and J. Lee, "Integration of interresonator coupling structures with applications to filter systems with signal route selectivity," *IEEE Transactions on Microwave Theory and Techniques,* vol. 64, no. 9, pp. 2790-2803, Sept. 2016.

[83] A. Anand and X. Liu, "Reconfigurable planar capacitive coupling in substrate-integrated coaxial-cavity filters," *IEEE Transactions on Microwave Theory and Techniques,* vol. 64, no. 8, pp. 2548-2560, Aug. 2016.

[84] H. Joshi, H. H. Sigmarsson, S. Moon, D. Peroulis, and W. J. Chappell, "High-Q fully reconfigurable tunable bandpass filters," *IEEE Transactions on Microwave Theory and Techniques,* vol. 57, pp. 3525-3533, 2009.

[85] G. Basavarajappa and R. R. Mansour, "Design methodology of a tunable waveguide filter with a constant absolute bandwidth using a single tuning element," *IEEE Transactions on Microwave Theory and Techniques,* vol. 66, no. 12, pp. 3525-3533, Dec. 2009.

[86] G. Basavarajappa and R. R. Mansour, "Design methodology of a high-Q tunable coaxial filter and diplexer," *IEEE Transactions on Microwave Theory and Techniques,* vol. 67, no. 12, pp. 5005-5015, Dec. 2019.

[87] B. Gowrish and R. R. Mansour, "A tunable quarter-wavelength coaxial filter with constant absolute bandwidth using a single tuning element," *IEEE Microwave and Wireless Components Letters,* vol. 31, no. 6, pp. 658-661, Jun. 2021.

[88] B. Gowrish and R. R. Mansour, "A novel bandwidth reconfigurable waveguide filter for aerospace applications," *IEEE Microwave and Wireless Components Letters,* vol. 30, no. 6, pp. 577-580, Jun. 2020.

[89] H. Xu, Y. Wang, F. A. Ghaffar, and L. Roy, "Reconfigurable microwave filters implemented using field programmable microwave substrate," *IEEE Transactions on Microwave Theory and Techniques,* vol. 69, no. 2, pp. 1344-1354, Feb. 2021.

[90] M. A. El-Tanani and G. M. Rebeiz, "Corrugated microstrip coupled lines for constant absolute bandwidth tunable filters," *IEEE Transactions on Microwave Theory and Techniques,* vol. 58, no. 4, pp. 956-963, Apr. 2010.

[91] R. LEVY, “Filters with single transmission zeros at real or imaginary frequencies,” *IEEE Trans. Microwave Theory and Tech.*, vol. 29, no. 4, pp. 172-181, Apr. 1976.

[92] K. T. Jokela, “Narrow-band stripline or microstrip filters with transmission zeros at real and imaginary frequencies,” *IEEE Transactions on Microwave Theory and Techniques*, vol. 28, no. 6, pp. 542-547, Jun. 1980.

[93] J. D. Rhodes and R. J. Cameron, “General extracted pole synthesis technique with applications to low-loss te/sub011/mode filters,” *IEEE Transactions on Microwave Theory and Techniques*, vol. 28, no. 9, pp. 1018-1028, Sep. 1980.

[94] M. Yu and Y. Yang, “Unified extracted pole filter synthesis: Bridging the gap between EM and circuit simulations,” *IEEE Microwave Magazine*, vol. 21, no. 3, pp. 84-95, Mar. 2020.

[95] L. Szydlowski, A. Lamecki, and M. Mrozowski, “Coupled-resonator waveguide filter in quadruplet topology with frequency-dependent coupling–a design based on coupling matrix,” *IEEE Microwave and Wireless Components Letters*, vol. 22, no. 11, pp. 553-555, Nov. 2012.

[96] Y. He, G. Macchiarella, G. Wang, W. Wu, L. Sun, L. Wang, *et al.*, “A direct matrix synthesis for in-line filters with transmission zeros generated by frequency-variant couplings,” *IEEE Transactions on Microwave Theory and Techniques*, vol. 66, no. 4, pp. 1780-1789, Apr. 2018.

[97] R. J. Cameron and J. Rhodes, “Asymmetric realizations for dual-mode bandpass filters,” *IEEE Transactions on Microwave Theory and Techniques*, vol. 29, no. 1, pp. 51-58, Jan. 1981.

[98] S. Tamiazzo and G. Macchiarella, “An analytical technique for the synthesis of cascaded N-tuplets cross-coupled resonators microwave filters using matrix rotations,” *IEEE Transactions on Microwave Theory and Techniques*, vol. 53, no. 5, pp. 1693-1698, May 2005.

[99] G. Macchiarella and S. Tamiazzo, “Synthesis without optimization of cascaded inline prototype filters with arbitrary transmission zeros,” in *2005 European Microwave Conference*, 2005, p. 4 pp.

[100] R. Levy, “Direct synthesis of cascaded quadruplet (CQ) filters,” *IEEE Transactions on Microwave Theory and Techniques*, vol. 43, no. 12, pp. 2940-2945, Dec. 1995.

[101] X. Chen, W. Hong, T. Cui, J. Chen, and K. Wu, “Substrate integrated waveguide (SIW) linear phase filter,” *IEEE Microwave and Wireless Components Letters*, vol. 15, no. 11, pp. 787-789, Nov. 2005.

[102] J. D. Rhodes, “The generalized direct-coupled cavity linear phase filter,” *IEEE Transactions on Microwave Theory and Techniques*, vol. 18, no. 6, pp. 308-313, Jun. 1970.

[103] T. Martin, A. Ghiotto, T.-P. Vuong, K. Wu, and F. Lotz, “Compact quasi-elliptic and highly selective AFSIW filter with multilayer cross-coupling,” in *2019 IEEE MTT-S International Microwave Symposium (IMS)*, 2019, pp. 718-721.

[104] K. Ahn and I. Yom, "A Ka-band multilayer LTCC 4-pole bandpass filter using dual-mode cavity resonators," in *2008 IEEE MTT-S International Microwave Symposium Digest*, 2008, pp. 1235-1238.

[105] W. Shen, X.-W. Sun, W.-Y. Yin, J.-F. Mao, and Q.-F. Wei, "A novel single-cavity dual mode substrate integrated waveguide filter with non-resonating node," *IEEE Microwave and Wireless Components Letters,* vol. 19, no. 6, pp. 368-370, Jun. 2009.

[106] K. Zhou, C.-X. Zhou, and W. Wu, "Substrate-integrated waveguide dual-mode dual-band bandpass filters with widely controllable bandwidth ratios," *IEEE Transactions on Microwave Theory and Techniques,* vol. 65, no. 10, pp. 3801-3812, Oct. 2017.

[107] A. K. Gorur, C. Karpuz, and A. Gorur, "Design of dual-mode dual-band bandpass filter with independently tunable bandwidths and reconfigurable filtering characteristics," in *2017 IEEE MTT-S International Microwave Symposium (IMS)*, 2017, pp. 922-925.

[108] R. J. Cameron, C. M. Kudsia, and R. R. Mansour, *Microwave filters for communication systems: fundamentals, design, and applications*: John Wiley & Sons, 2018.

[109] A. Gorur, "Description of coupling between degenerate modes of a dual-mode microstrip loop resonator using a novel perturbation arrangement and its dual-mode bandpass filter applications," *IEEE Transactions on Microwave Theory and Techniques,* vol. 52, no. 2, pp. 671-677, Feb. 2004.

[110] S. Bastioli, C. Tomassoni, and R. Sorrentino, "A new class of waveguide dual-mode filters using TM and nonresonating modes," *IEEE Transactions on Microwave Theory and Techniques,* vol. 58, no. 12, pp. 3909-3917, Dec. 2010.

[111] B. Gustavsen and A. Semlyen, "Simulation of transmission line transients using vector fitting and modal decomposition," *IEEE Transactions on Power Delivery*, vol. 13, no. 2, pp. 605-614, April 1998.

[112] P. Zhao, "Phase de-embedding of narrowband coupled-resonator networks by vector fitting," *IEEE Transactions on Microwave Theory and Techniques,* 2018.

[113] P. Zhao and K.-L. Wu, "Model-based vector-fitting method for circuit model extraction of coupled-resonator diplexers," *IEEE Transactions on Microwave Theory and Techniques,* vol. 64, no. 6, pp. 1787-1797, Jun. 2016.

[114] X. Y. Zhang and Q. Xue, "High-selectivity tunable bandpass filters with harmonic suppression," *IEEE Transactions on Microwave Theory and Techniques,* vol. 58, no. 4, pp. 964-969, Apr. 2010.

[115] D. Tian, Q. Feng, and Q. Xiang, "Synthesis applied 4th-order constant absolute bandwidth frequency-agile bandpass filter with cross-coupling," *IEEE Access,* vol. 6, pp. 72287-72294, 2018.

[116] S. Amari, U. Rosenberg, and J. Bornemann, "Singlets, cascaded singlets, and the nonresonating node model for advanced modular design of elliptic filters," *IEEE Microwave and Wireless Components Letters,* vol. 14, no. 5, pp. 237-239, May 2004.

[117] L. Szydlowski, A. Lamecki, and M. Mrozowski, "Coupled-resonator filters with frequency-dependent couplings: Coupling matrix synthesis," *IEEE Microwave and Wireless Components Letters,* vol. 22, no. 6, pp. 312-314, June 2012.

[118] S. Amari and J. Bornemann, "Using frequency-dependent coupling to generate finite attenuation poles in direct-coupled resonator bandpass filters," *IEEE Microwave and Guided Wave Letters,* vol. 9, no. 10, pp. 404-406, Oct. 1999.

[119] G. Macchiarella and S. Tamiazzo, "Cooking microwave filters: Is synthesis still helpful in microwave filter design?," *IEEE Microwave Magazine,* vol. 21, no. 3, pp. 20-33, March 2020.

[120] S. Amari and G. Macchiarella, "Synthesis of inline filters with arbitrarily placed attenuation poles by using nonresonating nodes," *IEEE Transactions on Microwave Theory and Techniques,* vol. 53, no. 10, pp. 3075-3081, Oct. 2005.

[121] R. Levy, "Filters with single transmission zeros at real or imaginary frequencies," *IEEE Transactions on Microwave Theory and Techniques,* vol. 24, no. 4, pp. 172-181, Apr. 1976.

[122] G. Matthaei, "Microwave filters, impedance-matching networks and coupling structures," *Artech House Book,* pp. 775-809, 1980.

[123] R. J. Cameron, A. Harish, and C. J. Radcliffe, "Synthesis of advanced microwave filters without diagonal cross-couplings," *IEEE Transactions on Microwave Theory and Techniques,* vol. 50, no. 12, pp. 2862-2872, Dec. 2002.

[124] G. Macchiarella, G. Gentili, N. Delmonte, L. Silvestri, C. Tomassoni, L. Perregrini, *et al.*, "Accurate modeling of stubs used as resonant coupling elements in SIW filters," *IEEE Microwave and Wireless Components Letters,* vol. 30, no. 12, pp. 1125-1128, Dec. 2020.

[125] A. Zakharov, "Transmission zeros of trisection and quadruplet bandpass filters with mixed cross coupling," *IEEE Transactions on Microwave Theory and Techniques,* vol. 69, no. 1, pp. 89-100, Jan. 2021.

[126] L. Szydlowski, N. Leszczynska, and M. Mrozowski, "Dimensional synthesis of coupled-resonator pseudoelliptic microwave bandpass filters with constant and dispersive couplings," *IEEE Transactions on Microwave Theory and Techniques,* vol. 62, no. 8, pp. 1634-1646, Aug. 2014.

[127] J.-K. Xiao, M. Zhu, Y. Li, L. Tian, and J.-G. Ma, "High selective microstrip bandpass filter and diplexer with mixed electromagnetic coupling," *IEEE Microwave and Wireless Components Letters,* vol. 25, no. 12, pp. 781-783, Dec. 2015.

[128] P. Zhao and K. Wu, "Waveguide filters with central-post resonators," *IEEE Microwave and Wireless Components Letters,* vol. 30, no. 7, pp. 657-660, Jul. 2020.

[129] S. Tamiazzo and G. Macchiarella, "Synthesis of cross-coupled filters with frequency-dependent couplings," *IEEE Transactions on Microwave Theory and Techniques,* vol. 65, no. 3, pp. 775-782, Mar. 2017.

[130] D. Psychogiou and K. Sadasivan, "Tunable coaxial cavity resonator-based filters using actuated liquid metal posts," *IEEE Microwave and Wireless Components Letters,* vol. 29, no. 12, pp. 763-766, Dec. 2019.

[131] D. Lu, N. S. Barker, and X. Tang, "A simple frequency-agile bandpass filter with predefined bandwidth and stopband using synchronously tuned dual-mode resonator," *IEEE Microwave and Wireless Components Letters,* vol. 27, no. 11, pp. 983-985, Nov. 2017.

[132] D. Packiaraj, M. Ramesh, and A. Kalghatgi, "Design of a tri-section folded SIR filter," *IEEE Microwave and Wireless Components Letters,* vol. 16, no. 5, pp. 317-319, May 2006.

[133] S. Amari, G. Tadeson, J. Cihlar, R. Wu, and U. Rosenberg, "Pseudo-elliptic microstrip line filters with zero-shifting properties," *IEEE Microwave and Wireless Components Letters,* vol. 14, no. 7, pp. 346-348, Jul. 2004.

[134] M. M. Mendoza, D. Martinez, D. C. Rebenaque, and A. Alvarez-Melcon, "Enhanced topologies for the design of dual-mode filters using inductive waveguide structures," *Radio Science,* vol. 50, no. 1, pp. 66-77, Jan. 2015.

[135] S. Amari and M. Bekheit, "New dual-mode dielectric resonator filters," *IEEE Microwave and Wireless Components Letters,* vol. 15, no. 3, pp. 162-164, Mar. 2005.

[136] Y.-H. Chun and J.-S. Hong, "Electronically reconfigurable dual-modemicrostrip open-loop resonator filter," *IEEE Microwave and Wireless Components Letters*, vol. 18, no. 7, pp. 449-451, Jul. 2008.

[137] H.-J. Tsai, B.-C. Huang, N.-W. Chen, and S.-K. Jeng, "A reconfigurable bandpass filter based on a varactor-perturbed, T-shaped dual-mode resonator," *IEEE Microwave and Wireless Components Letters,* vol. 24, no. 5, pp. 297-299, May 2014.

[138] M. Á. Sánchez-Soriano, S. Sirci, J. D. Martínez, and V. E. Boria, "Compact dual-mode substrate integrated waveguide coaxial cavity for bandpass filter design," *IEEE Microwave and Wireless Components Letters,* vol. 26, no. 6, pp. 386-388, Jun. 2016.

[139] Q. Liu, D. Zhou, Y. Zhang, D. Zhang, and D. Lv, "Substrate integrated waveguide bandpass filters in box-like topology with bypass and direct couplings in diagonal cross-coupling path," *IEEE Transactions on Microwave Theory and Techniques*, vol. 67, no. 3, pp. 1014-1022, Mar. 2019.

[140] M. Guglielmi, F. Montauti, L. Pellegrini, and P. Arcioni, "Implementing transmission zeros in inductive-window bandpass filters," *IEEE Transactions on Microwave Theory and Techniques,* vol. 43, no. 8, pp. 1911-1915, Aug. 1995.

[141] F. Lin and M. Rais-Zadeh, "Continuously tunable 0.55–1.9-GHz bandpass filter with a constant bandwidth using switchable varactor-tuned resonators," *IEEE Transactions on Microwave Theory and Techniques,* vol. 65, no. 3, pp. 792-803, Mar. 2017.

[142] J. Xu and Y. Zhu, "Tunable bandpass filter using a switched tunable diplexer technique," *IEEE Transactions on Industrial Electronics,* vol. 64, no. 4, pp. 3118-3126, Apr. 2017.

[143] D. Lu, M. Yu, N. S. Barker, Z. Li, W. Li, and X. Tang, "Advanced synthesis of wide-tuning-range frequency-adaptive bandpass filter with constant absolute bandwidth," *IEEE Transactions on Microwave Theory and Techniques,* vol. 67, no. 11, pp. 4362-4375, Nov. 2019.

[144] Z. Zhao, J. Chen, L. Yang, and K. Chen, "Three-pole tunable filters with constant bandwidth using mixed combline and split-ring resonators," *IEEE Microwave and Wireless Components Letters,* vol. 24, no. 10, pp. 671-673, Oct. 2014.

[145] Z. Li, X. Tang, D. Lu, and M. Yu, "Tunable diplexer with identical passband and constant absolute bandwidth," *IEEE Transactions on Microwave Theory and Techniques,* vol. 68, no. 2, pp. 721-731, Feb. 2020.

[146] U. Rosenberg and M. Knipp, "Novel tunable high Q filter design for branching networks with extreme narrowband channels at mm-wave frequencies," in *2005 European Microwave Conference*, 2005, pp. 4 pp.-824.

[147] S. Nam, B. Lee, C. Kwak, and J. Lee, "Contactless tuning plunger and its application to K-band frequency-tunable cavity filter," *IEEE Transactions on Microwave Theory and Techniques,* vol. 67, no. 7, pp. 2713-2719, Jul. 2019.

[148] P. Aurélien, V. Serge, D. Nicolas, B. Stéphane, T. Olivier, and L. Carpentier, "Continuously tunable X-band filter using a 3D spiral ribbon," in *2018 IEEE MTT-S International Conference on Numerical Electromagnetic and Multiphysics Modeling and Optimization (NEMO),* 2018, pp. 1-4.

[149] J.-X. Xu, L. Yang, Y. Yang, and X. Y. Zhang, "High-Q factor tunable bandpass filter with constant absolute bandwidth and wide tuning range based on coaxial resonators," *IEEE Transactions on Microwave Theory and Techniques,* vol. 67, no. 10, pp. 4186-4195, Oct. 2019.

[150] J.-S. G. Hong and M. J. Lancaster, *Microstrip filters for RF/microwave applications*: John Wiley & Sons, 2004.

[151] D. M. Pozar, *Microwave engineering*: John wiley & sons, 2011.

[152] Y. Yang, M. Yu, and Q. Wu, "Advanced synthesis technique for unified extracted pole filters," *IEEE Transactions on Microwave Theory and Techniques,* vol. 64, no. 12, pp. 4463-4472, Dec. 2016.

[153] E. Guerrero, J. Verdú, and P. de Paco, "Synthesis of extracted pole filters with transmission zeros in both stopbands and nonresonant nodes of the same nature," *IEEE Microwave and Wireless Components Letters,* vol. 31, no. 1, pp. 17-20, Jan. 2021.

[154] C.-F. Chen, "Design of a microstrip three-state switchable and fully tunable bandpass filter with an extra-wide frequency tuning range," *IEEE Access,* vol. 8, pp. 66438-66447, 2020.

[155] Y.-H. Cho and G. M. Rebeiz, "Tunable 4-pole noncontiguous 0.7–2.1-GHz bandpass filters based on dual zero-value couplings," *IEEE Transactions on Microwave Theory and Techniques,* vol. 63, no. 5, pp. 1579-1586, May 2015.

[156] C.-F. Chen, "A compact reconfigurable microstrip dual-band filter using varactor-tuned stub-loaded stepped-impedance resonators," *IEEE Microwave and Wireless Components Letters,* vol. 23, no. 1, pp. 16-18, Jan. 2013.

[157] X. Fang, Y. C. Li, L. W. Li, W. Che, and Q. Xue, "A dual-band tunable balanced filter with independently tuning bands," *IEEE Transactions on Circuits and Systems II: Express Briefs,* vol. 69, no. 4, pp. 2076-2080, Apr. 2022.

[158] J. R. Chen, M. D. Benge, A. Anand, H. H. Sigmarsson, and X. Liu, “An evanescent-mode tunable dual-band filter with independently-controlled center frequencies,” in *2016 IEEE MTT-S International Microwave Symposium (IMS)*, 2016, pp. 1-4.

[159] Z.-H. Chen and Q.-X. Chu, “Dual-band reconfigurable bandpass filter with independently controlled passbands and constant absolute bandwidths,” *IEEE Microwave and Wireless Components Letters*, vol. 26, no. 2, pp. 92-94, Feb. 2016.

[160] J. Xu, W. Wu, and G. Wei, “Novel dual-band bandpass filter and reconfigurable filters using lumped-element dual-resonance resonators,” *IEEE Transactions on Microwave Theory and Techniques*, vol. 64, no. 5, pp. 1496-1507, May 2016.

[161] D. J. Simpson, R. Gómez-García, and D. Psychogiou, “Single-/multi-band bandpass filters and duplexers with fully reconfigurable transfer-function characteristics,” *IEEE Transactions on Microwave Theory and Techniques*, vol. 67, no. 5, pp. 1854-1869, May 2019.

[162] Y.-H. Cho, C. Park, and S.-W. Yun, “0.7-1.0-GHz switchable dual-/single-band tunable bandpass filter using a switchable J-inverter,” *IEEE Access*, vol. 9, pp. 16967-16974, 2021.

[163] B. Lee, B. Koh, S. Nam, T.-H. Lee, and J. Lee, “Band-switchable substrate-integrated waveguide resonator and filter," *IEEE Transactions on Microwave Theory and Techniques*, vol. 66, no. 1, pp. 147-156, Jan. 2018.

[164] P.-H. Deng and J.-H. Jheng, “A switched reconfigurable high-isolation dual-band bandpass filter,” *IEEE Microwave and Wireless Components Letters*, vol. 21, no. 2, pp. 71-73, Feb. 2011.

[165] R. Zhang, R. Gómez-García, and D. Peroulis, “Multifunctional bandpass filters with reconfigurable and switchable band control,” *IEEE Transactions on Microwave Theory and Techniques*, vol. 67, no. 6, pp. 2355-2369, Jun. 2019.

[166] M.-L. Chuang and M.-T. Wu, “Switchable dual-band filter with common quarter-wavelength resonators,” *IEEE Transactions on Circuits and Systems II: Express Briefs*, vol. 62, no. 4, pp. 347-351, Apr. 2015.

[167] K. Zhao and D. Psychogiou, “Spurious suppression techniques for 3-D printed coaxial resonator bandpass filters,” *IEEE Microwave and Wireless Components Letters*, vol. 32, no. 1, pp. 33-36, Jan. 2022.

[168] J.-X. Chen, Y. Zhan, W. Qin, Z.-H. Bao, and Q. Xue, “Analysis and design of balanced dielectric resonator bandpass filters,” *IEEE Transactions on Microwave Theory and Techniques*, vol. 64, no. 5, pp. 1476-1483, May 2016.

[169] N.-H. Nguyen, A. Ghiotto, T.-P. Vuong, A. Vilcot, T. Martin, and K. Wu, “Dielectric slab air-filled substrate integrated waveguide (safsiw) bandpass filters,” *IEEE Microwave and Wireless Components Letters*, vol. 30, no. 4, pp. 363-366, Apr. 2020.

[170] W. Lin, T.-H. Lee, and K. Wu, “Fully reconfigurable dual-mode bandpass Filter,” in *2018 IEEE/MTT-S International Microwave Symposium-IMS*, 2018, pp. 397-400.

APPENDIX A LIST OF PUBLICATIONS

1. Journal papers:

[1] **W. Lin**, P. Zhao, T. -H. Lee, T. Liu, J. -J. Laurin, and K. Wu, "Tunable bandpass filters with reconfigurable symmetric transmission zeros on real or imaginary axis," in *IEEE Journal of Microwaves*, vol. 2, no. 1, pp. 145-161, Jan. 2022.

[2] **W. Lin**, K. Zhou, and K. Wu, "Band-reconfigurable tunable bandpass filters based on mode-switching concept," in *IEEE Transactions on Microwave Theory and Techniques*, Nov. 2022.

[3] **W. Lin**, P. Zhao, K. Zhou, and K. Wu, "Tunable waveguide bandpass filter with wide frequency-tuning range and constant bandwidth using mode-switching concept," submitted to *IEEE Transactions on Microwave Theory and Techniques*, Nov. 2021.

[4] **W. Lin**, K. Zhou, and K. Wu, "Tunable bandpass filters with one switchable transmission zero by only tuning resonances," in *IEEE Microwave and Wireless Components Letters*, vol. 31, no. 2, pp. 105-108, Feb. 2021.

[5] **W. Lin**, P. Zhao, and K. Wu, "Inline tunable bandpass filter with switchable asymmetric transmission zeros realized by frequency-dependent coupling," submitted to *IEEE Microwave and Wireless Components Letters*, Feb. 2022.

[6] C. Roy, **W. Lin,** and K. Wu, "Swarm intelligence homotopy hybrid optimization optimization-based ANN model for tunable bandpass filter," submitted to *IEEE Transactions on Microwave Theory and Techniques*, Nov. 2022.

[7] X. Gu, **W. Lin**, S. Hemour, and K. Wu, "Readout distance enhancement of battery-free harmonic transponder," in *IEEE Transactions on Microwave Theory and Techniques*, vol. 69, no. 7, pp. 3413-3424, Jul. 2021.

2. Conference papers:

[1] **W. Lin**, T. -H. Lee, and K. Wu, "Mixed-mode substrate integrated waveguide bandpass filter with controllable transmission zeros," *2019 IEEE MTT-S International Microwave Symposium (IMS)*, Boston, MA, USA, 2019, pp. 722-725.

[2] **W. Lin**, T. -H. Lee, and K. Wu, "Dual-band bandpass SIW resonator filter with flexible frequency ratio," *2019 49th European Microwave Conference (EuMC)*, Paris, France, 2019, pp. 364-367.

[3] **W. Lin**, T. -H. Lee, and K. Wu, "Fully reconfigurable dual-mode bandpass filter," *2018 IEEE/MTT-S International Microwave Symposium - IMS*, Philadelphia, PA, USA, 2018, pp. 397-400.

[4] T. -H. Lee, **W. Lin,** and K. Wu, "Multilayer SIW dual-mode bandpass filter with higher-order mode attenuation," *2018 IEEE MTT-S International Wireless Symposium (IWS)*, Chengdu, China, 2018, pp. 1-3.